A Sub-Kiloparsec Scale View of Star Formation in M31

Alexia R. Lewis

A dissertation
submitted in partial fulfillment of the
requirements for the degree of

Doctor of Philosophy

University of Washington

2016

Reading Committee:

Julianne J. Dalcanton, Chair

Thomas R. Quinn

Adam K. Leroy

Program Authorized to Offer Degree:
Astronomy

University of Washington

Abstract

A Sub-Kiloparsec Scale View of Star Formation in M31

Alexia R. Lewis

Chair of the Supervisory Committee:
Professor Julianne J. Dalcanton
Astronomy

This dissertation examines the properties of star formation in the nearest large Milky Way-like galaxy, the Andromeda Galaxy (M31). Using resolved star data from the Hubble Space Telescope obtained as part of the Panchromatic Hubble Andromeda Treasury (PHAT), I model the optical color-magnitude diagrams (CMDs) of > 9000 regions that are 100pc$\times$100pc (projected) in size to derive the most finely spatially-resolved star formation history (SFH) of M31 to date. I find that M31's 10 kpc star-forming ring is a long-lived feature, continually forming stars over at least the past 500 Myr. Additionally, I find that the star formation rate in M31 has decreased by a factor of $3 - 4$ over the same period of time. This is strong evidence that M31 is turning off its star formation.

I use these SFHs to predict the ultraviolet flux in each region. To do this, I create modeled spectral energy distributions by summing up simple stellar populations with ages and SFRs set by the SFH and convolving with the pare them with the observed FUV and NUV maps obtained by the *Galaxy Evolution Explorer* (*GALEX*) response curves to generate flux. I then create maps of this predicted flux in the far- and near-ultraviolet (FUV and NUV) and compare them with the observed FUV and NUV maps obtained by *GALEX*. The time resolution provided by the spatially-resolved SFHs enables very accurate modeling of the UV flux. The predicted and observed fluxes agree to within 5% in each band. I also generate maps of the intrinsic, dust-free flux and compare those to maps of *GALEX* FUV + *Spitzer*

24 μm data and I find that the synthetic maps require much more flux. This suggests a discrepancy with the 24 μm correction. This also results in an under-estimate of the FUV + 24 μm derived SFR compared to that determined from the spatially-resolved SFHs.

I also explore variation of the dust attenuation curve across the disk of M31. Using *GALEX* observations and the predicted, dust-free UV flux, I constrain the total-to-selective attenuation, R_V, and the strength of the 2175Å bump relative to the Milky Way, $f_{\rm bump}$, in each of the 100 pc size regions. I model the ensemble distribution and find a mean R_V of $\mu_{R_V} = 2.94 \pm 0.01$ with a width of $\sigma_{R_V} = 0.71 \pm 0.01$. This is steeper than the Milky Way value and implies smaller dust grains are acting as absorbers. I find considerable variation in R_V across the disk including a systematic decrease in R_V toward the center of the galaxy. Previous measurements of R_V in M31 have been limited to only a small number of sightlines. The results presented here are the largest ensemble study of R_V within the Andromeda Galaxy.

TABLE OF CONTENTS

LIST OF FIGURES

LIST OF TABLES

ACKNOWLEDGMENTS

I am extremely grateful for the support and encouragement of many individuals. I first want to acknowledge my science advisors and mentors. To my advisor, Julianne Dalcanton, for her expertise, inspiration, and support over the past six years. I have learned a great deal simply from my conversations with her where I've watched her mind work. To my committee member and former advisor, Tom Quinn, for helping me jump into the world of academic research and hit the ground running. To my committee member, Adam Leroy, for his thoughtful suggestions and ideas. I look forward to working more closely with him.

I also want to thank the graduate students in the astronomy department at the University of Washington, especially my officemate for 5 years, Lori Beerman, as well as Cliff Johnson and Jim Davenport for many conversations over the years, scientific or otherwise.

Finally, I want to acknowledge my family. To my brother and sister-in-law, Kris and Michelle, for the home-cooked meals, conversation, and laughs we've enjoyed. To my sister, Becca, for phone conversations weighty or light. To my husband, Dan, for his companionship. To my mom, who has encouraged me every step of the way and showed interest and enthusiasm in all of my research. I would not be where I am today without you. Thank you, mom. I love you.

DEDICATION

To my husband and best friend, Dan, for his constant support and love.

Our adventure continues.

Chapter 1
INTRODUCTION

The process of star formation is central to many areas of astrophysics. At the smallest scales, it informs our knowledge of the evolution of a single star and how that star affects its surrounding environment, impacting the interstellar medium (ISM) as well as affecting the habitability of its planetary systems. At larger scales, it tells us about the formation and evolution of galaxies and drives our knowledge of the evolution of the universe.

This dissertation explores the properties of star formation in the large, Milky Way (MW)-like galaxy, Andromeda (M31). M31 is an ideal target for a detailed study of star formation. It is similar to the MW in mass, size, and morphology making it a good point of comparison for the MW. It is close enough that we can use the *Hubble Space Telescope* (HST) to resolve individual stars, and it is far enough away that we can see the entire galaxy. M31's distance and size places it at a point in parameter space that opens up the intersection of small scale star formation (of order a few parsecs or less) and large scale star formation of galaxies (1 kpc or more). Study of M31with HST can provide us with a view into the details of star formation on scales of ∼100 pc, a scale that is not easily accessible in most galaxies but that can drive much of the structure observed within a galaxy.

1.1 Star Formation

The star formation rate is a simple concept — what is the mass of stars born over a given time? However, measuring a star formation rate is difficult. The necessary quantities are the ages and masses of each star, values that are not always easily obtained and that are impossible to measure beyond the closest galaxies when stars are no longer individually

resolved. Therefore, while we can use individual stars in the nearby universe, we must use other tracers of star formation at larger distances. Here, I describe a few of the most common methods for measuring SFRs as well as typical problems encountered in SFR measurements.

1.1.1 Methods for Measuring Star Formation Rates

The most straightforward way to measure a SFR is to count the number of stars of a given age. This is usually done within a young star cluster or star-forming region. The necessary assumptions are that the stars in a given cluster are of the same age and that their masses uniformly sample an initial mass function (IMF). The age of the cluster is determined by fitting an isochrone to the color-magnitude diagram (CMD) of the cluster. This is most commonly done for young stellar objects (YSOs) within molecular clouds in the MW and the Magellanic Clouds (e.g., Robitaille & Whitney 2010; Chen et al. 2010). For older and more mixed populations as well as for those that are farther away where it is not possible to count YSOs, different methods must be used.

In a small part of parameter space, outside the MW but within a few Mpc, where stars can be individually resolved, we can measure SFRs by modeling the CMDs of a region. The stars do not need to be of the same age. This process can be used to measure the SFR and the star formation history (the SFR as a function of time) for entire galaxies (e.g., Weisz et al. 2011, 2014) or for individual regions within a single galaxy (e.g., Harris & Zaritsky 2009; Lewis et al. 2015). With this method, one creates a large sample of synthetic CMDs by combing stellar populations of different ages and metallicities, and then compares each synthetic CMD to the observed CMD to find the best fit. With this method, the SFH that creates each synthetic CMD is known, so the SFH of the synthetic CMD that best fits the observed CMD is taken to be the SFH of the observed population. This is a very powerful method of determining the SFR as a function of time, sometimes up to a Hubble time, for stars that can be individually resolved in nearby galaxies. I will provide greater detail on the use of CMDs to model SFHs in Chapter 2.

For more distant populations where stars cannot be individually resolved, SFRs are typ-

ically measured with broadband tracers (e.g., Kennicutt & Evans 2012). The far-ultraviolet (FUV) is the most commonly used because it traces the photospheric emission of young stars and is therefore a fairly direct tracer of star formation. The Hα emission line is sometimes substituted for the FUV as it is less affected by dust (e.g., Calzetti et al. 2007; Kennicutt et al. 2007). Longer wavelength tracers have also been used to measure the flux emitted by young stars that is absorbed by dust and re-emitted in the infrared. In some regions, this dust-reprocessed flux can amount to a very large percentage of the flux emitted by young stars. When the data is available, a composite tracer that uses both short wavelength and long wavelength emission is most accurate. The combination of *GALEX* FUV + *Spitzer* 24 μm flux is commonly used. I will discuss the use of flux-based SFRs in comparison with CMD-based SFRs in Chapter 3.

1.1.2 Common Problems

None of the methods described above are perfect. There are complications in each that must be properly accounted for when measuring SFRs.

The most common problem that affects SFR indicators is dust. Stars form out of dense clouds of gas and dust. As they grow, they eventually blow away their natal clouds, but until they get to that point, they are surrounded by obscuring dust. This dust can prevent you from seeing all of the stars in a region (which affects star counting methods), it can make stars appear redder and older than they actually are (which affects CMD modeling) and it can absorb the light emitted by young stars and re-radiate it at different wavelengths (which affects flux-based SFRs). As such, it is essential to account for the effects of dust when measuring SFRs with any method. The effects of dust stellar emission have been widely studied and there are ways to model these effects in all SFR measurement methods.

Another uncertainty comes from the calibration of multi-wavelength SFR indicators, such as ultraviolet + infrared (UV + IR) tracers, usually parameterized as $L(\mathrm{UV}) + w \times L(\mathrm{IR})$. These indicators must be calibrated such that they are compared with a "true" measure of SFR. The Paschen-α line is commonly used because it traces the nebular emission from

young, massive stars and is largely unaffected by dust. The UV + IR combination is then compared with the Paschen-α emission to determine what the value of w should be to bring the two SFRs into agreement. This has been done for samples of nearby galaxies (e.g., Calzetti et al. 2007; Leroy et al. 2008; Hao et al. 2011). The uncertainties on these calibrations can be substantial, and recent studies suggest that w can vary by factors of a few to ten or more between galaxies and even within a single galaxy (Boquien et al. 2016). This uncertainty in the calibrations of composite SFR tracers has not been widely studied. Blind use of single coefficients can lead to SFR uncertainties of a factor of 2 – 10 or more.

In this dissertation, I use CMD modeling of resolved stars to measure the recent SFH of M31. This method is ideal because it enables the detailed study of the SFR as a function of time over 500 Myr timescales and it includes the effects of dust on the measured SFRs. CMD modeling has its own set of uncertainties; however, they can be modeled and properly accounted for in the error bars. These uncertainties will be discussed in greater detail in Chapter 2. I will also show in Chapter 4 how CMD analysis enables further analysis of the properties of the dust attenuation curve. CMD modeling therefore opens up many avenues for study.

1.2 Spatial Resolution

The most distant galaxies are unresolved blobs of light. These galaxies may have a handful of spectra or measurements of integrated light across the galaxy. More often, there is only a single measurement of the flux in a given band or perhaps a single color.

In nearby galaxies, we can tile images or place integral field units (IFUs) across the face of the galaxy to gather flux or take spectra at multiple locations (e.g., Walter et al. 2008; Dalcanton et al. 2012; Bundy et al. 2015). The resulting spatial resolution permits study of age gradients within a galaxy, where its star formation occurs, how it rotates, etc. When we can resolve individual stars, we can use the abundant age information on a CMD to uncover the detailed SFHs of subregions of a galaxy (e.g., Dohm-Palmer et al. 2002). This

spatially-resolved study of nearby galaxies is crucial to understanding the physics that drive galaxy evolution and that indirectly manifests itself in the single color or flux measurement for high redshift galaxies.

Most of what we know about star formation in galaxies comes either at the scale of individual stars (e.g., Bate 2009) or at scales of 1 kpc or more where we have developed large-scale relations, between, for example, gas and SFR surface densities (e.g., Bigiel et al. 2008) that have given us unprecedented insight into the efficiency of star formation on these scales. Extending these kinds of relations to higher resolution (smaller physical areas) will provide us with further insight into the process of star formation and galaxy evolution.

Improving the spatial resolution of observations and the details of galaxy evolution on small scales is especially important for galaxy simulations. Observations are crucial for verification of simulation outputs. For example, comparison of simulations with observations showed that early simulations produced galaxies with too many baryons. Implementation of stellar feedback in simulations brought the results into better agreement with observations (e.g., Governato et al. 2012; Scannapieco et al. 2012; Hopkins et al. 2014; Agertz & Kravtsov 2015a,b).

Observations on smaller scales permit a more detailed view of the physics of star formation, feedback, and kinematics on these intermediate scales. As the resolution of simulations improves, such observational constraints are essential for improving the input physics. This is especially important because large-scale relations are no longer completely applicable on small scales where differences in galactic structure and content are indicative of different physics.

This dissertation presents the most finely resolved SFH of a MW-like galaxy to date, with a detailed view of the SFR as a function of time over the past 500 Myr on 100 pc scales. M31 is uniquely placed to allow for study of this intermediate scale of star formation across a large contiguous area.

1.3 M31

The studies presented in this dissertation rely on the power of resolved stars. We can only resolve individual stars in the very Local Universe. The resolution enabled by resolved stars gives us the ability to examine astrophysical processes, such as star formation, in much greater detail than is available in more distant galaxies. As a result, the analysis done in the Local Universe can help to inform studies and findings of more distant galaxies.

Of the most nearby galaxies for which we have resolved stars, M31 is the closest analog we have to other nearby star-forming galaxies, such as those from the Sloan Digital Sky Survey. M31 is an ideal target in the effort to examine star formation on sub-galactic scales. As already discussed, its properties are similar to those of the MW, which allows us to better understand star formation processes in our own Galaxy as well. Its location opens up an intermediate scale of study that is only accessible in nearby galaxies.

1.3.1 Past Studies

Due to its proximity, M31 is a highly studied galaxy. Its SFH has been measured across the disk from the ground as well as in deep exposures of outer disk and halo fields (Williams 2002, 2003b; Brown et al. 2006, 2007, 2008; Bernard et al. 2012, 2015b,a). It has been imaged from the X-ray to the far-infrared with ROSAT, *Swift* UVOT, *GALEX*, *HST*, *Spitzer*, *Herschel*, and other telescopes. There are measurements of gas in CO and H I (e.g., Nieten et al. 2006; Braun et al. 2009). There is spectra of stars across the disk that have been used to study kinematics and structure (e.g., Dorman et al. 2012). It's star clusters are well-cataloged (Johnson et al. 2012, 2015).

The studies listed here are only a small piece of the literature related to star formation, and a tiny sliver of all available data in M31. This ancillary data enhances the use of resolved star data. It facilitates study of M31 and its comparison to more distant galaxies where such integrated light data is all that is available, and it enables more robust comparison with simulations.

1.3.2 The Panchromatic Hubble Andromeda Treasury

The work presented in this dissertation uses data from the Panchromatic Hubble Andromeda Treasury (PHAT) (Dalcanton et al. 2012; Williams et al. 2014) program. PHAT was a HST multi-cycle treasury program that imaged 1/3 of the star-forming disk of M31 in six filters, from the near-UV to the near-IR in 828 orbits. The result was a catalog with fluxes of 120 million stars, all at a common distance.

1.4 Dissertation Outline

This dissertation is organized as follows. Chapter 1 provides a brief introduction to the study of star formation in nearby galaxies and discusses some of the problems encountered in such studies. In Chapter 2, I present my measurement of the spatially-resolved SFH of M31 within the PHAT survey. I use these SFHs derived from optical CMDs to predict the ultraviolet (UV) flux in each region and I discuss a couple of uses for these predicted flux maps in Chapter 3. In Chapter 4, I present a method for using *GALEX* UV flux and dust-free UV flux predicted from the SFHs to examine variations in the attenuation curve across the disk of M31. I summarize the results of this dissertation and I discuss my plans for ongoing and future work in M31 and other galaxies in Chapter 5.

Throughout this dissertation, I use the pronoun 'we' to recognize the contributions from my coauthors and from the individuals of the PHAT collaboration. I was the lead investigator on each project, completed the analysis, and wrote up each paper.

Chapter 2

THE SPATIALLY-RESOLVED RECENT STAR FORMATION HISTORY OF M31

This chapter was published as A. R. Lewis et al. 2015, ApJ, 805, 183, and is reproduced by permission of the AAS.

We measure the recent star formation history (SFH) across M31 using optical images taken with the *Hubble Space Telescope* as part of the Panchromatic Hubble Andromeda Treasury (PHAT). We fit the color-magnitude diagrams in ∼9000 regions that are ∼100 pc × 100 pc in projected size, covering a 0.5 square degree area (∼380 kpc^2, deprojected) in the NE quadrant of M31. We show that the SFHs vary significantly on these small spatial scales but that there are also coherent galaxy-wide fluctuations in the SFH back to ∼500 Myr, most notably in M31's 10-kpc star-forming ring. We find that the 10-kpc ring is at least 400 Myr old, showing ongoing star formation over the past ∼500 Myr. This indicates the presence of molecular gas in the ring over at least 2 dynamical times at this radius. We also find that the ring's position is constant throughout this time, and is stationary at the level of 1 km s^{-1}, although there is evidence for broadening of the ring due to diffusion of stars into the disk. Based on existing models of M31's ring features, the lack of evolution in the ring's position makes a collisional ring origin highly unlikely. Besides the well-known 10-kpc ring, we observe two other ring-like features. There is an outer ring structure at 15 kpc with concentrated star formation starting ∼80 Myr ago. The inner ring structure at 5 kpc has a much lower star formation rate (SFR) and therefore lower contrast against the underlying stellar disk. It was most clearly defined ∼200 Myr ago, but is much more diffuse today. We find that the global SFR has been fairly constant over the last ∼500 Myr, though it does show a small increase at 50 Myr that is 1.3 times the average SFR over the past 100

Myr. During the last ∼500 Myr, ∼60% of all SF occurs in the 10-kpc ring. Finally, we find that in the past 100 Myr, the average SFR over the PHAT survey area is 0.28 ± 0.03 $M_\odot$ yr^{-1} with an average deprojected intensity of 7.3×10^{-4} $M_\odot$ yr^{-1} kpc^{-2}, which yields a total SFR of ∼0.7 $M_\odot$ yr^{-1} when extrapolated to the entire area of M31's disk. This SFR is consistent with measurements from broadband estimates.

2.1 Introduction

A galaxy's star formation history (SFH) encodes much of the physics controlling its evolution. It tells us about the evolution of the star formation rate (SFR) throughout the galaxy, the evolution of the mass and metallicity distributions, and the movement of stars within the galaxy. In addition to the global evolution, focusing on the recent SFH (<1 Gyr) reveals the relationships between stars and the gas and dust from which they form and can be used to constrain models of star formation (SF) propagation and/or dissolution. For this type of study to be possible, however, we first need a spatially-resolved view of the past SFH with sufficient resolution to probe the relevant physical scales.

Broad SFH constraints can be derived by looking at the properties of the galaxy population across cosmic time. However, examining the integrated properties of distant galaxies provides limited information on how individual galaxies form and evolve. While such integrated light studies benefit from large sample sizes, the final results are limited to conclusions about the SFHs of general galaxy types (e.g., based on bins of mass, luminosity, or color), and cannot say anything definitive about the physics that controls the evolution of individual galaxies.

To appropriately examine the evolution of individual galaxies, it is necessary to study well-resolved nearby galaxies for which there exists large amounts of ancillary data. With such data, one can, for example, analyze the relationship between star SF and gas in the spatially-resolved Kennicutt-Schmidt law (e.g., Kennicutt et al. 2007; Bigiel et al. 2008), understand the evolution of a galaxy's gas reservoir (e.g., Leroy et al. 2008; Schruba et al. 2010; Bigiel et al. 2011; Leroy et al. 2013), and calibrate SFR indicators (e.g., Calzetti et al.

2007; Li et al. 2013), among many others. However, these studies have historically been restricted to using only the current SFR where 'current' is the average over some timescale characteristic of a given SFR indicator. These studies, therefore, cannot probe the evolution of these relationships with time or on small physical scales where the SFR indicators break down (e.g., Leroy et al. 2012).

For a more detailed analysis of the recent SFH, resolved stellar populations are the gold standard. Using individual stars, we can examine the evolution of a galaxy archaeologically by analyzing the color-magnitude diagram (CMD) as a function of position within the galaxy. Embedded within the CMD is the history of SF and metallicity evolution of the galaxy. Although recovering this information is not completely assumption-free (we must make choices about the initial mass function (IMF), stellar models, constancy of SFR within time bins, etc), it is the only way to make a time-resolved measurement of the SFR. It also has the ability to recover the SFR on much finer physical scales.

CMD fitting has most often been used to probe low mass galaxies (e.g., Gallart et al. 1999; Harris & Zaritsky 2004; Cole et al. 2007; Harris & Zaritsky 2009; Monelli et al. 2010; Weisz et al. 2011; Monachesi et al. 2012; Weisz et al. 2014) because they are the most numerous type of galaxy in the Local Volume, which is one of the few places where galaxies can be sufficiently well resolved. The technique has been used to examine a few individual larger galaxies (e.g., Wyder et al. 1998; Hernandez et al. 2000; Bertelli & Nasi 2001; Williams 2002, 2003b; Brown et al. 2006, 2007, 2008; Williams et al. 2009, 2010; Gogarten et al. 2010; Bernard et al. 2012, 2015b), but these studies have been limited to either small fields spread across the disk and/or halo or have low spatial resolution such that it is difficult to pick out detailed features present in the galaxy. This technique has never been used to contiguously and uniformly recover the recent SFH of an $L_\star$ galaxy with high resolution.

In this paper, we present the first finely spatially-resolved recent SFH of a significant part of the $L_\star$ galaxy, Andromeda (M31). M31 has been the target of many photometric (e.g., Brown et al. 2006; Barmby et al. 2006; Gordon et al. 2006; Dalcanton et al. 2012; Bernard et al. 2012; Ford et al. 2013; Sick et al. 2014) and spectroscopic (e.g., Ibata et al.

2004; Guhathakurta et al. 2006; Kalirai et al. 2006; Koch et al. 2008; Gilbert et al. 2009; Dorman et al. 2012; Gilbert et al. 2014) studies due to its proximity and similarity to the Milky Way. M31 is the ideal place to examine processes in $L_\star$ galaxies; it is close enough to be well resolved into stars with the *Hubble Space Telescope* (*HST*) but does not not face the same obstacles as studies in the Milky Way, which are plagued by uncertainties due to line-of-sight reddening and challenging distance measurements.

We generate maps of the recent (<0.5 Gyr) SFH in M31 using resolved stars from recent observations of M31 taken as part of the Panchromatic Hubble Andromeda Treasury (PHAT; Dalcanton et al. 2012). While other studies have examined the SFH in M31 using resolved stars (Williams 2003b; Brown et al. 2006, 2007, 2008; Davidge et al. 2012; Bernard et al. 2012), none have been as finely resolved as the work we present here.

With the resulting spatially- and temporally-resolved recent SFHs, we can see where stars form within the galaxy and how that SF evolves across the galaxy, whether it's a single star-forming event or propagation across the disk. The maps also provide clues about the evolution of spatial structure on a variety of different scales; while we know a great deal about small-scale SF within molecular clouds and large-scale SF within the galactic environment, the maps we derive bridge these two scales. Recent SFHs also enable the analysis of fluctuations in the recent SFR. This is especially significant for SF relations, such as the Kennicutt-Schmidt relation (Schmidt 1959; Kennicutt 1989), which often assumes a constant SFR over the timescale of the tracer used. While this paper deals only with the SFHs themselves, it is the first in a series of papers on the SF, dust, and ISM contents of M31 on small spatial scales (Lewis et al., in prep).

This paper is organized as follows: We describe the data used in Section 2.2. In Section 2.3, we explain the method by which we recover the SFHs in each region. We present the resulting SFH maps in Section 2.4 and discuss features of the maps in Section 2.5. We summarize the results in Section 2.6.

2.2 PHAT Data

We derive the spatially resolved SFHs using photometry from the PHAT survey. PHAT surveyed the northeast quadrant of M31 in six filters, from the near-UV to the near-IR, measuring the properties of ∼117 million stars. Full details of the survey can be found in Dalcanton et al. (2012) and the photometry is described in Williams et al. (2014). Figure 2.1 shows a 24 μm image (Gordon et al. 2006) of M31 with the PHAT footprint overlaid. In this paper, we examine the SFH inside the solid red region; we have excluded the region closest to the bulge (black dashed line) where crowding errors are large and the depth of the CMD is shallow, making reliable CMD fitting difficult.

2.2.1 Photometry and Creation of Single-Brick Catalogs

We use optical photometry (F475W and F814W filters) from the `.gst` catalogs, which were compiled following procedures developed by Dolphin (2000) as described in Dalcanton et al. (2012). The stars in this catalog have S/N > 4 in both filters and pass stringent goodness-of-fit cuts. These cuts leave stars with the highest quality photometry but with higher incompleteness in more crowded regions. The incompleteness is worse in the inner galaxy (inside ∼3 kpc), which we exclude from our analysis, and also affects the centers of stellar clusters. This latter limitation is not a problem for this paper because clusters contain only a few percent of the recent SF (Johnson et al., in prep.). Moreover, we are interested in the SFHs of the field stars, and picking out stars in the centers of dense stellar clusters is not necessary.

The survey was split into 23 regions called 'bricks'; each brick is ∼1.5 kpc × 3 kpc in projected size. Odd-numbered bricks extend from the galactic center to the outer disk along the major axis. Even-numbered bricks sit adjacent to them at larger radii along the minor axis. Each brick is subdivided into 18 'fields', each with a (projected) size of ∼500 pc × 500 pc. In the optical, adjacent fields overlap to cover the ACS chip gap. The SFHs presented in this paper are derived on a brick-by-brick basis. To create a single brick catalog from the 18

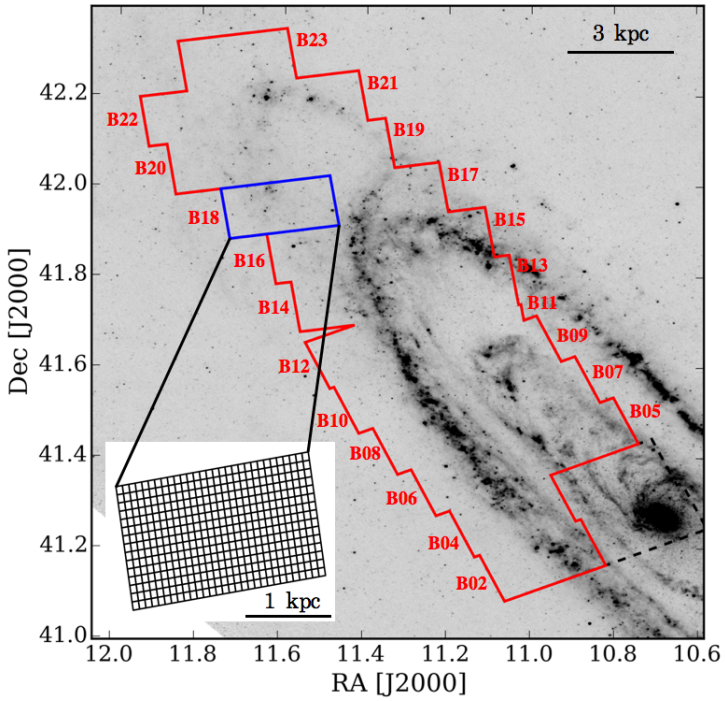

Figure 2.1 The PHAT NIR footprint overlaid on a 24 μm image (Gordon et al. 2006) of M31. The thick red line denotes the area for which we compute SFHs in this paper. We have left out the regions closest to the bulge along the major axis (dashed black line) because crowding errors are large and CMD depth is shallow, which makes fitting a reliable SFH difficult. The inset shows an example of our binning scheme, shown here for Brick 18, which is outlined in blue. We have included scale bars for the large image as well as for the inset. The bricks are labeled with their numbers just exterior to the brick outline. We use these brick numbers throughout the text. The image is oriented such that north is up and east is to the left.

'field' catalogs, we use the smaller IR brick footprint divided into 18 non-overlapping regions which roughly describe the IR field footprints. In each of these fields, we select all of the stars in the corresponding optical catalog that fall within the IR field boundaries. We fill in the chip gap using two adjacent fields, selecting only the stars that fall within the desired portion of the chip gap. Three fields in Brick 11 were not observed; this area is completely covered by overlap from Brick 09 so that there is continuous coverage over the survey area.

The result of this process is the creation of a single brick catalog of all stars detected in the optical filters that fall within the IR footprint, filling in the chip gap and eliminating duplication of stars in the overlap regions. We then grid each brick into 450 approximately equal sized, non-overlapping regions that are ∼100 pc × 100 pc in projected size for a total of ∼9000 regions across the survey area. In Figure 2.1, B18 is outlined in blue. The inset shows the binning scheme used within each brick.

2.2.2 Artificial Star Tests

Even with the resolution of *HST*, crowding in regions of high stellar density can strongly affect the photometry. Many faint stars cannot be resolved in the dense field of brighter stars. In addition, faint stars, that would otherwise not be detected, are biased brighter by blending with neighboring stars. This also affects brighter stars, but to a lesser degree.

To characterize photometric completeness and to account for the observational errors that result from crowding, we perform extensive artificial star tests (ASTs). Briefly, we insert fake stars into each image and run the photometry as normal. We then test for recovery of these fake stars and measure the difference between the input and recovered magnitude if a star was detected. We adopt the magnitude at which 50% of the stars are recovered as our limiting magnitude when solving for the SFHs. The completeness limits used for each brick are given in Table 2.1.We refer the reader to Dalcanton et al. (2012) for further details.

We inserted ∼100,000 artificial stars individually into each ACS field-of-view. We combined the resulting ASTs into brick-wide catalogs in the same way as the photometry. When running the SFHs for a given 100 pc region, we select the fake stars from a 5×5 grid of ad-

jacent regions, such that the ASTs come from a 500×500 pc^2 region centered on the region of interest. Each of these larger regions contains the results of ∼50,000 ASTs.

2.3 Derivation of the Star Formation Histories

We derive SFHs using only the optical data from the F475W and F814W filters. These filters provide the deepest CMDs and the greatest leverage for the recent SFHs of interest in this paper. A more detailed discussion of our filter choice can be found in Appendix 2.7.1.

2.3.1 Fitting the Star Formation History

We derive the SFHs using the CMD fitting code `MATCH` described in Dolphin (2002). The user specifies desired ranges in age, metallicity, distance, and extinction. The code also requires a choice of IMF and a binary fraction. It then populates CMDs at each combination of age and metallicity, convolved with photometric errors and completeness as modeled by ASTs. The individual synthetic CMDs are linearly combined to form many possible SFHs. Each synthetic composite CMD is compared with the observed CMD via a Poisson maximum likelihood technique. The synthetic CMD that provides the best fit to the observed CMD is taken as the model SFH that best describes the data. For full implementation details, see Dolphin (2002).

The fit quality is given by the `MATCH` *fit* statistic: $fit = -2 \ln L$, where L is the Poisson maximum likelihood. We estimate the $n\sigma$ confidence intervals as $n^2 \geq fit - fit_{\rm min}$; the 1σ confidence interval includes all SFHs in a given region with $fit - fit_{\rm min} \leq 1$, the 2σ confidence interval includes all SFHs with $fit - fit_{\rm min} \leq 4$, etc.

We use a fixed distance modulus of 24.47 (McConnachie et al. 2005), a binary fraction of 0.35 with the mass of the secondary drawn from a uniform distribution, and a Kroupa (2001) IMF. We solve the SFH in 34 time bins covering a range in log time (in years) from 6.6 to 10.15 with a resolution of 0.1 dex except for the range of log(time) = 9.9 – 10.15 which we combine into one bin. This time binning scheme was chosen to provide as much time resolution as possible while minimizing computing time. We found that using a

Table 2.1. 50% Completeness Limits and Isochrone Shifts

Brick Number	m_{F475W} (mag)	m_{F814W} (mag)	$\sigma_{\log T_{eff}}$	$\sigma_{M_{bol}}$
02	27.2	26.1	0.019	0.22
04	27.1	25.9	0.019	0.21
05	26.4	25.0	0.019	0.18
06	27.2	26.0	0.019	0.22
07	26.8	25.4	0.019	0.18
08	27.2	26.0	0.019	0.22
09	27.1	25.8	0.019	0.21
10	27.2	26.1	0.019	0.23
11	27.1	25.9	0.019	0.21
12	27.3	26.2	0.019	0.24
13	27.2	26.1	0.019	0.23
14	27.3	26.2	0.019	0.24
15	27.4	26.2	0.019	0.25
16	27.4	26.4	0.019	0.26
17	27.5	26.4	0.020	0.26
18	27.8	26.7	0.020	0.29
19	27.6	26.7	0.020	0.28
20	27.8	26.9	0.020	0.30
21	27.8	26.9	0.020	0.30
22	27.8	26.9	0.020	0.30
23	27.8	26.9	0.020	0.30

Note. — Column 1 contains the brick number. Columns 2 and 3 list the 50% completeness limits in F475W and F814W, respectively. Columns 4 and 5 contain the shifts in log T_{eff} and M_{bol} used when computing the systematic uncertainties.

finer time binning scheme with a resolution of 0.05 dex increased the computing time by at least a factor of two and only resulted in differences in the SFHs of $\sim$1%, which is much smaller than systematic and random uncertainties. We use the Padova (Marigo et al. 2008) isochrones with updated AGB tracks (Girardi et al. 2010). The [M/H] range is [-2.3, 0.1] with a resolution of 0.1 dex. Because we are limited by the depth of the data, which does not reach the ancient main sequence turnoff, we also require that [M/H] only increases with time. We limit the oldest time bin to have [M/H] between -2.3 and -0.9 and the youngest time bin to have [M/H] between -0.4 and 0.1.

M31 contains significant amounts of dust (e.g., Walterbos & Schwering 1987; Draine et al. 2014; Dalcanton et al. 2015), which, broadly speaking, can be described by three components: a mid-plane component due to extinction internal to M31 that dominates the older, well-mixed stellar populations, a foreground component due to Milky Way extinction, and a differential component that affects the star-forming regions. In addition to the SFH, `MATCH` allows two free parameters to describe the dust distribution: a foreground extinction (A_V) and a differential extinction (dA_V) which describes the spread in extinction values for the stars in each region. The differential extinction is a step function starting at A_V with a width given by the value of dA_V. While foreground extinction is expected to be relatively constant across the galaxy, differential extinction can vary significantly from region to region as they probe very different star-forming and stellar density environments. To determine the best fit to the data, we search extinction space to find the combination of A_V and dA_V that best fits the data. However, the distribution of dust is different for young stars and old stars (e.g., Zaritsky 1999). The step function differential extinction model provides a good fit to the main sequence (MS) component, but it cannot reproduce the post-MS stellar populations.

We mitigate the effects of dust on our SFHs by simplifying the fitting process such that we exclude the redder portions of the CMD from the fit. Specifically, we have adopted the cuts in Simones et al. (2014), excluding all stars with F475W-F814W>1.25 and F475W>21 (shaded regions of the CMDs in Figures 2.2 and 2.3). This prevents contamination from

the older populations. We therefore avoid extinction-related complications by excluding the RGB and the red clump, which is often poorly fit with a single step function, and which is not relevant when calculating the recent SFH.

We note that age-metallicity degeneracy is an important concern in any kind of SFH work. When modeling composite CMDs, it primarily affects the RGB (e.g., Gallart et al. 2005), which we do not fit in this analysis. Instead, the vast majority of stars in the CMD are main sequence stars, for which the age-metallicity degeneracy is negligible compared to typical photometric uncertainties. In addition, the metallicity gradient of M31 has been extensively studied and found to be very shallow (e.g., Blair et al. 1982; Zaritsky et al. 1994; Galarza et al. 1999; Trundle et al. 2002; Kwitter et al. 2012; Sanders et al. 2012; Balick et al. 2013; Lee et al. 2013; Pilyugin et al. 2014, Gregersen et al. in prep), and the age range we are fitting is small. As a result, we are not concerned that the age-metallicity degeneracy affects the results in this paper.

We compute the SFH in 450 regions per brick for 21 of the 23 bricks in the PHAT survey. To determine the best-fit SFH, we solve multiple SFHs with different combinations of A_V and dA_V, where the best-fit SFH is chosen to be the one whose combination of A_V and dA_V minimizes the fit value as given by the maximum likelihood technique. Consequently, for each of our regions, we must compute many possible SFHs. We minimize the total number of SFHs that must be run using an optimization scheme to limit the size of (A_V, dA_V) space that must be searched, as discussed in Appendix 2.7.2. Based on this optimization, we set a constraint that $A_V + dA_V \leq 2.5$. In each region, we run a grid of SFHs in (A_V, dA_V) space with a step size of 0.3 over the range of $A_V = [0.0, 1.0]$, also requiring that $A_V + dA_V \leq 2.5$. We take the resulting SFH with the best fit, determine the two-sigma range around that best (A_V, dA_V) pair, and then sample the grid in that region down to a finer spacing of 0.1 in A_V and dA_V. Not only does this ensure that we are finding the global minimum, but it also allows us to account for the uncertainty in extinction in the SFHs by including all fits in the result. In addition, the extinction parameters provide us with an additional method to verify our results, as we discuss in Section 2.3.2.

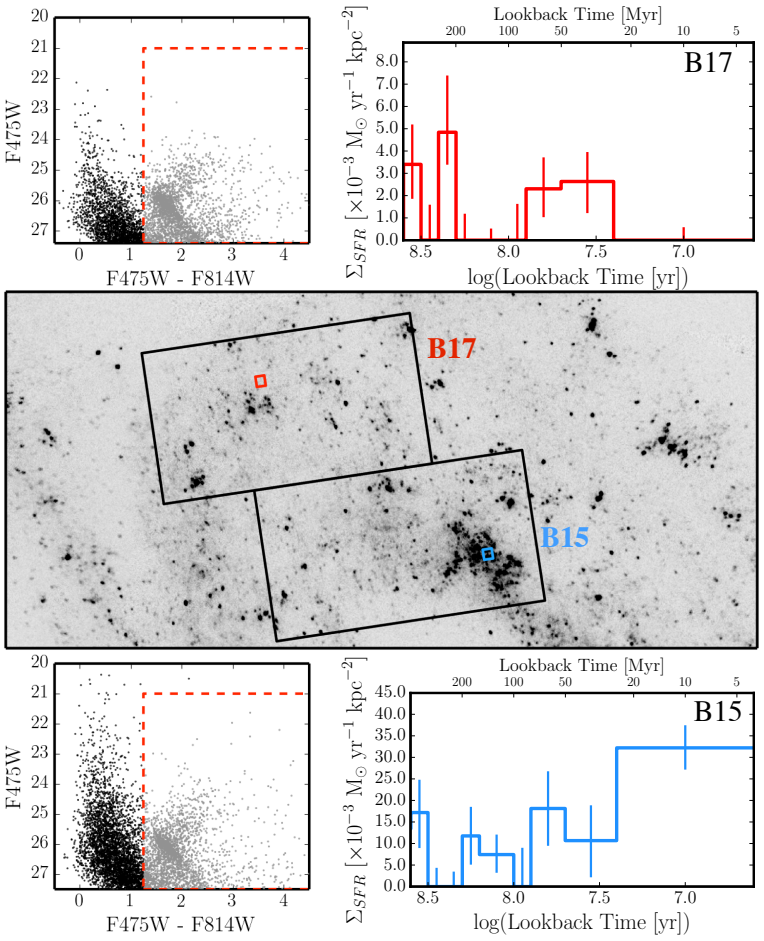

Figure 2.2 Here we show example results for two different regions, one in Brick 15 sitting on a bright star-forming region (blue, lower) and the other in B17 in a more quiescent spot (red, upper). We have overlaid the outlines of Bricks 15 and 17 on top of a GALEX FUV image (Gil de Paz et al. 2007). The individual region outlines are also shown. For each region, we show the CMD, with the stars that we fit in black and those that we don't in gray and outlined with red dashes, and the SFH to illustrate the differences on these small scales. The SFHs have been binned into 25 Myr increments below 100 Myr and 50 Myr increments above 100 Myr, as the native time resolution (0.1 dex) allows. Both of these regions have fairly recent SF as can be seen by the well-defined MS in each CMD, though the blue region (B15) shows ongoing and more intense SF. Surface densities are calculated using deprojected areas and assuming an inclination of 77° (Brinks & Burton 1984).

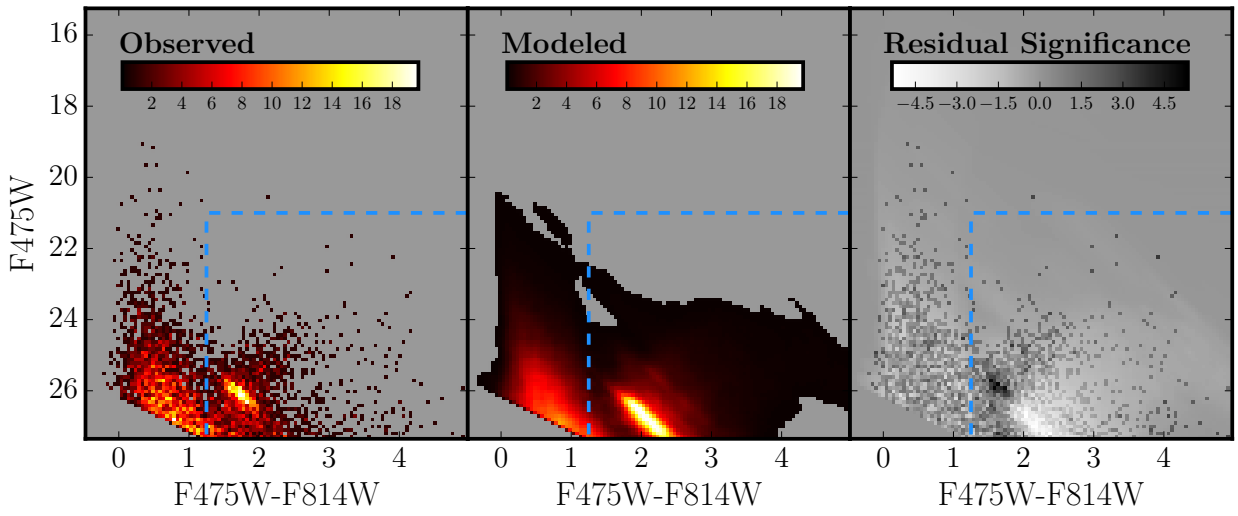

Figure 2.3 The fit of a region in Brick 15. This is the same region as shown in Figure 2.2. The left panel shows the data, the middle shows the best-fit model for the data, and the right shows the significance of the residuals (the observed CMD minus the modeled CMD, weighted by the variance) between the model and the data. All data inside the region outlined by the blue dashed line is masked out of the fit. In the left two panels, the color bars indicate the number of stars in each bin. In the right panel, the color bar indicates the significance of the residuals. In the residuals panel, darker colors generally indicate more stars in the data than in the model, lighter colors indicate more stars in the model than in the data. The lack of systematic residuals in the area that we fit is an indication that the model fits the data well.

As an example, in Figure 2.2 we plot the CMDs and SFHs for two of the regions found near the 10-kpc ring. We show the location of these regions over-plotted on a *GALEX* FUV image (Gil de Paz et al. 2007). The top region, in Brick 17, is located just off of a spur of the 10-kpc ring. The region itself shows very little FUV emission, and the resulting SFH is sparse with only moderate SFRs at all times. The lower region falls directly on an OB association (OB 54; van den Bergh 1964) in Brick 15. As expected, there is elevated, ongoing SF in that region over at least the past 100 Myr. The CMDs for each of these regions show a well-defined MS. The consequences of dust are very evident in the region but are most easily seen in the part of the of the CMD that we do not fit, where the red clump is elongated along the reddening vector.

We note that the Padova isochrones do not include tracks younger than 4 Myr. In the resulting SFHs, we renormalize the SFR in the youngest time bin to reach the present day (0 Myr), conserving the total mass formed in that time bin.

In Figure 2.3, we show the observed CMD, the best-fit modeled CMD, and the significance of the residuals (the observed CMD minus the modeled CMD with a weighting determined by the variance) for a region in Brick 15. We fit all stars that are outside the blue dashed region, which are primarily MS stars, with a smattering of short-lived blue helium-burning stars. The residuals show no distinct features, which means the model is a good fit.

2.3.2 Extinction

In this section we discuss how we incorporate IR-based dust maps as a prior in determining our dust parameters. After determining the best-fit SFH in each region as described in Section 2.3.1, we conducted additional verification by examining the map of total dust, $A_V + dA_V$.

We found that there were a handful of regions in which the best-fit required large amounts of dust, at or very close to the limit of 2.5 mag in spite of there being no evidence for SF within the last 100 Myr, based on a lack of luminous MS stars and low SFR averaged over the most recent 100 Myr. In these regions, we would expect very little dust because there

are no dust-enshrouded young stars. Bad fits result in these cases because there are few stars in the MCD fitting region that can be used to constrain the dust.

To examine this discrepancy, we compared our dust parameters with the total dust mass in each region, as measured by Draine et al. (2014). We correct the low-SFR, high-dust regions by constructing a prior on $A_V + dA_V$ based on the Draine et al. (2014) dust mass maps and multiplying the prior by the likelihood calculated by `MATCH`. The details of the prior are described in Appendix 2.7.3. After applying the prior, we compute new fits for all of the SFHs measured in each region. We use these new fits to go back through A_V, dA_V parameter space to be sure that we properly sampled 2-σ space around the new best-fits for each region. As a result, we were able to constrain the `MATCH` dust parameters in the regions of very-low SFR that are not properly anchored in the CMD analysis. Ultimately, because application of the prior primarily affects the very-low SFR regions, this processing did not significantly affect the SFH results of this paper.

2.3.3 Uncertainties

There are three significant sources of uncertainties that affect the measured SFHs: random, systematic, and dust. In this section, we discuss each source of uncertainty in turn.

First, we consider random uncertainties. The random uncertainties are dominated by the number of stars on the CMD and are consequently larger for more sparsely populated CMDs. Random uncertainties were calculated using a hybrid Monte Carlo process (Duane et al. 1987), implemented as described in Dolphin (2013). The result of this Markov Chain Monte Carlo routine is a sample of 10,000 SFHs with density proportional to the probability density, i.e., the density of samples is highest near the maximum likelihood point. Error bars are calculated by identifying the boundaries of the highest-density region containing 68% of the samples, corresponding to the percentage of a normal distribution falling between the $\pm 1\sigma$ bounds. This procedure provides meaningful uncertainties for time bins in which the best-fitting result indicates little or no star formation.

Next, we consider the systematic uncertainties. Systematic uncertainties reflect deficien-

cies in the stellar models (i.e., uncertainties due to convection, mass loss, rotation, etc.; Conroy 2013) such that different groups model these parts of stellar evolution differently, which leads to discrepant results for the same data, depending on the stellar models used (Gallart et al. 2005; Aparicio & Hidalgo 2009; Weisz et al. 2011; Dolphin 2012). These uncertainties primarily affect older populations that have evolved off the MS. The stellar models of the various groups generally agree quite well for MS stars that dominate our adopted fitting region.

Because we have used the same models across the whole survey, all regions experience similar systematic effects. We have estimated the size of the systematics for a number of regions, covering the range of stellar environments within M31. We computed the systematic uncertainties by running 50 Monte Carlo realizations on the best-fit SFHs as described in Dolphin (2002). For each run, we shifted the model CMD in $\log(T_{\rm eff})$ and $M_{\rm bol}$ by an amount taken from a random draw from a Gaussian with sigma listed in Table 2.1. These shifts are designed to mimic differences in isochrone libraries. We then measured the resulting SFH. The range that contained 68% of the distributions from all 50 realizations is designated as the systematic uncertainties. The relative size of the systematics varies greatly from region to region but is generally less than half the size of the random uncertainties in individual regions and increases at larger lookback time. There is also more variation in the relative size of the uncertainties in the ring features than in the outermost regions where both the stellar density and the SFR are low.

Finally, the variable internal dust content introduces uncertainties. We select the best-fit SFH by choosing the (A_V, dA_V) pair that maximizes the likelihood. However, there are regions where the difference between the fit values of the two most likely SFHs is very small (i.e., both SFHs are almost equally likely). We also sample to a minimum spacing of only 0.1 in A_V and dA_V, and thus may have determined a slightly different best-fitting SFH than if we had sampled A_V, dA_V space more finely. To account for these variations, we calculate our uncertainties due to the dust distribution by combining all SFHs measured in a given region and determining the range that contains 68% of the samples. In this combination,

the SFHs are weighted by their fit values such that the best-fit gets full weight and the $n\sigma$ fits are weighted by $e^{-0.5\,n^2}$ (e.g., SFHs with fit values that are 2σ from the best-fit value are weighted by $e^{-0.5\times 2^2}$, or e^{-2}).

A possible additional source of uncertainty is due to the choice of binary fraction, which is a free parameter in this analysis. We tested the effect of different binary fractions in two of our regions and found that the final fit is not very sensitive to binary fraction. This is because the inclusion of binaries in the model results in a color separation on the CMD that is washed out by dust. The fits and resulting SFHs are consistent with the uncertainties when choosing a binary fraction anywhere between about 0.2 and 0.7. This insensitivity of the SFH to binary fraction is consistent with more extensive tests presented in Monelli et al. (2010). Uncertainties due to binary fraction will be much smaller than those due to dust.

We note that we do not include the model systematics in our reported uncertainties. While there may be absolute uncertainties in the global SFR due to model uncertainties, the relative region-to-region uncertainties are dominated by the random and dust components.

2.3.4 Choice of Region Size

To generate the spatially-resolved SFH of M31, we divide each of the brick-wide catalogs into regions that are approximately 100 pc (projected; $25''$) on a side, assuming a distance of 783 kpc to M31. There were a few different considerations for this size.

Regions of this size are of scientific interest because they bridge the gap between existing knowledge of Galactic pc scale SF (e.g., Bate 2009; Schruba et al. 2010) and SF in more distant galaxies on kpc scales (e.g., Leroy et al. 2008). The resolution is also fine enough to resolve features such as large HII regions and giant molecular clouds.

While a finer grid would also be scientifically interesting, there are a couple of difficulties to consider. The main problem is that smaller regions would have insufficiently populated CMDs, increasing the random uncertainties of the SFHs to unacceptable levels. With our adopted $\sim$100 pc bin size, the number of stars within the CMD fitting region ranges from 110 to 3900. In 93% of the regions, we fit more than 500 stars, and in 80% we fit more than

1000 stars. Additionally, the SFHs are computationally expensive to run. For each region, MATCH must be run multiple times to determine the (A_V, dA_V) pair that provides the best fit to the data. Moving to 50 pc size regions would have resulted in four times as many regions, significantly increasing the time needed to derive the SFHs. Even at our 100 pc grid size, deriving the SFHs and uncertainties for the entire sample required more than 500,000 CPU hours using XSEDE resources (Towns et al. 2014).

Our overall technique is similar to that of Simones et al. (2014), who measured the SFHs of UV-bright regions within Brick 15 of the PHAT survey. Their goal was to convert the SFHs into FUV fluxes and compare with the observed fluxes in each star-forming region. About half of their regions had fewer than 500 stars on the part of the CMD they were fitting but they still found reasonable agreement between the modeled and observed fluxes. This agreement indicates that the CMD fitting routine is robust, even with a modest number of stars in the part of the CMD occupied by young stars.

2.3.5 Reliability of the SFHs as a Function of Lookback Time

We have excluded the red side of the CMD in our SFH recovery process, so consequently, our fits are not sensitive to old stellar populations. The exact age at which sensitivity is lost is set by the oldest stars observable on the MS, which varies with stellar density and dust extinction.

We perform two different tests to examine the sensitivity of our results as a function of time. First, we create artificial CMDs using MATCH. The CMDs are generated with a constant SFH and solar metallicity, while modeling observational uncertainties by using the results of the ASTs in each region. The results are shown in Figure 2.4, where we plot simulated CMDs. The youngest stars are shades of blue, and all stars older than 1 Gyr are red. Each of the top three rows shows a CMD at a different depth, where the top row is the shallowest CMD closest to the bulge (B05), and the third row is the deepest in B23. The brick numbers are indicated in the left panel. The columns display varying amounts of extinction, which is applied to the CMD in the same way we apply it to the model CMDs when recovering our

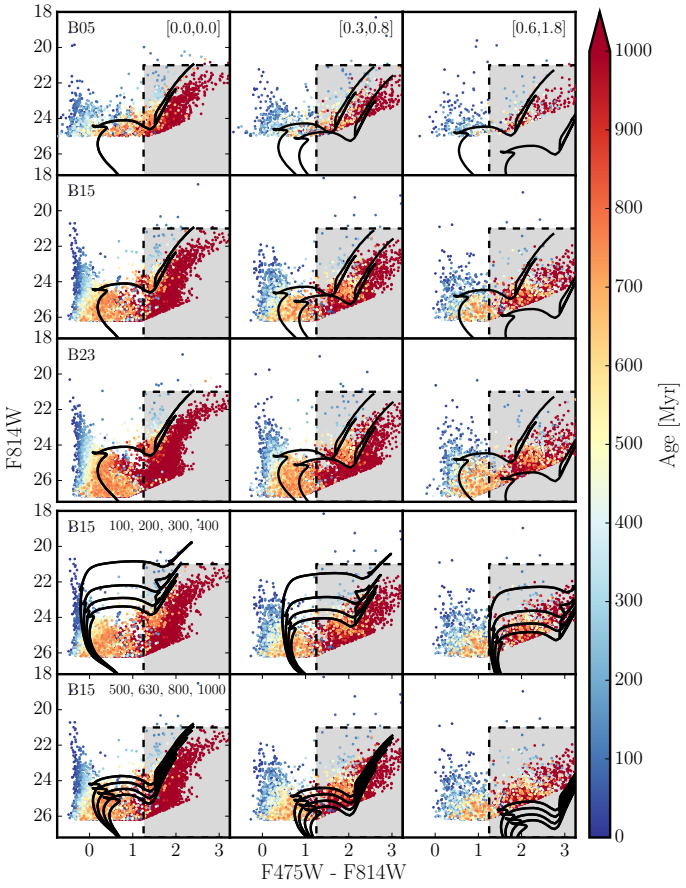

Figure 2.4 Artificial CMDs over a range of extinction and photometric depth, assuming a constant SFH, solar metallicity, and three different extinction values; one low: [A_V, dA_V] = [0.0,0.0], one typical of our SFHs: [A_V, dA_V] = [0.3,0.8], and one high: [A_V, dA_V] = [0.6,1.8], shown in the left, middle, and right columns, respectively and labeled in the upper right corner of the top panel of plots. The brick number listed in the left panel of plots indicates the depth of the corresponding row. Within each panel, individual stars are color-coded by age. All stars older than 1 Gyr are dark red. In the top 3 rows, we have over-plotted 630 Myr, solar metallicity isochrones, one attenuated by A_V, and the second attenuated by $A_V + dA_V$. Individual stars within the CMD will be reddened to somewhere between the two isochrones. Increased extinction reddens some stars off of the MS and into the region we do not fit in the SFH recovery process (shaded gray). The bottom two rows each have isochrones of 4 different ages over-plotted. The ages are listed in the left panel.

SFHs. Extinction is labeled in the top panel by [A_V, dA_V]. The left column is un-reddened, the middle column shows the effect of the median extinction found in each of our regions ([A_V, dA_V] = [0.3, 0.8]), and the right column shows the upper limit of extinction allowed in our SFHs. We also check the sensitivity by over-plotting isochrones of a single age (630 Myr) and solar metallicity. The isochrone in the first column has not been reddened. In the second and third columns of the first three rows, we plot two isochrones, one extincted by A_V and one extincted by $A_V + dA_V$. Individual stars can be extincted to anywhere between the two isochrones.

The variation in depth is large across the survey. The inner regions are very crowded and as a result the photometric depth is quite shallow. In Brick 05, where there is high crowding and moderate levels of extinction, we cannot detect many stars that are older than ∼500 Myr. As we move further away from the center of the galaxy, crowding and extinction generally decrease and we can probe stars that are 700 – 1000 Myr old (row 3 of Figure 2.4). The exception, of course, is the 10-kpc ring, where extinction can be high; the CMDs in the second row of Figure 2.4 mimic the conditions found in these regions. At low or mid-range extinction, we still see many stars on the MS that are at least 600 – 700 Myr old. As we increase the extinction, many of these stars are reddened into the portion of the CMD that we do not fit, as can also be seen from the isochrones. Unreddened 630 Myr old stars are easily recovered; however, stars that have the highest level of extinction applied to them are entirely reddened into the neglected portion of the CMD.

In the last two rows, the colored CMD is identical to that in the second row (B15 depth). Here, though, we plot solar metallicity isochrones of different ages: the fourth row has isochrones of 100, 200, 300, and 400 Myr while the bottom row shows isochrones of 500, 630, 800, and 1000 Myr. From these tests, we can see that there will be a number of regions that are reliable back to 1 Gyr, while others that are more extincted may only have a handful of stars that are more than ∼500 Myr old.

Ultimately, due to the wide variety of stellar environments found across the survey, not all bricks can reliably cover the same age range. The inner regions are much more crowded

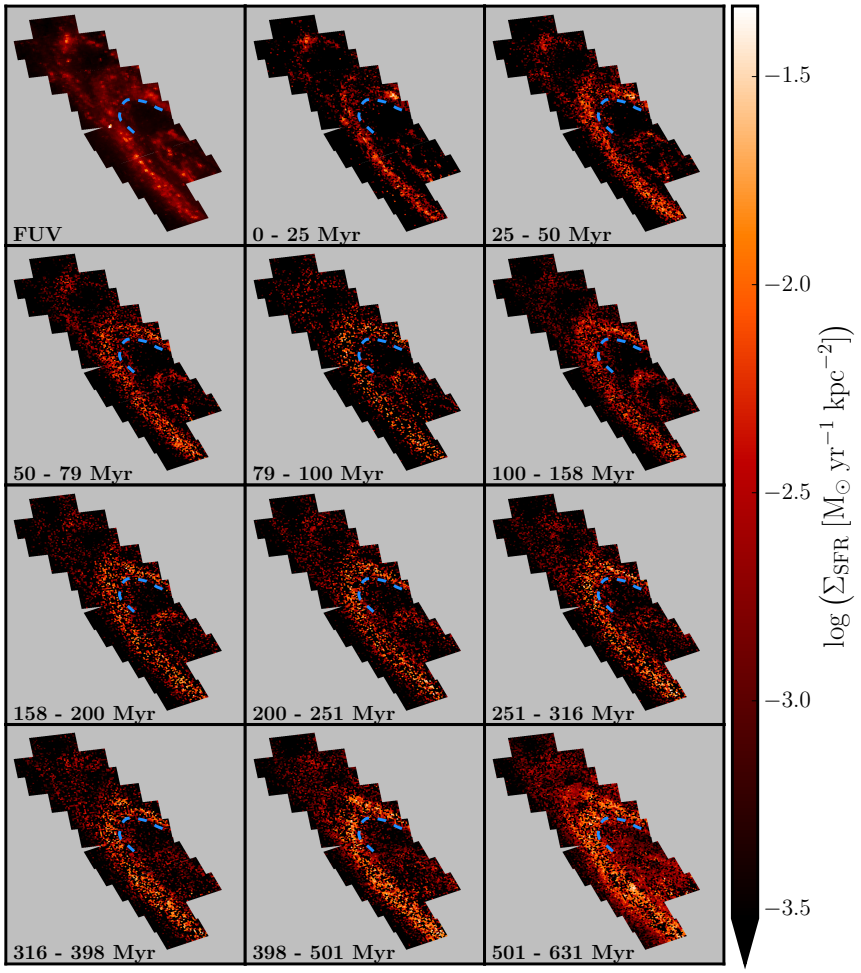

Figure 2.5 Map of the SFH of M31 covered by the PHAT survey. Each region is colored according to its SFR surface density in each time bin. We have applied a lower cut at a $\Sigma_{\rm SFR}$ of 10^{-4} $M_\odot\,{\rm yr}^{-1}\,{\rm kpc}^{-2}$ in order to highlight structure in the image. The time range covered is shown in the lower left of each plot. The plot in the top left shows the *GALEX* FUV image, smoothed to the same physical scale as our SFHs for better comparison. A blue dashed curve is over-plotted on each panel to aid the eye in recognizing structural change between timebins. The maps are oriented as in Figure 2.1. *Note*: We have included the time bins from 400 Myr to 600 Myr for illustrative purposes only. As discussed in Section 2.3.5, the SFHs in these time bins are much less certain in the crowded inner regions and in the dusty ring than they are in the outer parts of the disk.

and have shallower completeness limits than the outer regions; as a result, the age limit for regions closest to the bulge is only 400 Myr. Regions that fall within the ring and spiral arm features are much more extincted than other regions; although the completeness limit is deeper, stars may be reddened into the region of the CMD that we do not fit. These regions have an age limit of no more than 500 Myr. In the outer regions where extinction and crowding are less, the completeness limit is much deeper and the SFHs are reliable back to 700 – 1000 Myr. We therefore choose a conservative age limit of 400 Myr for consistency across the survey. For all scientific analysis, we examine only the most recent 400 Myr. In some of the plots that follow, we include results back to 630 Myr for illustrative purposes, with the caveat that they are only relevant for the outermost regions of the survey.

2.4 Results

We now present the results of the SFH fitting process.

2.4.1 Star Formation Rate Maps

We combine the single best-fit SFHs in each region into maps of $\Sigma_{\rm SFR}$ as a function of time. As an ensemble, they reveal the recent SFH of M31 in the PHAT footprint over the last 630 Myr. This SFH is shown in Figure 2.5. Each panel displays the SFR surface density within the time range specified in the lower left corner. We note that these time bins are not the native resolution of $\Delta(\log t) = 0.1$; instead, we have binned the results within the most recent 100 Myr into ∼25 Myr bins. This helps to expose the continuous structure, especially in the most recent 25 Myr when SF is very low across the galaxy. The regions are colored according to $\Sigma_{\rm SFR}$ in that region during the given time range. To more clearly illuminate the structure, we have placed a lower limit on the SFRs visible within this map such that all regions with $\Sigma_{\rm SFR}$ lower than 10^{-4} $M_\odot\,{\rm yr}^{-1}\,{\rm kpc}^{-2}$ are colored black. We have also over-plotted a blue dashed line on each image to aid the eye in recognizing structural evolution between time bins. There is little large-scale change over the last ∼500 Myr. The upper left panel shows the *GALEX* FUV image smoothed to the same physical scale as

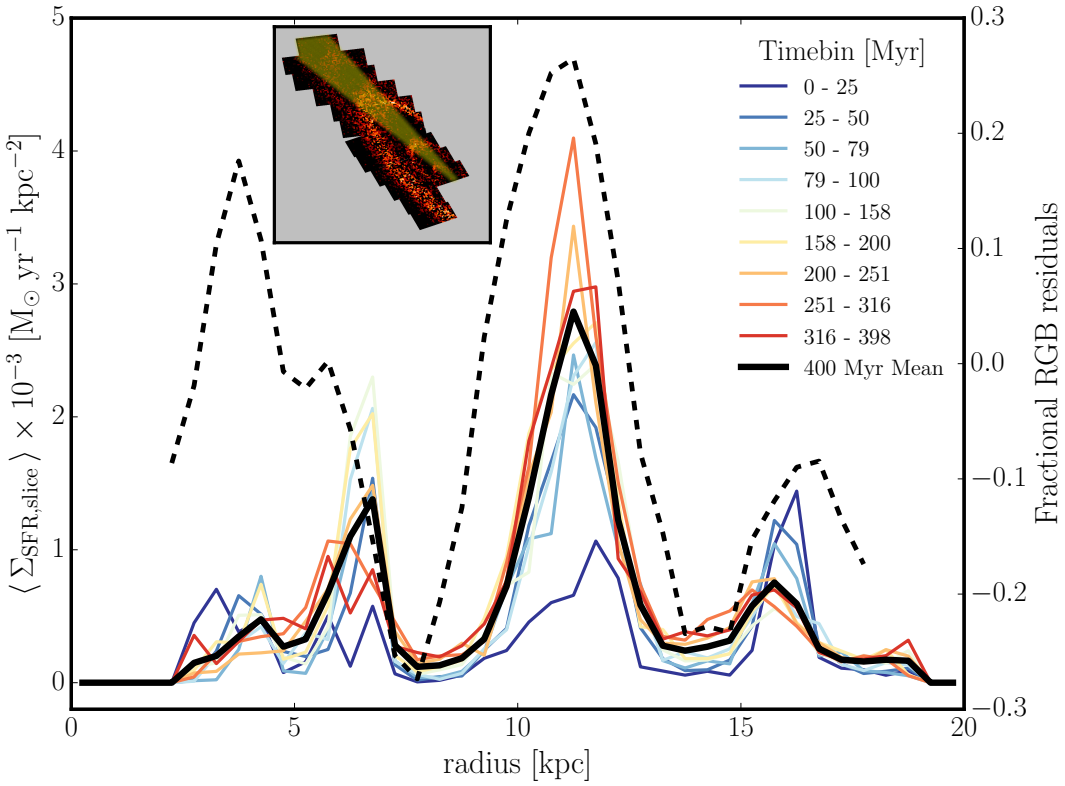

Figure 2.6 SFR surface density as a function of radius and time. Here we plot the SFR surface density in all regions within a 40 degree arc about the major axis (shaded yellow in the inset) per time bin. We have binned the radius in 0.5 kpc bins. The SFR surface density in each radius bin is the mean of all regions that fall within that bin. The thick black line shows the overall mean. The dashed line shows the fractional RGB residuals (Seth et al., in prep.) with values given on the right axis.

our SFHs, which shows excellent morphological agreement with the most recent time bins. This agreement strengthens confidence in our SFH maps given that measurements made in ∼9000 completely independent regions reproduce coherent large-scale structure seen in a well-established SFR tracer. The relationship between the SFR and the FUV flux will be examined in an upcoming paper (Simones et al. in prep.).

The SFHs reveal large-scale, long-lasting, coherent structures in the M31 disk. There are

three star-forming ring-like features; a modest inner ring at ∼5 kpc, the well-known 10-kpc ring, and an outer, low-intensity ring at ∼15 kpc that partially merges with the 10-kpc ring due to a combination of projection effects and a possible warp that is visible in HI (e.g., Brinks & Shane 1984; Chemin et al. 2009; Corbelli et al. 2010). These rings have been observed previously in *Spitzer*/Infrared Array Camera (IRAC) images (Barmby et al. 2006) and *Spitzer*/Multiband Imaging Photometer (MIPS) images (Gordon et al. 2006), as well as in atomic (Brinks & Shane 1984) and molecular gas images (Nieten et al. 2006). There is also an observed over-density of red giant branch (RGB) stars in the 10-kpc ring (Dalcanton et al. 2012). Recovery of these coherent, well-known features is further confirmation that our method is robust.

One of the most remarkable features of this SFH is that the 10-kpc ring is visible and actively forming stars throughout the past ∼500 Myr. Although SF occurs at a low level in the outer regions at all times, SF in the ring feature at 15 kpc is most concentrated starting at 80 Myr ago. This is likely due to SF in OB 102, which has had an elevated SFR compared to its surroundings over the last ∼100 Myr (Williams 2003a). The inner ring feature at ∼5 kpc is also visible, and though there appears to be SF in that ring distinct from the surrounding populations, that feature gains definition 200 Myr ago but has largely dispersed in the last 25 Myr.

We further investigate these trends in Figure 2.6 where we plot the average SFR surface density as a function of radius in each time bin for a subset of the regions along the major axis. We determine the distance to the center of each region and then divide the regions into bins of 0.5 kpc. The three rings at ∼5 kpc, ∼10 kpc, and ∼15 kpc are clearly visible as peaks in $\Sigma_{\rm SFR}$, providing further indication of ongoing (if low) SF in the ring features over 500 Myr. This trend is further supported by evidence of RGB star residuals in the ring features (Seth et al., in prep), as shown by the thick dashed line. There is an over density of RGB stars in the 10-kpc ring and in the inner ring where our oldest time bin shows the highest SF. The plot reveals that not only is the 10-kpc ring long-lived, it has also remained mostly stationary in galactocentric radius over 500 Myr, a result that has implications for

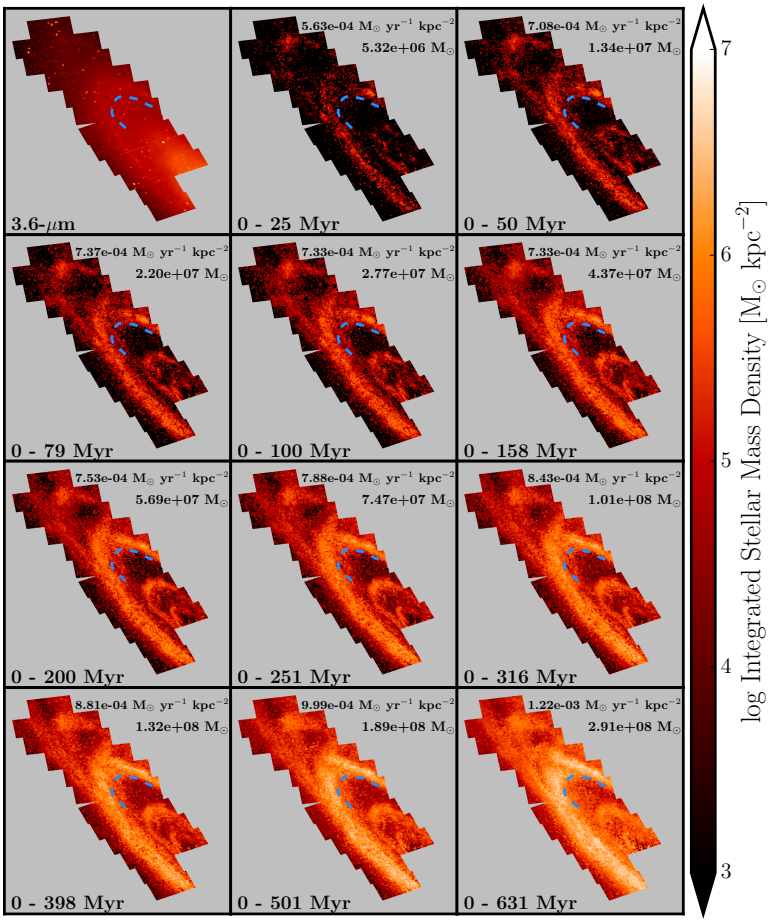

Figure 2.7 Map of the cumulative mass formed. Each region is colored according to the mass formed in that region, integrated from the present day, and scaled by the area of the region. The time range covered is shown in the lower left of each plot. In the upper right of each plot, we indicate the SFR surface density and the total mass formed over that time range. We have chosen to present the maps in this way in order to better highlight the structure of the most recent mass formed. Most of the mass in M31 was in place by at least 1 Gyr ago. We scale the maps to the mass formed in the last 630 Myr in order to highlight structure. The maps are oriented as in Figure 2.1. *Note*: We have included the time bins from 400 Myr to 600 Myr for illustrative purposes only. As discussed in Section 2.3.5, the SFHs in these time bins are much less certain in the crowded inner regions and in the dusty ring than they are in the outer parts of the disk.

the origin of the ring, which we discuss further in Section 2.5.4.

2.4.2 Mass Maps

In Figure 2.7, we show the evolution of recent mass growth in the galaxy from 630 Myr to the present. The upper left panel shows the 3.6 μm image, which is a rough estimation of the total mass of a galaxy, smoothed to the same spatial resolution as our SFHs. The next 11 panels show the total mass formed over a given time range (the same as those in Figure 2.5). The upper middle panel shows the mass that formed in the last 25 Myr while the bottom right panel shows all of the mass formed in the last 630 Myr. The time range is written in the lower left of each plot. In the upper right, we have indicated the total mass formed and the average SFR over that time range.

Most of the SF in M31 occurred much earlier than the timescale probed by these SFHs; consequently, the amount of mass accumulated over the last $\sim$500 Myr has been minimal. As can be seen in the upper left image in Figure 2.7, the older stars are distributed fairly uniformly. This means that the structure that we see in our integrated mass maps only appears within the last $\sim$2 Gyr (more recent than the ages of stars that dominate the emission at 3.6 μm). Over the time range of our SFHs, SF has been confined primarily to the rings.

We further examine the impact of SF in the last $\sim$500 Myr by looking at the fraction of mass formed during this time. In Figure 2.8, we plot the fraction of mass formed in the last 400 Myr to the total mass in each region. We derive the total stellar mass by multiplying the 3.6 μm image (Barmby et al. 2006) by a constant mass-to-light ratio of 0.6 (Meidt et al. 2014). Only $\sim$0.8% of the total stellar mass of this section of the galaxy formed in the last 400 Myr, which is $\sim$3% of a Hubble time. On a region-by-region basis, the mass fraction reaches a maximum of $\sim$7% and is highest in the ring features, specifically in the two outer features, where most of the gas is located (see Figure 2.9). Consequently, though the SFR in the ring in the last $\sim$500 Myr is much higher than that in the rest of the galaxy, it must still be very small relative to past SFRs.

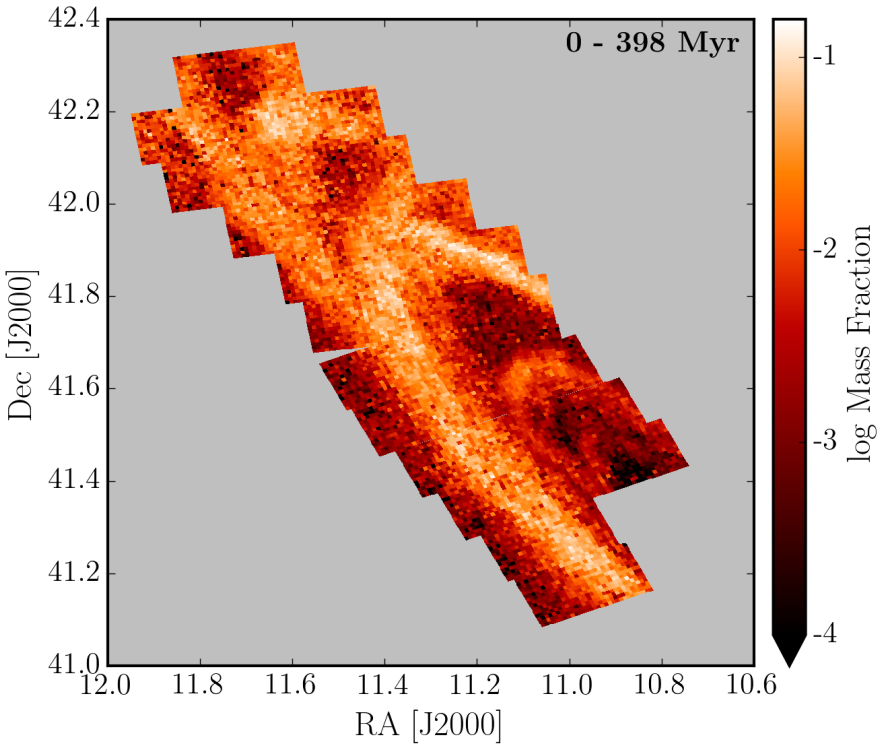

Figure 2.8 Map of the fraction of mass formed in the last 400 Myr compared to the total mass as inferred from the 3.6 μm image (Barmby et al. 2006). The amount of mass formed over the time range covered by these SFHs is very small, as expected, with the highest fractions coming in the 10 and 15-kpc ring features. The map is oriented as in Figure 2.1.

2.5 Discussion

We have presented maps of SF and mass evolution in M31 that show rich structure with ongoing SF and evolution. Much of this structure has been observed in maps of M31 in other tracers. As an example, in Figure 2.9, we plot our SFR map averaged over the last 100 Myr, next to maps of FUV flux (Gil de Paz et al. 2007) and HI (Brinks & Shane 1984). All three maps show M31's ring structures. In addition, we note the good agreement between the 100 Myr SFR map and the map of FUV flux, which is sensitive to SF within the last 100 Myr. These regions of high SFR and flux are also broadly consistent with areas of largest

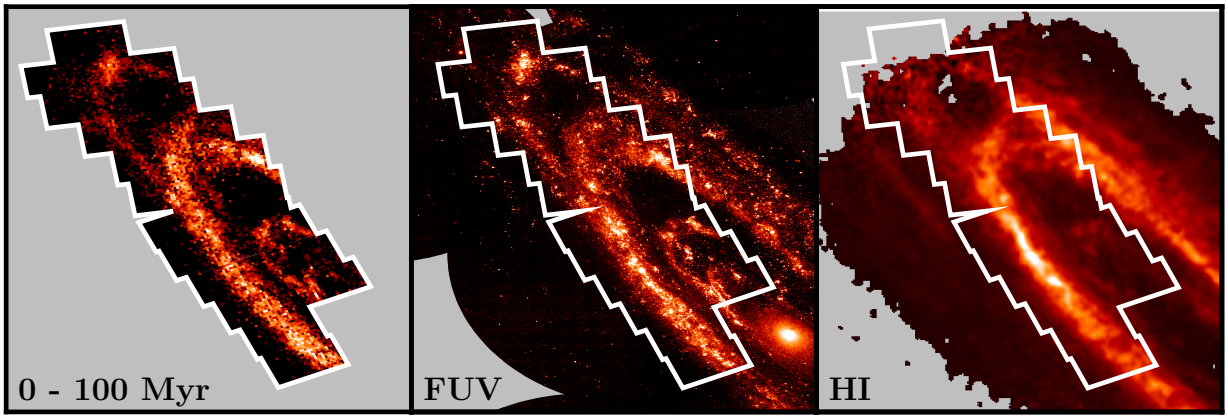

Figure 2.9 Maps of the average SFR in the last 100 Myr as derived in this paper, *GALEX* FUV (Gil de Paz et al. 2007, 4.3″ resolution), and HI (Brinks & Shane 1984, 45″ resolution). There is good morphological agreement between the SFR map and the FUV map, which is sensitive to the same time scale. It is also clear that the regions of highest SF, primarily in the 10-kpc ring, coincide with the regions of highest HI content. Orientation of the images is as in Figure 2.1.

gas content. We now discuss some of the features observed in these maps.

2.5.1 The Recent PHAT SFH

The SFHs of the individual regions are extremely diverse. Some of the regions, such as those in the 10-kpc ring have SF that is ongoing and seemingly long-lived; others, such as those that fall in the outer parts of the galaxy, have generally quiescent SFHs in the past 500 Myr. At the native time resolution of 0.1 dex, the uncertainties on the individual SFHs in each region are significant. By combining all the SFHs, we can reduce the amplitude of the uncertainties in those time bins and obtain a more significant and constrained result for the total SFH.

We derive the total SFH within the PHAT footprint by integrating over all regions in Figure 2.5. In Figure 2.10 we show the total SFR per time bin over the survey area. Figure

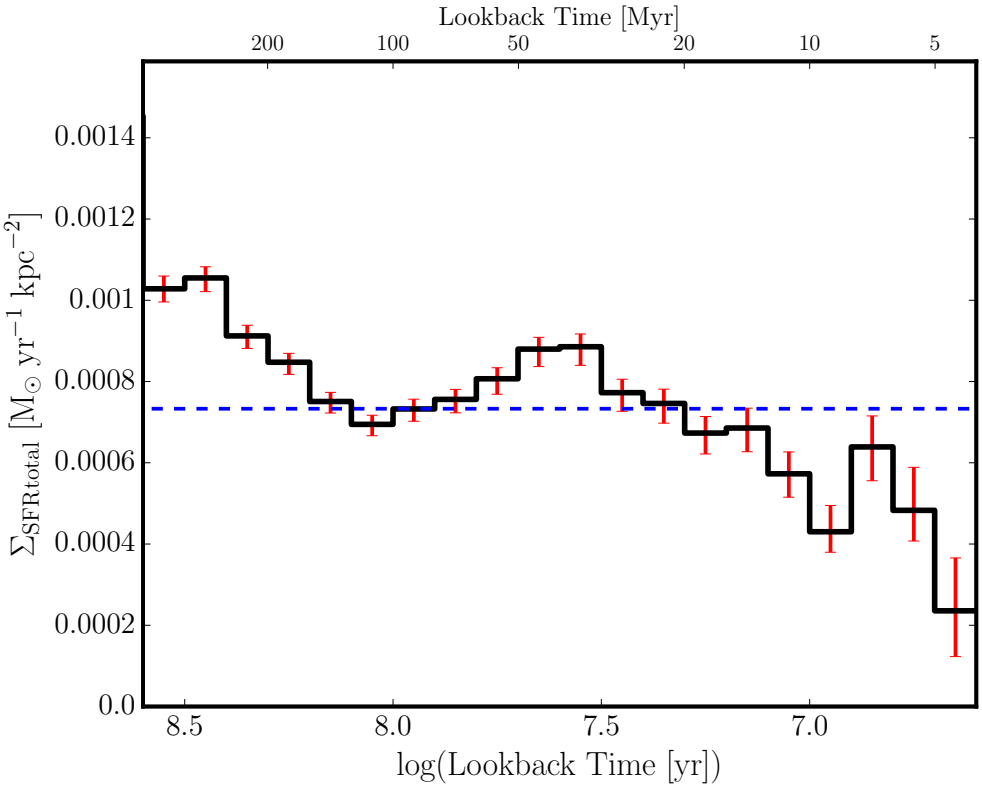

Figure 2.10 The total SFH of M31 within the PHAT footprint over the last 400 Myr, combining the individual SFHs of each field. The dashed line (blue) shows the average SFR density over the most recent 100 Myr. The red error bars are a combination of the random uncertainties and the uncertainties in A_V and dA_V. The time bins are $\Delta(\log t) = 0.1$, so the youngest bins cover considerably less linear time than do the older bins.

2.11 shows the same SFH but with linear time bins over 3 different time ranges. The dashed blue line indicates the average SFR over the past 100 Myr. The uncertainties in each of these figures include the random component as well as uncertainties in the A_V, dA_V combination of the best-fit SFH of each region. There are also systematic uncertainties due to isochrone mismatch (see Section 2.3.3), which we do not include but are $\sim$30% in all time bins. The SFRs and uncertainties in each time bin are listed in Table 2.2.

We look more closely at the total SFH to determine which regions contribute in each time

Table 2.2. Total PHAT SFH

log(ti) log(yr)	log(tf) log(yr)	SFR $M_\odot\ yr^{-1}$
6.60	6.70	$0.09^{+0.04}_{-0.03}$
6.70	6.80	$0.18^{+0.03}_{-0.02}$
6.80	6.90	$0.24^{+0.02}_{-0.02}$
6.90	7.00	$0.16^{+0.02}_{-0.01}$
7.00	7.10	$0.22^{+0.02}_{-0.02}$
7.10	7.20	$0.26^{+0.01}_{-0.02}$
7.20	7.30	$0.25^{+0.01}_{-0.01}$
7.30	7.40	$0.28^{+0.01}_{-0.01}$
7.40	7.50	$0.29^{+0.01}_{-0.01}$
7.50	7.60	$0.34^{+0.01}_{-0.01}$
7.60	7.70	$0.33^{+0.01}_{-0.01}$
7.70	7.80	$0.30^{+0.01}_{-0.01}$
7.80	7.90	$0.29^{+0.01}_{-0.01}$
7.90	8.00	$0.28^{+0.01}_{-0.01}$
8.00	8.10	$0.26^{+0.01}_{-0.01}$
8.10	8.20	$0.28^{+0.01}_{-0.01}$
8.20	8.30	$0.32^{+0.01}_{-0.01}$
8.30	8.40	$0.34^{+0.01}_{-0.01}$
8.40	8.50	$0.40^{+0.01}_{-0.01}$
8.50	8.60	$0.39^{+0.01}_{-0.01}$

Note. — The total SFH summed over all regions. The first column lists the start of each timebin and the second column lists the end of each time bin. The third column shows the total SFR in each time bin, integrated over the entire survey. To convert to SFR surface density ($\Sigma_{\rm SFR}$), divide the SFR by the total area of the survey, 378 kpc^2. The uncertainties represent the smallest range that contains 68% of the probability distribution calculated from the random and dust uncertainties. The first time bin extends to the present day.

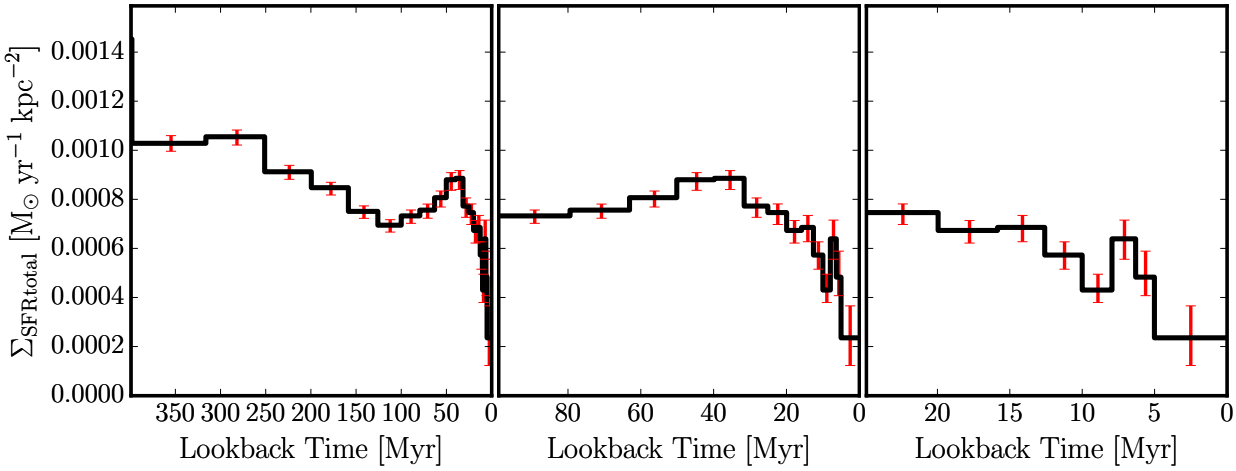

Figure 2.11 Same as in Figure 2.10 but showing time bins on a linear scale. The first panel shows the SFH back to 400 Myr. The second shows the SFH over the last 100 Myr and the third panel shows the SFH within the last 25 Myr.

bin. While the SFR has been generally declining over the last 600 Myr, we see a bump at ∼50 Myr. Further examination reveals that this peak is not a galaxy-wide feature. To show this, in Figure 2.12, we plot the SFH in 5 angular slices in theta about the major axis. We see that the slice that falls down the major axis (green line) shows a declining SFR over all periods of time, i.e., there is no 50 Myr bump. The west-most slice (blue line) shows a slight peak at 50 Myr and if we move to the slice that is out along the minor axis (purple line), the SFR shows the most prominent 50 Myr bump. These slices contain bright OB associations and are dominated by ring regions. Consequently, it is likely that the 50 Myr peak in the total SFH is due to specific star-forming regions in the rings.

In Figure 2.10, we have over-plotted a dashed line showing the average SFR over the past 100 Myr. The average SFR in the PHAT area over the past 100 Myr is 0.28±0.03 $M_\odot$ yr^{-1}, where the uncertainty is calculated from the tests of systematic uncertainties. To determine the average SFR over the past 100 Myr over the entire disk, we adopt a simple scaling argument. We use both the FUV and 24-μm maps of M31 and select the D25 ellipse (Gil de

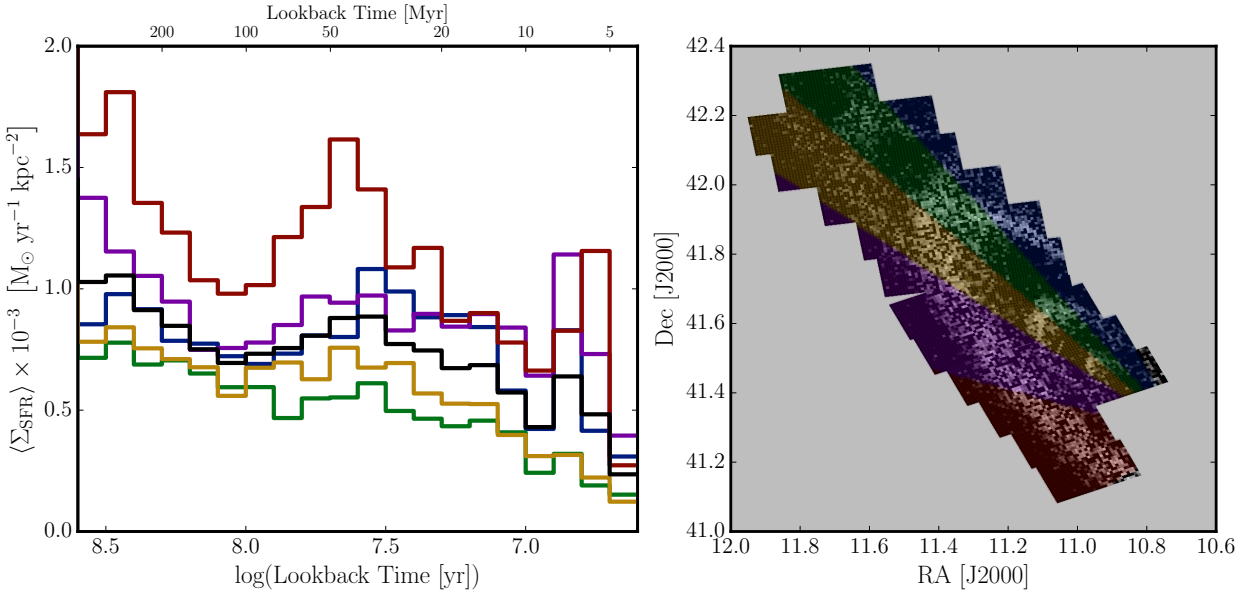

Figure 2.12 SFH in slices about the major axis. On the left we show the average SFR per area in each time bin for all of M31 divided into 5 angular slices. The lines are colored according to angular slice. The same coloring is used in the right panel to indicate the angular slice that is represented. All slices cover 30 degrees, though they do not all contain the same number of regions. The black line shows the average SFR per time bin for the entire survey area.

Paz et al. 2007) as an aperture. We then measure the total flux within the entire aperture and the flux inside the PHAT footprint (without Bricks 1 or 3). In both cases, the fraction of the total flux inside the PHAT footprint is ∼40%. Therefore, to scale the PHAT SFR to the entire D25 aperture, we must multiply by a factor of 1/0.4 = 2.5. We multiply the SFR by this scaling factor to yield a total SFR of ∼0.7 $M_\odot$ yr^{-1}. Previous studies have examined the global SFR using resolved stars (∼1 $M_\odot$ yr^{-1}; Williams 2003b), 8 μm (0.4 $M_\odot$ yr^{-1}; Barmby et al. 2006), FUV (0.6–0.7 $M_\odot$ yr^{-1}; Kang et al. 2009), Hα (∼0.3 $M_\odot$ yr^{-1};Tabatabaei & Berkhuijsen 2010, 0.44 $M_\odot$ yr^{-1}; Azimlu et al. 2011), and FUV + 24 μm (0.25 $M_\odot$ yr^{-1}; Ford et al. 2013). Our result falls within this range, and is most consistent with methods

that effectively average over longer timescales.

Although this simple scaling argument neglects possible variations in the SFR from one side of the disk to the other, we do not expect these variations to be large enough to dramatically affect the overall SFR. A complete analysis of the SFR measured via different tracers is beyond the scope of this paper but will be examined more closely in an upcoming paper (Lewis et al., in prep).

2.5.2 Birthrate Parameter

We further examine the total SFH by computing the birthrate parameter, b, which is defined as the ratio of the current SFR to the past averaged SFR:

$$b = \frac{\mathrm{SFR}}{\langle \mathrm{SFR} \rangle} \tag{2.1}$$

We calculated the past-averaged SFR by converting the 3.6 μm image to mass, as described in Section 2.4.2 and setting the lifetime of the disk to the Hubble time.

While the birthrate parameter is generally used to classify a galaxy as a whole as in either a star-bursting or quiescent phase, in this case we can examine b for our individual regions. This gives us the ability to tell whether regions of current high SF, such as the 10-kpc ring, are currently undergoing unusually high SF relative to the rest of the galaxy (in which case b should be large) or whether those regions have always had higher SFRs (in which case $b \leq 1$). In Figure 2.13, we show a map of the birthrate parameter over two timescales: the lifetime of our SFHs ($\sim$400 Myr) and 100 Myr. The regions are colored according to b on a linear scale. We see over both time periods that the rings at 10 and 15 kpc have higher values of b than the rest of the galaxy. While b is greater than unity over most of these ring features, there are very few regions where it rises above 2, which indicates that while SF is certainly elevated in those regions compared to the overall SFR, it would not be considered 'bursty'. The exception in the right panel of Figure 2.13 is the large OB associations in Bricks 15 and 21 where we know that SF is occurring at an elevated rate. These low values

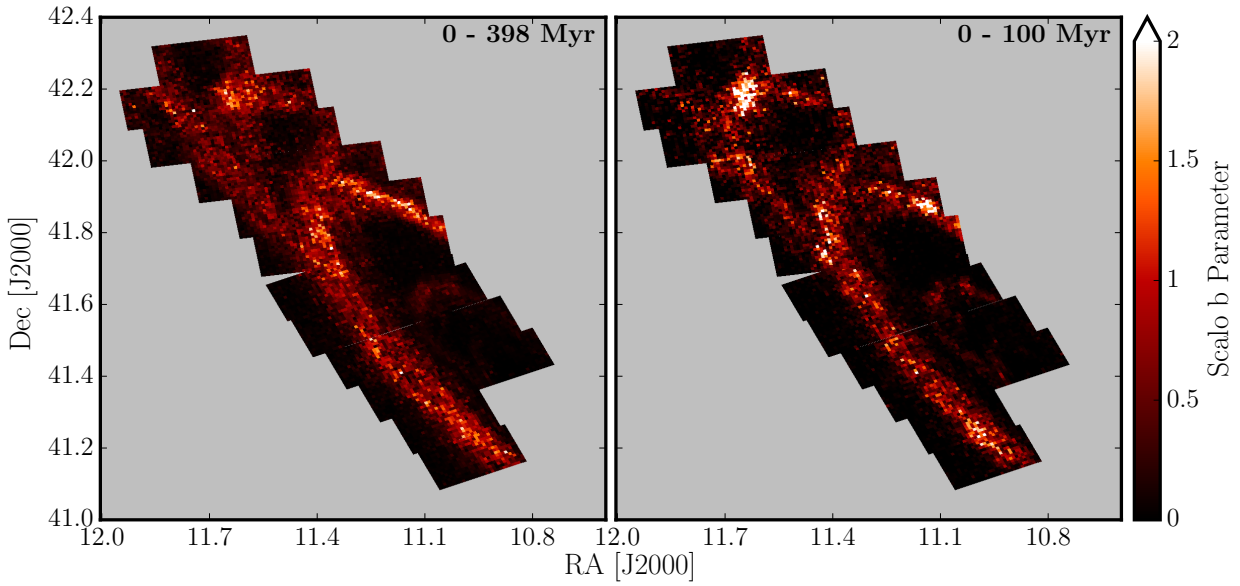

Figure 2.13 Maps of the birthrate parameter b over 400 Myr and 100 Myr timescales. The regions are colored according to the value of the birthrate parameter in that region and an upper limit has been set at $b = 2$. The maps are oriented as in Figure 2.1. Both maps show $b > 1$ in the 10 and 15-kpc rings. The OB associations in Bricks 15 and 21 are clearly visible in the right image as regions of elevated b.

of b are not wholly unexpected since the 3.6 μm image is quite smooth (see the upper left panel in Figure 2.7) though one can still make out the ring feature.

Integrated over the entire survey area, we find that the birthrate parameter is 0.23 over the last 100 Myr and 0.27 over the last 400 Myr. This further shows that M31 has been forming stars in the last 400 Myr at a much lower rate than it was in the past.

2.5.3 Comparison with Previous Work

Here we examine the results presented in this paper in relation to earlier studies of the recent SFH of M31.

Williams (2002) measured the SFH using archival *HST* data in various fields throughout the galaxy, some of which overlap with the PHAT survey area. He also recovered a SFH using CMD analysis, with an earlier version of the code used in this work. The overlapping fields in his study fall primarily along the 10-kpc ring, so they probe regions of higher SFR. His 'INNER' field, which falls in B13, shows a SFH with a steep decline from 1 Gyr to ∼200 Myr ago, then a short rise to a peak in a time bin covering the range 40-80 Myr ago, and a decrease to the present day. Two nearby fields, G287 and G11, show a similar morphology in their SFHs, though the peak comes at slightly earlier times, closer to 100 Myr. Other fields fall along the northeast section of the 10-kpc ring and show strong SF at the most recent times. Our SFHs are consistent with this. As we showed in Figure 2.12, the average SFR per time bin can vary significantly in different regions. If we were to define our regions differently, such that they fell only on the regions of strongest SF, we would also see a sharper rise to the present day.

Williams (2003b) measured the SFH of M31 using ground-based data (Massey et al. 2006) and found an increase in the SFR from ∼25 Myr ago to the present. This increase was seen primarily in the northeast spiral arm. While the work we present here shows a decrease in the SFR from ∼50 Myr to the present, our last time bin in Figure 2.5 from 25 Myr to the present shows a tightening of the ring structure and more localized SF along the northeast arm, suggesting that the difference in resolution between this study and that of Williams (2003b) could be the cause of the discrepancy. For example, blends could be measured as upper MS stars, artificially increasing the measurements in the youngest time bins from ground-based data.

Davidge et al. (2012) examined the recent SFH of the entire disk of M31 by comparing u' luminosity functions with those derived from models assuming various SFHs. Their result indicates a factor of 2-3 rise in the SFR during the past 10 Myr, which is in broad agreement with the results of Williams (2003b).

While our results do not show a recent SFR increase, we will point out that Williams (2003b) and Davidge et al. (2012) looked at the SFH over the entire disk of M31, while we

focus only on ∼1/3 of the disk. There is evidence that the SFR is elevated in the outer regions of the southern and western parts of the disk more so than in the eastern parts. Our study does not include the southern disk, nor does it reach the outer regions of the western edge of the disk. It is possible that these regions could contribute to an increase in the last 10 – 25 Myr that we do not see in this work.

Williams (2003b) also saw movement of SF across the disk, which he interpreted as evidence of propagating density waves from the northern to the southern disk. We do not see this movement. However, our survey does not cover the southern disk and our region sizes are much smaller, giving us the ability to more precisely locate SF. We find no evidence for propagation in the area covered by the PHAT survey. We do, however, agree that SF has been confined primarily to the ring structures over at least the last 500 Myr.

2.5.4 The Mystery of the 10-kpc Ring

The Ring is Long Lived

The results we present here indicate that the ring of SF at a radius of 10 kpc has persisted for at least 500 Myr. If we assume a rotational velocity of M31 at the 10-kpc ring of ∼250 km s^{-1} (Chemin et al. 2009; Corbelli et al. 2010), then the dynamical time of M31 at the ring is ∼250 Myr. We have defined the dynamical time as the time to make one full rotation at a given radius: $t_{\rm dyn} = 2\pi\, r/v_r$. This means that SF has continued in the ring for at least two dynamical times. Williams (2003b) found that SF has occurred in the ring for the last 250 Myr, and Davidge et al. (2012) found SF in the ring for at least 100 Myr. Dalcanton et al. (2012) showed that there is an over density of stars with ages >1 Gyr in the ring as well, further supporting the long-lived nature of this feature.

Looking at just the regions that fall inside the 10-kpc ring, we see that over the last 600 Myr, SF in the ring drives the overall SFR (see Figure 2.14). Within the last 400 Myr, the SFR in all regions that do not lie in the ring has been mostly constant, while the SFR inside

the ring has varied substantially. This is also clearly visible in Figure 2.5, where the ring is very prominent due to a lack of SF occurring in other parts of the galaxy. We find that in the last 400 Myr, ∼60% of all SF occurs in the 10-kpc ring feature.

The long-lived nature of the ring is also visible in Figure 2.6, where SF is elevated relative to the areas just outside of the ring at all time. Only in the most recent 25 Myr do we see a notable decrease in SFR in the 10-kpc ring. This plot only includes regions that fall along the major axis so as to minimize uncertainties in the deprojected distance to each region. As a result, this slice does not include many of the higher SFR OB associations, such as OB 54 and those that fall along the northeast portion of the 10-kpc ring. These would likely act to increase the SFR over the most recent ∼50 Myr.

Not only is the ring long-lived, but it has also been mostly stationary. From Figure 2.6, we can see that the 10-kpc ring has remained centered at about the same location, moving no more than 0.5 kpc over ∼500 Myr. This translates into a motion of ∼1 km/s.

Dispersion of the Ring

Our maps of SF show that the 10-kpc ring is clearly broader at older ages than at younger ages. This suggests two possibilities: 1) Over time, SF in the ring has grown more concentrated, occurring in a much narrower strip, likely following the density of gas within the ring features or 2) SF has always occurred in the center of the ring and we see a broadening of the ring as the stars disperse. The second option is more probable, since we know qualitatively that the majority of stars form in clusters and that those clusters eventually disperse and the individual stars diffuse into the surrounding environment, becoming part of the larger galactic background (e.g., Harris & Zaritsky 1999; Bastian et al. 2009).

The simple kinematical argument is that if stars are born with an average random velocity of 10 km s^{-1} and that motion is directed radially outward, then over the course of 100 Myr, those stars should move 1 kpc. For the results we present here, this would result in significant motion over the course of 500 Myr (5 kpc). It would also suggest a strong dispersion of the ring features over relatively short periods of time, which we do not see. In reality, these

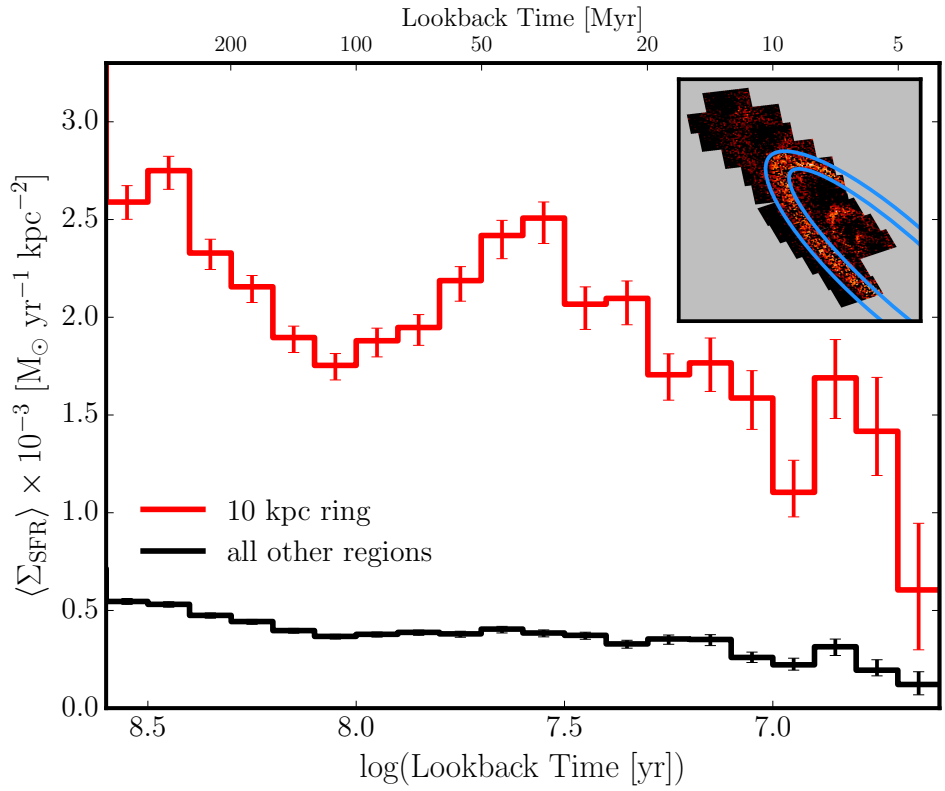

Figure 2.14 SFH showing the average SFR in each time bin for all regions within the 10-kpc ring (red) and all other regions (black). Error bars include random uncertainties primarily due to the number of stars on the CMD as well as uncertainties as a result of the search in A_V and dA_V for the best-fit SFH. Comparison with Figure 2.10 shows that the total SFH is driven by SF within the ring. SF outside of the ring feature was more important before ∼500 Myr ago. It is important to note that due to the high inclination of M31, our definition of the 10-kpc ring, shown in the inset, may also include some of the 15-kpc ring (if it is indeed a distinct feature). Nevertheless, this still confirms our result that SF occurs primarily in these ring features.

timescales are much longer. Bastian et al. (2011) showed that the evolution of the spatial structure of stellar populations in nearby dwarf galaxies occurs on many different timescales, setting *lower* limits of tens to hundreds of Myr, longer than would be expected based on simple arguments.

A detailed quantitative discussion of the evolution of spatial structure will be the subject of a future paper.

What is the Origin of the Ring?

The 10-kpc ring is the most prominent feature of M31, visible in wave bands from the UV through the radio (e.g., Brinks & Shane 1984; Barmby et al. 2006; Beaton et al. 2007; Block et al. 2006; Gordon et al. 2006; Massey et al. 2006; Nieten et al. 2006; Gil de Paz et al. 2007; Braun et al. 2009; Chemin et al. 2009; Fritz et al. 2012). Its ubiquity naturally leads to the question of its origin. Surprisingly, there have been few studies devoted to this question; its genesis remains largely uncertain.

Those studies that have attempted to answer the question have invoked one of two likely formation scenarios for a ring: (1) resonance ring due to a central bar, or (2) collisional ring due to the passage of a satellite galaxy through the disk of M31.

Bars can produce inner, outer, and/or nuclear rings in galaxies (Buta 1986). M31 shows evidence of a bar, as suggested by its boxy bulge seen in infrared imaging (Beaton et al. 2007), though it is likely not very strong (Athanassoula & Beaton 2006). The bar length has been estimated to be 4 – 5 kpc (Athanassoula & Beaton 2006; Beaton et al. 2007). If the 10-kpc ring is due to a bar, it is unlikely to be either a nuclear ring, which generally occurs within the bar (e.g., Buta & Combes 1996) or an inner ring, originating at the end of the bar (Schwarz 1984). Instead, if the ring is indeed due to a rotating bar, it must be an outer ring, which occurs near the outer Lindblad resonance (OLR, e.g., Schwarz 1981; Buta 1995). It has also been shown that in barred galaxies with rings, the ratio of the outer ring diameter to the bar diameter is $\sim$2 (Kormendy 1979; Athanassoula et al. 2009). By comparing observational data of M31 with N-body simulations, Athanassoula & Beaton

(2006) find that the OLR is at 45 ± 4 arcmin (9 – 10 kpc at the distance of M31). The outer ring radius to bar length ratio and the location of the OLR in M31 suggest that the 10-kpc ring could indeed be due to a bar.

Rings in galaxies can also be the result of collisions with satellite galaxies (e.g., Lynds & Toomre 1976). In the case of M31, that satellite galaxy is likely M32. A handful of studies have attempted to model the effect of M32 crashing through the disk of M31 (Gordon et al. 2006; Block et al. 2006; Dierickx et al. 2014) and have found that such a collision could produce a ring with properties similar to that observed, including ring centers offset from the center of the galaxy, and the hole seen in the 10-kpc ring. These studies suggest that the impact event happened 20, 210, and 800 Myr ago, respectively.

There are inconsistencies with both scenarios. It is much more statistically likely that M31 is a barred galaxy with resonance rings simply because there are many barred galaxies that show this kind of ring structure. However, the offset centers of the 5 and 10-kpc rings (Block et al. 2006) and the hole in the 10-kpc ring are difficult to explain if the rings are all due to a bar. On the other hand, the collisional simulations suffer from uncertainties in the mass and orbit of M32, both of which strongly affect the collision and resulting morphological features. In addition, if a collision occurred, we would expect to see evidence of ring expansion. We note, however, that it is possible that existing spiral structure and bar disturbances could interact strongly with these much weaker collisional rings generated by a companion, preventing the expected classical propagation (Struck 2010).

Our results indicate that the ring has been a distinct feature, actively forming stars for at least 500 Myr. Davidge et al. (2012) found that the last major disturbance to the disk occurred at least 500 Myr ago. Bernard et al. (2015b) and Williams et al. (2015) both find the last major event in M31's history to be 2 – 3 Gyr ago. These are longer than the timescales suggested by Gordon et al. (2006) and Block et al. (2006) for a collision with M32. We cannot rule out a collision that happened 800 Myr ago (Dierickx et al. 2014) much less 2 – 3 Gyr ago. However, the velocity deviations suggested by collisional ring models do not match the observations presented here. Block et al. (2006) expect the rings to expand

radially at $\sim$7 – 10 km s^{-1} and Dierickx et al. (2014) find radial motions of at least 20 km s^{-1} in their models. The systems described by Struck (2010) have radial motions of at least 10 – 20 km s^{-1}, though he does note that M31 seems to be an exception to the general class of colliding ring galaxies.

Consequently, based on existing models of the origin of M31's ring features, we can rule out a purely collisional origin because of the additional time-resolved data we present in this paper. A bar-induced ring is more likely to be long-lived and resonance rings from bars are fairly common. If the ring is a resonance ring, it would make M31 a much more average galaxy than one that had recently suffered a dramatic collision. On the other hand, perhaps the morphological features we see in M31 result from a combination of the two scenarios. We note that no existing studies attempt to explain the existence of the outer ring at 15 kpc.

If we wish to fully understand the origin of the 10-kpc ring (or either of the other ring features) in M31, it is clear that more work is needed. One necessary step is to run simulations that follow the creation of the ring and its evolution over 1 Gyr or more. These simulations should account for multiple possible formation scenarios: collision with a satellite, resonance due to a bar, and a combination of the two. Athanassoula & Beaton (2006) provide stellar velocity field predictions that need to be tested. Finally, obtaining deep photometry that goes below the oldest main sequence turnoff over a large area around the ring in combination with a more complex dust model would allow us to determine the SFH in M31 back to more than 5 Gyr ago, providing additional observational constraints on the lifetime of the ring.

2.6 Conclusions

We have measured the SFH of $\sim$1/3 of the star-forming disk of M31 from *HST* images as part of the PHAT survey. We divided the survey area into $\sim$9000 approximately equal-sized regions and determined the SFH, as well as the extinction distribution, independently in each region.

We have found that SF in M31 has been largely confined to three ring features, including the well-known 10-kpc ring, over the past $\sim$500 Myr. The 15-kpc ring becomes most promi-

nent and structured starting at about 80 Myr ago, with SF increasing to the present day. In the 5-kpc ring, SF reached a peak about 100 Myr ago and the ring feature has since begun to dissolve.

The 10-kpc ring is long-lived and stationary, producing stars over at least the past 400 Myr, which is about two dynamical times at that radius. Over this period of time, SF has been elevated relative to the surrounding regions. As a result, the ring drives the overall SFH. The shape of the total SFH follows that of the SFH of just regions that fall broadly in the 10-kpc ring feature. This feature has also shown little or no significant propagation in our survey area over the lifetime of these SFHs.

We have shown that the total mass formed over the last 400 Myr is less than 10% of the total mass of the galaxy, as measured from 3.6 μm images. M31 is a fairly quiescent galaxy today. Aside from a handful of bright regions that coincide with OB associations, the total SFR at the present day is very low. We have shown with maps of the birthrate parameter, b, that only a handful of regions have $b > 2$ over the last 100 Myr or 400 Myr. In most cases, the current average SFR is very low relative to the past average. Globally, the galaxy has $b = 0.23$ over the last 100 Myr and $b = 0.27$ over the last 400 Myr, further confirming that M31 is a fairly quiescent galaxy today.

Finally, aside from a possible increase in SF $\sim$50 Myr ago, the SFH over the last 400 Myr has been relatively constant. We have computed the average SFR over the past 100 Myr to be 0.28 ± 0.03 $M_\odot\,yr^{-1}$ within the PHAT footprint. Extrapolating to the entire galaxy we find a global SFR over the last 100 Myr of 0.7 $M_\odot\,yr^{-1}$, which is consistent with the range found in previous studies.

2.7 Supplementary Analysis

2.7.1 Filter Choice

We have chosen to use only the optical filters (F475W and F814W) for this analysis. In the PHAT survey, data were also taken in two NUV filters (F275W and F336W) and two NIR

filters (F110W and F160W). The optical filters provide the greatest leverage for probing the recent SFH because they have by far the deepest CMDs of MS stars which allows us to probe both further down the luminosity function and further back in lookback time.

In principle, addition of the UV filters might potentially allow for greater constraints on the recent SFH; however, in practice, the PHAT data do not allow it. Only the brightest main sequence stars have measurements in the two UV filters, which significantly reduces the age range over which the SFH can be derived. As such, including the UV filters will not improve the analysis presented in this paper.

The NIR data are more complex. They are significantly shallower than the optical data. The mean depth in F160W is an absolute magnitude of ∼0, which is 2 magnitudes shallower than in the optical. At this depth, we lose the main sequence at less than 200 Myr. In addition, there are not very many stars that fall on the main sequence to begin with, further reducing the usefulness of the NIR for analysis of the recent SFH. Finally, the NIR models of young stars are much more uncertain than the optical models, as there has been less verification of the models in this regime.

In Figure 2.15, we plot the color-magnitude diagrams of a bright, highly star-forming region in B15. The left panel shows the optical data and the right panel shows the NIR data. On each panel, we have plotted three sets of isochrones at 25, 100, and 400 Myr at two different metallicities, solar and slightly sub-solar ([M/H] = –0.3). M31 has a very flat metallicity gradient that is approximately solar, so these values are reasonable for the disk. The stars mark the main sequence turnoff points at each age and metallicity. The optical data are deep, and we have leverage back at least 400 Myr. On the other hand, the IR data are much shallower and do not allow reliable SFH measurements beyond ∼200 Myr. Consequently, we have chosen to use just the optical data in this analysis of the recent SFH.

2.7.2 Determining the Best-Fit SFH by Searching A_V, dA_V Space

The two main free parameters in the fitting process are those that describe the dust model: an extinction applied evenly to all stars, A_V, and a differential extinction, dA_V, that is

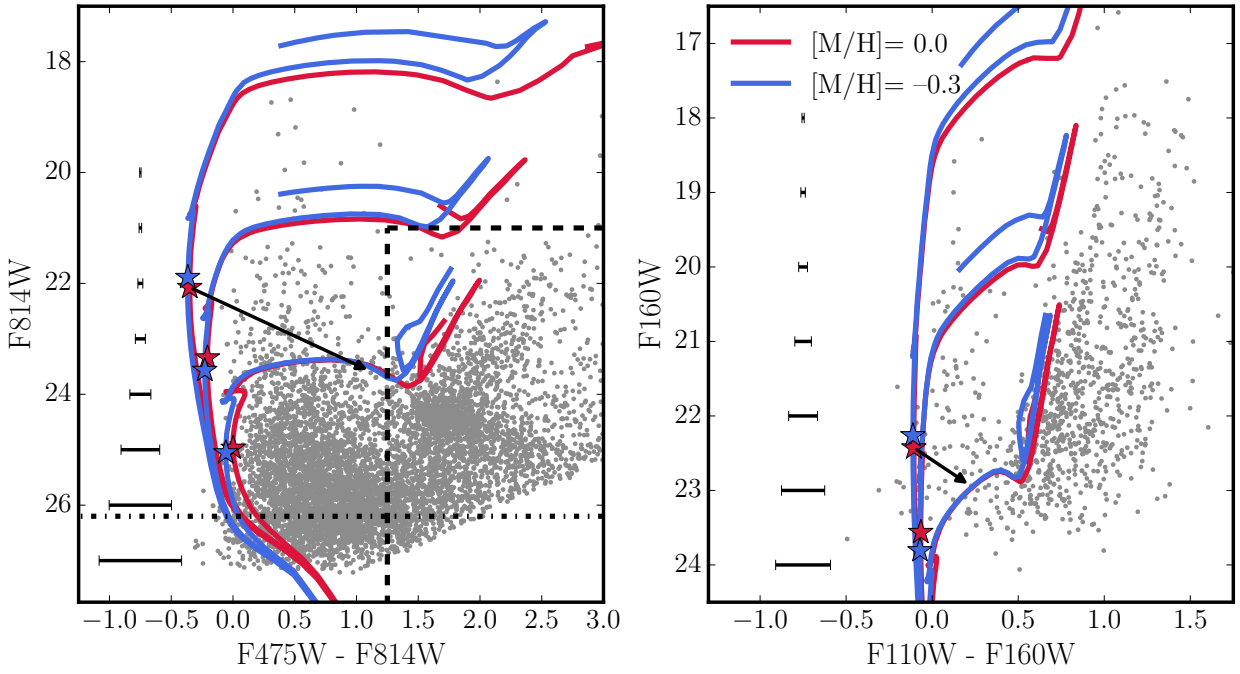

Figure 2.15 The optical (left) and NIR (right) CMDs of a highly star-forming region in B15. On each CMD, we have plotted three sets of isochrones at 25, 100, and 400 Myr and two metallicities: solar ([M/H] = 0.0, red) and sub-solar ([M/H] = –0.3, blue). We also show a reddening vector of 2.5 magnitudes which is the amount of extinction required by the best-fit SFH in this region. In the left panel, we also show the optical exclude region described in this paper (dashed line), the 50% completeness limit (dot-dash line).

applied in addition to A_V. The differential extinction is applied as a distribution to all stars, rather than uniformly, so that each star receives some additional extinction between 0 and dA_V. As a result, the total extinction applied to each star falls in the range $[A_V, A_V + dA_V]$.

Using B15, we sampled A_V, dA_V space on the range A_V = [0.0, 1.0] and dA_V = [0.0, 6.0] with step sizes of 0.25 in both parameters. The results for two of these regions are shown in the top panel of Figure 2.16. We found that while some regions had a well-defined best-fit SFH, other regions showed "troughs" of (A_V, dA_V) pairs going to arbitrarily high dA_V values with fits that were within 1-σ of the best-fit, defined as $fit_{\rm best} + 1$. The resulting

SFHs are indistinguishable within the error bars. These "troughs" are an artifact of the exclusion area we used in the SFH solution, which removed the red clump and RGB from the fitting process. At higher extinction, stars are artificially pushed into the exclude region on the CMD. In order to account for the fewer stars in a given CMD bin, the SFR increases. Examination of the regions with these troughs shows that they tend to start at $A_V + dA_V = 2.5$. As a result, we limit our total extinction to 2.5 magnitudes.

2.7.3 Applying a Dust Prior

In some of the very low-SFR regions at the survey edges and between the ring features, we found that `MATCH` assigned large extinctions with very poor constraints. Given the low SFR and the small number of bright, young MS stars at these locations, there is no physical explanation for large extinction. To investigate this issue, we use the Draine et al. (2014) dust mass maps to examine the relationship between the `MATCH` extinction and the total dust mass in those regions. On the left side of Figure 2.17, we plot the ratio of the `MATCH` total dust ($A_V + dA_V$) to the dust mass surface density as a function of SFR (averaged over the last 100 Myr) and number of MS stars. Each circle represents a single region, color-coded by the number of MS stars in that region, where we define MS stars as those with F475W − F814W < 1 and F475W < 26. The bricks closer to the bulge have lower completeness, so the value of 26 was chosen to accommodate those bricks with 50% completeness just fainter than 26th magnitude. On the right axis, we converted the dust mass surface density into extinction according to Equation 7 in Draine et al. (2014):

$$A_V = 0.74 \left(\frac{\Sigma_{Md}}{10^5 \ M_\odot \ \mathrm{kpc}^{-2}} \right) \mathrm{mag}. \tag{2.2}$$

We have made this conversion for ease of reader interpretation, though analysis of this result is beyond the scope of this paper. For the sake of this exercise, only the relative numbers are important.

If there were a perfect correlation between measured dust mass and the `MATCH` dust parameters, we would expect to see a straight horizontal line in this figure such that the

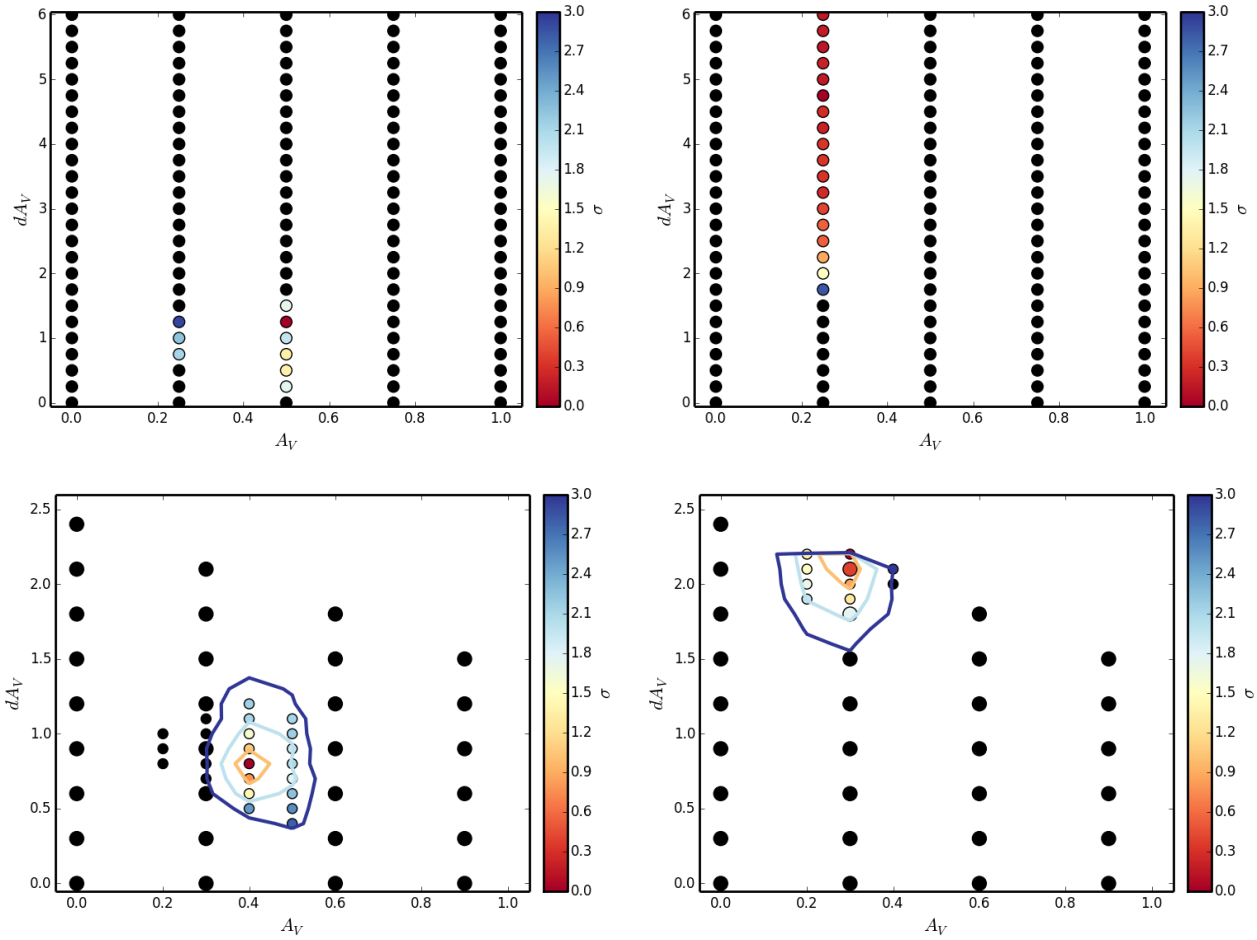

Figure 2.16 Exploration of A_V, dA_V parameter space in two regions of B15. The top panel show examples of a grid search in A_V, dA_V space. One region has a very well defined best fit. In the second region, a "trough" of low fit values occurs. If dA_V is increased, the fit value does not change, but rather remains very close to the best fit. In the bottom panel, we show the results of the search over (A_V, dA_V) space for the same two regions with the requirement that $A_V + dA_V \leq 2.5$. Once again, the region on the left remains well-defined in A_V, dA_V space. In the second region, the constraint on extinction has forced a best fit. The lines show the 1-, 2-, and 3-σ contours.

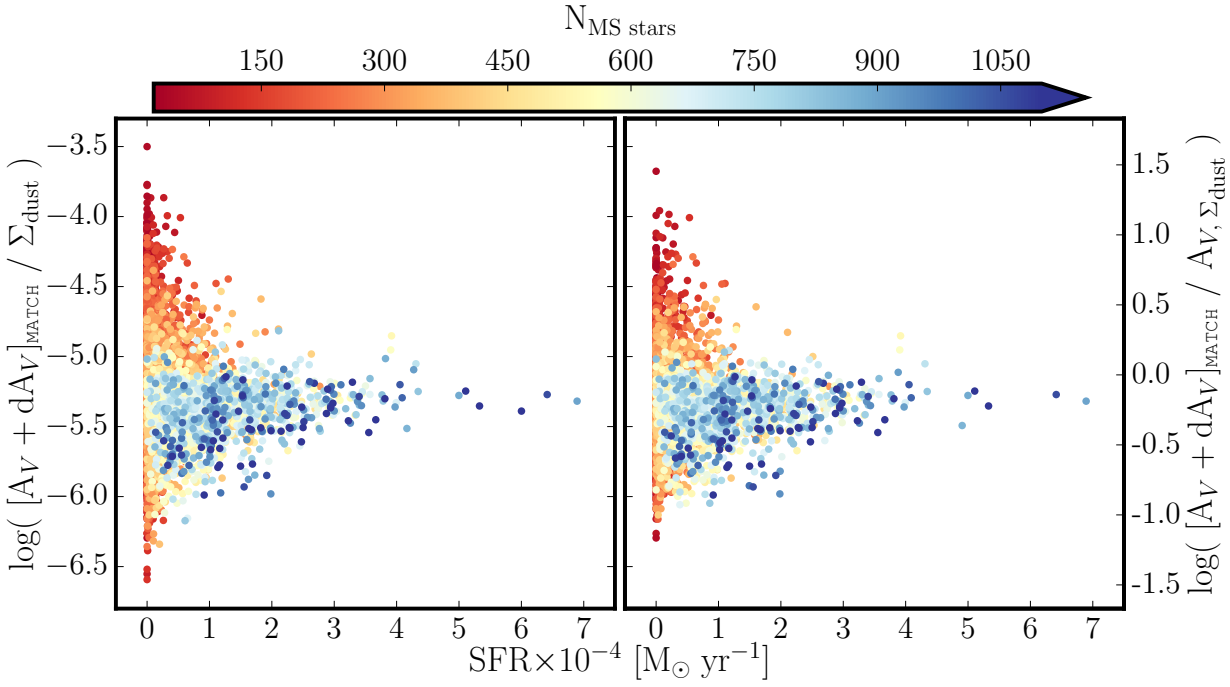

Figure 2.17 Comparison of the `MATCH`-derived dust parameter ($A_V + dA_V$) with the dust mass surface density as derived by Draine et al. (2014) before (left) and after (right) applying the prior. On the left axis, we show the ratio of the `MATCH` extinction to the dust mass surface density. On the right axis we show the ratio of the `MATCH` extinction to the extinction derived from the dust mass surface density following Equation 2.2. The relationship between the two parameters is generally quite constant with an expected increase in scatter at the lowest SFRs.

ratio of the normalized MATCH dust to the normalized dust mass would be constant across all SFRs with some scatter expected at the low SFR end. Instead, we see that at very low SFRs there is wide scatter in this ratio, and, as may be expected, these regions also contain lower numbers of MS stars. If there are very few or no stars on the upper MS, it is more difficult to anchor the SFH. In order to fit the broadened lower MS, the amount of differential reddening is increased. Figure 2.17 shows that the ratio between MATCH dust model parameters and the dust mass is approximately constant in regions with high SFR and/or many MS stars. This implies that we should be able to fit a straight line to a plot of MATCH dust parameters vs. dust mass in these regions with the most robust fits. So we use this relation to set a prior on the total extinction in a region to adjust the low-SFR, high-dust regions to achieve more physical extinction parameters.

We compare the MATCH best-fit extinction ($A_V + dA_V$) with dust mass surface density ($M_{\rm dust}$) in each region. To do this, we fit a line with slope m and scatter σ to a plot of MATCH dust ($A_V + dA_V$) vs. $M_{\rm dust}$ of the n regions with high SFR and many MS stars.

The slope and dispersion of that line are found by solving the following equation numerically for m and σ such that $\chi^2 = 1$:

$$\chi^2 = \frac{1}{n-1}\sum_n \begin{cases} \dfrac{\left([A_V + dA_V] - m \times M_{\rm dust}\right)^2}{(\overline{\sigma_{A_V\,\rm reg}}^2 + \sigma^2)}, & A_V + dA_V < 2 \\ \displaystyle\int_2^\infty \dfrac{\left(x - m \times M_{\rm dust}\right)^2}{(\overline{\sigma_{A_V\,\rm reg}}^2 + \sigma^2)}\,{\rm d}x, & A_V + dA_V \geq 2 \end{cases} \tag{2.3}$$

where $A_V + dA_V$ is that of the best-fit SFH for that region and $\overline{\sigma_{A_V\,\rm reg}} = C/\sqrt{N_{\rm stars}}$. $N_{\rm stars}$ is the number of stars in the nth region and C is calculated such that the resulting values of m and σ do not depend on $N_{\rm stars}$. In this case, $C = 12$. We split χ^2 into two solutions to account for the fact that we have set an upper limit of $A_V + dA_V = 2.5$ in our analysis. As we have shown in Appendix 2.7.2, the best-fit extinction parameters are effectively lower limits in some of our regions. As a result, we assume that all regions with $A_V + dA_V \geq 2$ are lower limits.

We find that a line with $m = 4.5 \times 10^{-6}$ and $\sigma = 0.6$ results in the fit that best helps us

constrain the regions with low SFR and high dust. We apply this prior to our results in all regions by recomputing the fit values for each (A_V, dA_V) pair. The new fit value is given by

$$fit_{\rm new} = fit_{\rm old} + \frac{(A_V + dA_V) - m \times M_{\rm dust}}{\sigma^2} \tag{2.4}$$

We compare the A_V and dA_V values corresponding to the new fits in each region with the dust mass. The results are shown on the right side of Figure 2.17. Applying the prior did tighten up the relation a little bit, reducing the number of outliers on both tails at the low SFR end.

Chapter 3

EXAMINING OBSCURED STAR FORMATION BY MODELING ULTRAVIOLET FLUX IN M31

We present synthetic far- and near-ultraviolet (FUV and NUV) maps of M31, both with and without dust reddening. These maps were constructed from spatially-resolved star formation histories (SFHs) derived from optical *Hubble Space Telescope* imaging of resolved stars, taken as part of the Panchromatic Hubble Andromeda Treasury (PHAT) program. We use stellar population synthesis modeling to generate synthetic UV maps with a spatial resolution of $\sim$0.01 kpc^2 ($\sim$570 square arcseconds). When reddening is included, these maps reproduce all of the main morphological features in the *GALEX* imaging, including rings and large star-forming complexes. The predicted UV flux also agrees well with the observed flux, with median ratios between the modeled and observed flux of $\log_{10}(f^{\rm syn}_{\rm FUV}/f^{\rm obs}_{\rm FUV}) = 0.005\pm0.24$ and $\log_{10}(f^{\rm syn}_{\rm NUV}/f^{\rm obs}_{\rm NUV}) = -0.027 \pm 0.16$ in the FUV and NUV, respectively. This agreement is particularly impressive given that we used only optical photometry to construct these UV maps. With this verification of the synthetic reddened maps, we use the dust-free maps to examine properties of obscured flux and star formation. We compare our dust-free and reddened maps of FUV flux with the observed *GALEX* FUV flux and FUV + 24 μm flux to examine the fraction of obscured flux. We find that the maps of synthetic flux require that 88% of the FUV flux in M31 is obscured by dust, while the observed maps suggest that 71% of the light emitted by young stars is absorbed by dust. This discrepancy is driven by the difference between the dust-free synthetic FUV flux and the observed FUV flux corrected for dust with 24 μm data. The difference is further illustrated when we compare the SFRs derived from the FUV + 24 μm flux with the 100 Myr average SFR from the CMD-based SFHs. We find that the 24 μm-corrected FUV flux underestimates the SFR by a factor of

$\sim$2.5. This discrepancy could be reduced by allowing for variability in the weight applied to the 24 μm data, as has been recently suggested in the literature.

3.1 Introduction

The star formation rate (SFR) of a galaxy is an extremely astrophysically important quantity, a key component to understanding the detailed evolution of a single galaxy or that of a population of galaxies across cosmic time. To this end, the ultraviolet (UV) is one of the most diagnostically important parts of a galaxy's spectrum. It is often interpreted as a measure of recent star formation, given that stars younger than 300 Myr, including young, massive O and B stars, emit most of their energy in the UV (e.g., Kennicutt & Evans 2012). Additionally, the UV is essential for tracing star formation across cosmic time. At high redshift, the light observed in the optical is the galaxy's rest frame UV, which has been redshifted to longer wavelengths.

The UV, however, is also one of the most challenging parts of the spectrum to interpret reliably. While it is generally a good measure of recent star formation, the UV is also highly sensitive to dust. UV light is absorbed by dust grains, which re-emit in the infrared. Consequently, UV-only star formation rates (SFRs) underestimate the true SFR of a galaxy, usually by factors of a few in typical disk galaxies (e.g., Kennicutt 1998; Leroy et al. 2012), though it can be as much as a factor of 100 or more in ULIRGS (e.g., Schmitt et al. 2006). In addition, theoretical progress is difficult because the stellar models for the UV are difficult to create and are neither well tested nor well-calibrated (e.g., Pradhan et al. 2014). Models are particularly problematic for highly evolved low-mass stars, which also emit modestly in the UV (e.g., Code 1969; O'Connell et al. 1992; Dorman et al. 1993; Rosenfield et al. 2012; Johnson et al. 2013). UV flux from older stellar populations is therefore difficult to interpret (Conroy 2013). Finally, UV observations are difficult for low-redshift galaxies because they requires a space or balloon-borne mission, like the *Galaxy Evolution Explorer* (*GALEX*; Martin et al. 2005), the UVOT camera on *Swift* (Gehrels et al. 2004), or the UVIS channel on the Wide Field Planetary Camera 3 (WFC3/UVIS) aboard the *Hubble Space Telescope*.

Further complications when interpreting UV observations arise from assumptions on the initial mass function (IMF) and the SFR. Models generally assume that (1) the IMF is fully populated and (2) that the SFR is constant at recent times. The first of these assumptions is likely to hold only over large areas or in small but high star formation surface density regions. The second requirement arises because, at UV wavelengths, up to 90% of the emission in the far UV (FUV) and near UV (NUV) is from stars that are younger than 100 Myr and 300 Myr, respectively; conversion to a SFR therefore assumes that the SFR has been uniform over that period of time (e.g., Kennicutt & Evans 2012).

Although a wide range of science is enabled with these assumptions, the circumstances under which they are reliable remain unclear. For example, recent work on the IMF has shown that for sufficiently low SFRs and/or small spatial scales, the high-mass IMF is not fully populated (da Silva et al. 2012, 2014; Krumholz et al. 2015), and may even systematically vary (e.g., Meurer et al. 2009). Similarly, in low-mass galaxies and/or on small spatial scales in large galaxies, SFHs tend to be bursty as opposed to constant (e.g., Lee et al. 2009; Weisz et al. 2012). The consequences of these deviations from the fiducial assumptions are not well-understood and may have a significant impact on our interpretation of the observed flux and consequently on the SFR.

Given the astrophysical importance of SFR measurements, tests of the above models and assumptions are crucial. A number of studies have examined how interpreting the observed galaxy flux is affected by some of these assumptions (e.g., Lee et al. 2009; Chomiuk & Povich 2011; Weisz et al. 2012; Wilkins et al. 2012; Johnson et al. 2013; Boquien et al. 2014; Simones et al. 2014, among many others). In a recent paper, Boquien et al. (2015) analyzed the scale dependence of SFR tracers. They found broad agreement between tracers on $\sim$1 kpc scales, presumably because variations between regions of active star formation and diffuse emission (i.e., from older stellar populations) have averaged out. The scale at which this occurs will vary from galaxy to galaxy depending on the intensity of star formation as well as the structure and transparency of the interstellar medium.

In this paper, we take an alternate approach to SFR analysis that sidesteps some of the

above assumptions. We use SFHs and dust distributions derived from resolved stars and stellar population synthesis models to create maps of synthetic FUV and NUV flux on sub-kpc scales. The SFHs come from Lewis et al. (2015), who used optical[1] resolved star data, taken as part of the Panchromatic Hubble Andromeda Treasury (PHAT; Dalcanton et al. 2012; Williams et al. 2014) program, to model the spatially-resolved recent SFH of ∼9000 regions (∼0.01 sq. kpc in size) in the northeast quadrant of M31 (Figure 3.1). Use of these detailed SFHs allows us to relax the constant SFR assumption, and the poisson likelihood sampling in the SFH derivation process implicitly corrects the SFHs for IMF sampling, which is included in the uncertainty estimate. We compare the synthetic flux maps with far- and near-UV *GALEX* observations(Morrissey et al. 2007) to analyze the effect of non-constant SFHs on UV flux over a wide range of environments within a single galaxy. This methodology facilitates an end-to-end test verifying the connection between massive star formation, UV flux, and the ability to interpret and/or infer UV populations through analysis of optical stellar populations.

Simones et al. (2014) initiated this work in M31, using techniques similar to that of Johnson et al. (2013) to model the UV flux in 33 star-forming regions in M31's star-forming ring and compare UV flux-derived SFRs to those measured optical CMD-derived SFHs. They found that the SFRs derived from color-magnitude diagrams (CMDs) were, on average, consistent with those derived from extinction-corrected FUV flux to within 1σ, and $\sim 1/3$ of that scatter can be attributed to metallicity differences: the flux calibration assumes constant solar metallicity, while the metallicity of the SFHs varies with time. Additionally, Simones et al. (2014) found that a wide range of SFHs can produce the same amount of FUV flux.

The analysis of resolved stellar populations offers a different way to probe the effects of simplifying assumptions on integrated flux measurements. Unfortunately, tests such as the one performed by Simones et al. (2014) have been limited in scope, both due to the

[1]Although PHAT includes data in two UV filters (F275W and F336W), that data is not used in this analysis. Only the brightest main sequence stars have measurements in these filters, severely limiting the age range over which the SFH would be reliable. The optical data are the deepest and therefore provide the best leverage on measuring the SFH.

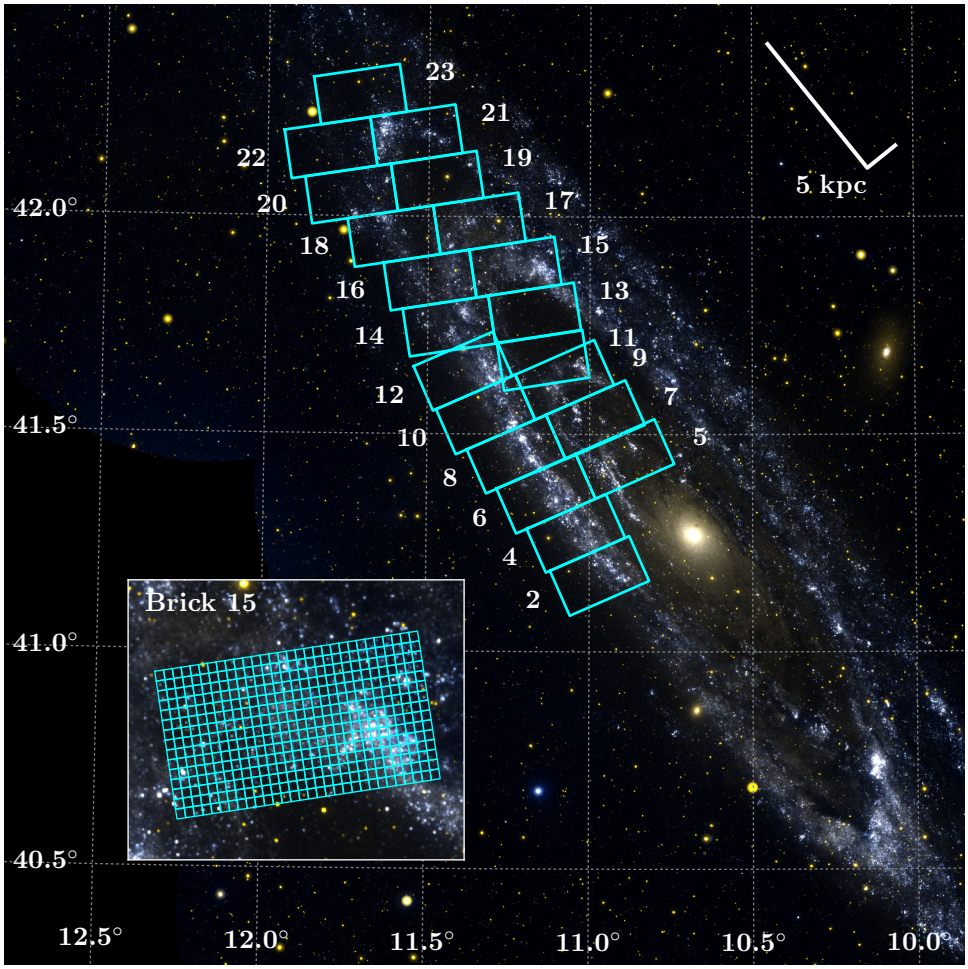

Figure 3.1 Map of the PHAT survey area. The 21 PHAT bricks analyzed in this study are outlined and numbered. Each brick was divided into 450 regions on a 15×30 grid, as shown for Brick 15 in the inset panel. The SFHs for each region are presented in Lewis et al. (2015). We note that Bricks 1 and 3 (nearest to the center of the galaxy) are not used in the present study because their CMDs are too shallow for reliable SFH determination. In the upper right of the image we include a scale bar denoting 5 kpc along the major and minor axes of the galaxy. The image is oriented such that north is up and east is to the left.

inability to gather the required resolved star data outside of the Local Group and because the vast majority of galaxies in the nearby universe are dwarf galaxies. Johnson et al. (2013) explored the connection between the UV and resolved stellar populations in nearby low-mass, low-metallicity dwarf galaxies using SFHs from the ACS Nearby Galaxy Treasury program (ANGST; Dalcanton et al. 2009; Weisz et al. 2011). They found that fluctuations in the SFH can cause factor of two variations in UV luminosities relative to constant SFR assumptions, and that stars older than 100 Myr can contribute up to 30% of FUV emission.

Performing this work in a large, Milky Way-like galaxy is important. In the nearby universe, we are limited to only a few large spiral galaxies. Of those, M31 data has the widest wavelength coverage, the best resolved star data, and the highest resolution. M31 is a more massive and metal-rich system than nearby dwarf galaxies, providing an important laboratory for testing the assumptions made when using integrated UV light. While the method for studying UV populations is the same as that in lower-mass systems, M31's environment is critical because it is similar to that in which most stars are formed.

This paper is organized as follows. In Section 3.2, we describe the SFH dataset and the *GALEX* FUV and NUV images used, and the production of the synthetic flux maps. Section 3.3 describes the creation of the UV maps, including the methodology used to model the UV fluxes and the manner in which we assembled the maps. We present the maps in Section 3.4 and discuss factors that affect the synthetic maps, including a discussion of uncertainties in the modeling. In Section 3.5, we examine results from this analysis, including the fraction of obscured star formation and comparison of SFR calibrations. We discuss the factors that affect our results in Section 3.6. We conclude in Section 3.7.

3.2 Data

3.2.1 GALEX UV Images

We take UV observational data from the *GALEX* Deep Imaging Survey (DIS; Martin et al. 2005). We use the five tiles that cover the PHAT survey in the FUV and NUV, converting

the count rate units, cps, into flux according to

$$f = U \left(\frac{\mathrm{cps}}{\mathrm{counts\,s^{-1}\,pixel^{-1}}} \right) , \tag{3.1}$$

where U, the *GALEX* unit response, is given in Table 3.1. A small amount of background UV flux was present in the FUV and NUV mosaics, primarily due to scattering of UV photons from hot foreground stars in the Galaxy. We measured the median background flux in four 0.6×0.6 square degree apertures in an off-galaxy area relatively devoid of stars. The apertures were centered at (RA, dec) values of (9.9, 42.5), (10.8, 42.7), (10.8, 42.2), and (10.1, 42.1). We took the mean of the four regions and subtracted this value from all image pixels. The subtracted background in the FUV (NUV) images was 2.04×10^{-16} (3.13×10^{-16}) $\mathrm{erg\,s^{-1}\,cm^{-2}\,\AA^{-1}}$, respectively. This is a first estimate of the background in each image. These values result in slight underestimates in the FUV and overestimates in the NUV at the low flux end. In order to bring these values back into line, we subtract and additional 9.25×10^{-17} $\mathrm{erg\,s^{-1}\,cm^{-2}\,\AA^{-1}}$ from the FUV and add back in 5.22×10^{-17} $\mathrm{erg\,s^{-1}\,cm^{-2}\,\AA^{-1}}$ in the NUV. We explain how we got these numbers in Section 3.3.3. This results in total background values of 2.96×10^{-16} $\mathrm{erg\,s^{-1}\,cm^{-2}\,\AA^{-1}}$in the FUV and 2.60×10^{-16} $\mathrm{erg\,s^{-1}\,cm^{-2}\,\AA^{-1}}$ in the NUV.

3.2.2 PHAT SFHs

To model UV flux, we use the PHAT spatially-resolved recent SFHs determined in Lewis et al. (2015). We briefly describe their derivation here, but refer readers to the original paper for details. Each brick in the PHAT survey was divided into 450 regions on a uniform 15×30 grid with a total of ∼9000 regions across the survey area, excluding the bricks closest to the crowded bulge area (see Figure 3.1). Each region was approximately $24'' \times 27''$ (100 pc × 100 pc, projected; 100 pc × 400 pc, deprojected). For each region, they modeled the optical (F475W and F814W) CMD using the fitting code `MATCH` (Dolphin 2002), which compares the observed CMD with many synthetic CMDs for composite stellar populations over a range of

ages and metallicities. As described in detail in Lewis et al. (2015), the SFHs were derived with the following assumptions:

1. A Kroupa (2001) IMF.

2. Padova isochrones (Marigo et al. 2008) with updated asymptotic giant branch (AGB) tracks (Girardi et al. 2010).

3. A distance modulus of 24.47, corresponding to a distance of 783 kpc (McConnachie et al. 2005).

4. A binary fraction of 0.35 with a uniform mass ratio.

5. Age resolution of 0.1 dex for log(time) = 6.6 – 9.9 and 0.25 dex for log(time) = 9.9 – 10.15

6. Metallicity resolution of 0.1 dex over the range $-2.3 \leq$ [M/H] ≤ 0.1, with the requirement that [M/H] increases with time.

7. A two-parameter extinction model consisting of a foreground component, A_V, applied evenly to all stars, and an additional differential component, dA_V following a uniform distribution, such that all stars in a region are extincted by some amount between A_V and $A_V + dA_V$, optimized for each region individually (see also Simones et al. 2014). These values are used in a Cardelli et al. (1989) extinction model with $R_V = 3.1$.

Additionally, the portion of each CMD with F475W > 21 and F475W $-$ F814W > 1.25 (red giant branch and red clump stars) was excluded from the fit (see the CMDs in Figures 2 and 3 of Lewis et al. 2015). This choice mitigates extinction effects from older stellar populations which are not well fit with the single step function described in item 7 above. As a result, the optimized extinction parameters correspond only to the dust associated with young, UV-emitting stars on the main sequence. We refer the reader to Dalcanton et al. (2015) for a robust analysis of the dust in M31.

3.3 Map Creation

3.3.1 Modeling Ultraviolet Flux

We used the SFHs described in Section 3.2.2 to create spatially-resolved broadband FUV and NUV flux maps for the PHAT survey area. We modeled the flux in each region using a technique similar to that described in Johnson et al. (2013). We generated a set of simple stellar population (SSP) models and then weighted those models by the SFH to calculate the integrated spectral energy distribution (SED) for a given region. We ultimately determined the FUV and NUV flux and magnitude of each region from its modeled SED.

We first constructed a set of SSPs using the Flexible Stellar Population Synthesis (FSPS) code (Conroy et al. 2009; Conroy & Gunn 2010), assuming a Kroupa (2001) IMF and the Padova isochrones (Marigo et al. 2008) with updated AGB tracks (Girardi et al. 2010) and using the BaSeL 3.1 semi-empirical stellar SED library (Westera et al. 2002). In FSPS, the Geneva tracks (Meynet et al. 1994) are used at log(time)<6.6 for high-mass stars, supplemented with the Padova models for low mass stars. These choices are consistent with the SFH determination. We constructed the SSPs with an age resolution of 0.025 dex over the range log(age) from 5.500 to 10.175. We set the SSP metallicity to the mean metallicity over the last 100 Myr, as derived from the SFH. If there was no star formation over that time range, we set the metallicity to that of the most recent time when the SFR was non-zero.

To link the SSPs to the SFH, we needed to reprocess the SFH. The `MATCH` implementation of the Padova isochrones only reaches to log(time) = 6.6, so we renormalized the SFR in the youngest age bin to reach time = 0, conserving the mass created in that time bin:

$$\begin{aligned} &\mathrm{SFR}(t = 0 - 10^{6.7}\,\mathrm{Myr}) = \\ &\qquad \mathrm{SFR}(t = 10^{6.6} - 10^{6.7}\,\mathrm{Myr}) \times \left(1.0 - \frac{10^{6.6}}{10^{6.7}}\right). \end{aligned} \tag{3.2}$$

We also increased the age resolution of the SFH to $\sim 6.5 \times 10^4$ yr. We determined this value by splitting the smallest time bin into 20 separate bins. In log(time) space we then interpolated the SSP SEDs to the SFH time points, weighted each interpolated SED by the SFR at each

SFH time point, and summed the SEDs to create the integrated intrinsic (i.e., dust-free) model SED. We note that we used the full 14 Gyr SFH in this process despite the fact that Lewis et al. (2015) stress that the SFHs are only robust to ∼500 Myr ago. We will discuss the effects of the SFH timescale in Section 3.8

To include the effects of dust, we created the integrated, attenuated model SED in the same manner as the intrinsic SED, except that we reddened each individual SSP SED component before weighting by the mass. To redden the SED, we split each SSP SED into 30 identical component SEDs. Each component was then attenuated according to the Cardelli et al. (1989) extinction curve with $R_V = 3.1$, assuming a uniform random A_V distribution drawn between $A_{V,\mathrm{SFH}}$ and $A_{V,\mathrm{SFH}} + dA_{V,\mathrm{SFH}}$, where $A_{V,\mathrm{SFH}}$ and $dA_{V,\mathrm{SFH}}$ are the best-fit parameters of the two-component extinction model used to derive the SFH from the CMD (Lewis et al. 2015).

We summed all of the attenuated components to create each region's integrated attenuated model SED. We note that the Cardelli et al. (1989) extinction curve, which predicts the amount of extinction relative to that in the V band as a function of wavelength, is based on the average $R_V = 3.1$ extinction curve for the Galaxy. Previous studies have shown that this extinction curve is applicable to M31 as a whole in both the UV (Bianchi et al. 1996) and the optical (Barmby et al. 2000) regimes. However, individual sight-lines may differ from $R_V = 3.1$ due to metallicity, gas-to-dust ratio, or star formation activity (Clayton et al. 2015).

To determine the UV magnitude, we projected each model SED (both intrinsic and attenuated) onto the response curves for the *GALEX* FUV and NUV filters to obtain absolute synthetic FUV and NUV magnitudes in the AB system. We converted the resulting absolute magnitude to apparent magnitude assuming a distance modulus of 24.47 (McConnachie et al. 2005).

Finally, we convert the magnitude to flux using:

$$m = -2.5 \log_{10} \left(\frac{f}{U} \right) + Z \ , \tag{3.3}$$

where U is the *GALEX* unit response, and Z is the zeropoint, given for each filter in Table

Table 3.1. *GALEX* filter properties.

	FUV	NUV
Unit response, U ($\times 10^{-15}$ erg s^{-1} cm^{-2} Å^{-1})[a]	1.40	0.206
AB magnitude zeropoint, Z	18.82	20.08

[a]`http://asd.gsfc.nasa.gov/archive/galex/FAQ/counts_background.html`

3.1.

Throughout the text, we refer to the synthetic intrinsic (un-reddened) flux as $f^{\rm syn,0}$ and the synthetic reddened flux as $f^{\rm syn}$. The same nomenclature is used when referring to synthetic magnitudes as well.

We note that this process can be applied when modeling the flux at any wavelength, although appropriate care must be taken in the IR, where dust geometry and radiative transfer effects also need to be considered.

3.3.2 Creating Maps of Synthetic Flux

We used the modeled FUV and NUV fluxes in each region to create a single map of the PHAT survey area at each wavelength. We created these maps with Montage[2], which aids in the combination of many FITS images into a single mosaic. Montage is flux-conserving and maintains the photometric and spatial fidelity of the input images.

Because the SFHs were derived on a 15×30 grid in each brick, we assembled the modeled flux values for each UV filter into a 15×30 array to create a brick image. We then tied each brick image independently to a world coordinate system using the RA and Dec coordinates of the SFH brick grid. We then let Montage determine the single template header that best

[2] `http://montage.ipac.caltech.edu`

describes the combination of input images and used that header to re-project each brick image to the same WCS. We co-added the re-projected images into a single FITS file to create full PHAT survey area maps of synthetic FUV and NUV flux. The pixels in the resulting co-added image have a scale of $23.7''$. Due to the reprojection, the input regions do not match one-to-one to the output image pixels.

Assuming a distance modulus of 24.47 (McConnachie et al. 2005), a disk inclination of 77° (e.g., Roberts 1966; Brinks & Burton 1984; Walterbos & Kennicutt 1988), and a major axis position angle of 35° (de Vaucouleurs et al. 1995), the pixel scale deprojects to a linear size of $440\,\mathrm{pc}\times100\,\mathrm{pc}$ along the minor and major axes of M31, respectively (see orientation of scale bar in Figure 3.1). The synthetic flux maps therefore have a resolution that is firmly in the sub-kpc regime.

Montage creates a pixel weight map during the mosaicking process. All pixels are weighted according to the fraction of the pixel that is inside the PHAT footprint (i.e., pixels entirely inside the footprint have a weighting of 1, pixels entirely outside of the PHAT footprint have a weighting of 0, and pixels that are partially within the footprint have a weighting somewhere between 0 and 1). To remove possible border effects, we only analyze pixels that have a weight $w > 0.95$.

3.3.3 Turning GALEX Observations into Maps

We also constructed maps of observed *GALEX* flux (f^{obs}), matched to the sampling of the modeled synthetic flux maps. The process was similar to that used for the synthetic maps. Starting with the background-subtracted images described in Section 3.2.1, we reprojected the flux tiles to the same template header as the synthetic flux maps. We then background-matched the images by determining the differences in the images at their overlaps and fitting a plane to these difference images to model the background. We then added the matched images to create the final observed maps.

As described in Section 3.2.1, we removed background UV flux from the original *GALEX* images before combining them into maps. However, after creating the full maps, the distribu-

tion of $f^{\rm syn}/f^{\rm obs}$ showed a significant downturn/upturn for pixels where $f^{\rm obs}$ was comparable to the background,. This behavior indicated a slight underestimation/overestimation of the background levels in the FUV/NUV. To correct this, we adjusted the background levels such that the median $\log_{10}(f^{\rm syn}/f^{\rm obs})$ value for all pixels with $f^{\rm obs}$ smaller than the median of $f^{\rm obs}$ ($10^{-15.5}$ erg s^{-1} cm^{-2} Å^{-1} for FUV and $10^{-15.6}$ erg s^{-1} cm^{-2} Å^{-1} for NUV) matched that for all pixels brighter than the median value and fainter than $10^{-14.2}$ (the bright pixels are underestimated in the synthetic NUV data). We subtracted these additional background values (9.25×10^{-17} erg s^{-1} cm^{-2} Å^{-1} in the FUV and -5.22×10^{-17} erg s^{-1} cm^{-2} Å^{-1} in the NUV) from the respective mosaics to obtain the final observed UV flux maps for the PHAT survey area.

These corrections only affect pixels with values comparable to the background or fainter. For the brighter pixels, the background subtraction method makes little difference.

3.4 Verification of the Optically-derived Synthetic Ultraviolet Maps of the PHAT Survey

3.4.1 Presentation of the Maps

In Figures 3.2 and 3.3 we show maps of observed *GALEX* flux ($f^{\rm obs}$; §3.3.3), synthetic attenuated flux ($f^{\rm syn}$; §3.3.1 and §3.3.2), and the significance of the difference between the two over the PHAT survey area for the FUV and NUV, respectively. All figures have the same stretch.

Figures 3.2 and 3.3 show remarkable qualitative agreement between the synthetic and the observed fluxes, indicating that the synthetic attenuated fluxes derived from the optical CMDs do an excellent job at reproducing the observed fluxes. All of the main features of the *GALEX* maps are reproduced in the synthetic maps, including the 10 kpc ring, the ring features at 5 and 15 kpc, and the individual star-forming regions within the ring, as well as the OB associations in Bricks 15 and 21 (the bright features located at the top and right side of the left two panels in Figures 3.2 and 3.3; also see Figure 3.1 for brick numbering). The agreement is especially good in the FUV map, but also apparent in the NUV map, despite

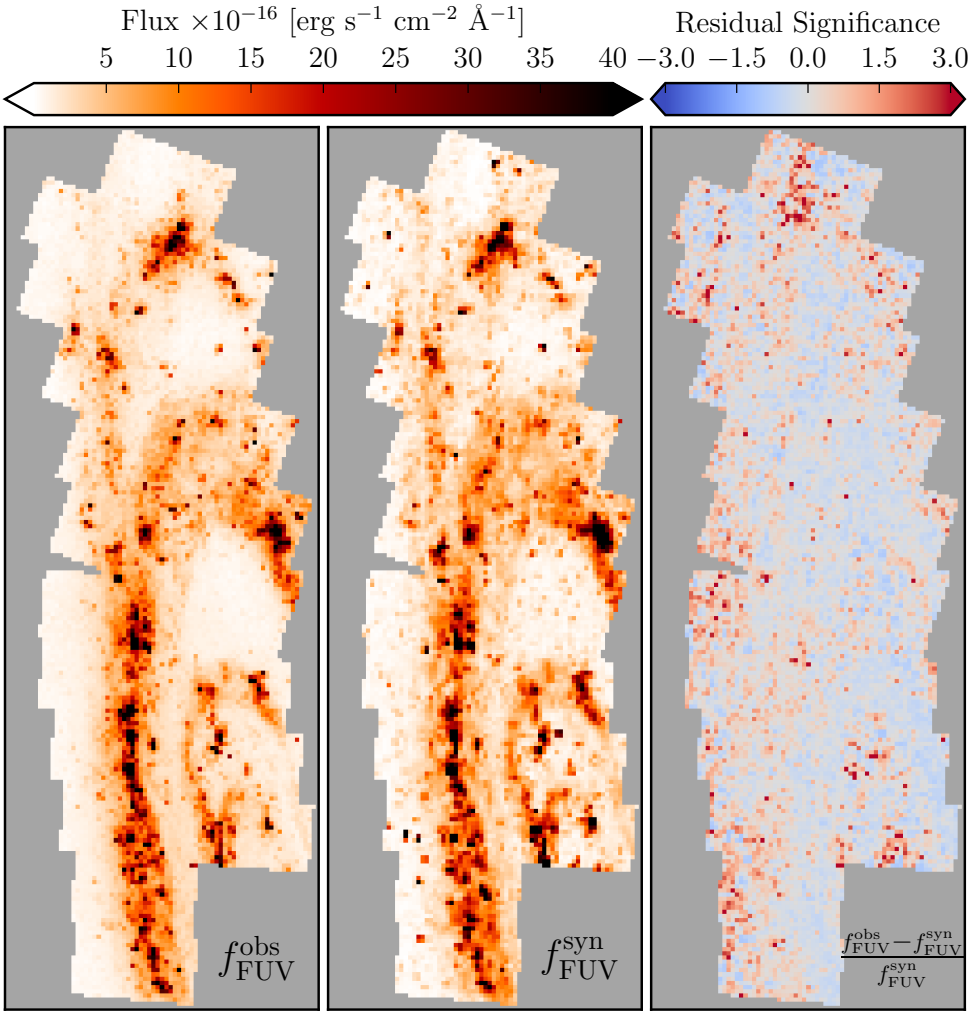

Figure 3.2 The observed *GALEX* FUV flux, $f_{\rm FUV}^{\rm obs}$, is shown in the left panel. The middle panel shows the synthetic flux derived from optical SFHs and attenuated according to a Cardelli extinction model, $f_{\rm FUV}^{\rm syn}$. These maps are on the same flux scale as indicated by the color bar above the left two panels. The right panel shows the significance of the residuals, plotted as ($f^{\rm obs}$ - $f^{\rm syn}$) / $f^{\rm syn}$. Bluer colors are where the modeled flux is over-predicted and redder colors are where it is under-predicted. The value indicates the sigma deviation. Most of the regions are within 1-σ. The bright red pixels in B23 and outside of the 10 kpc ring show a 2+σ under-prediction of the flux.

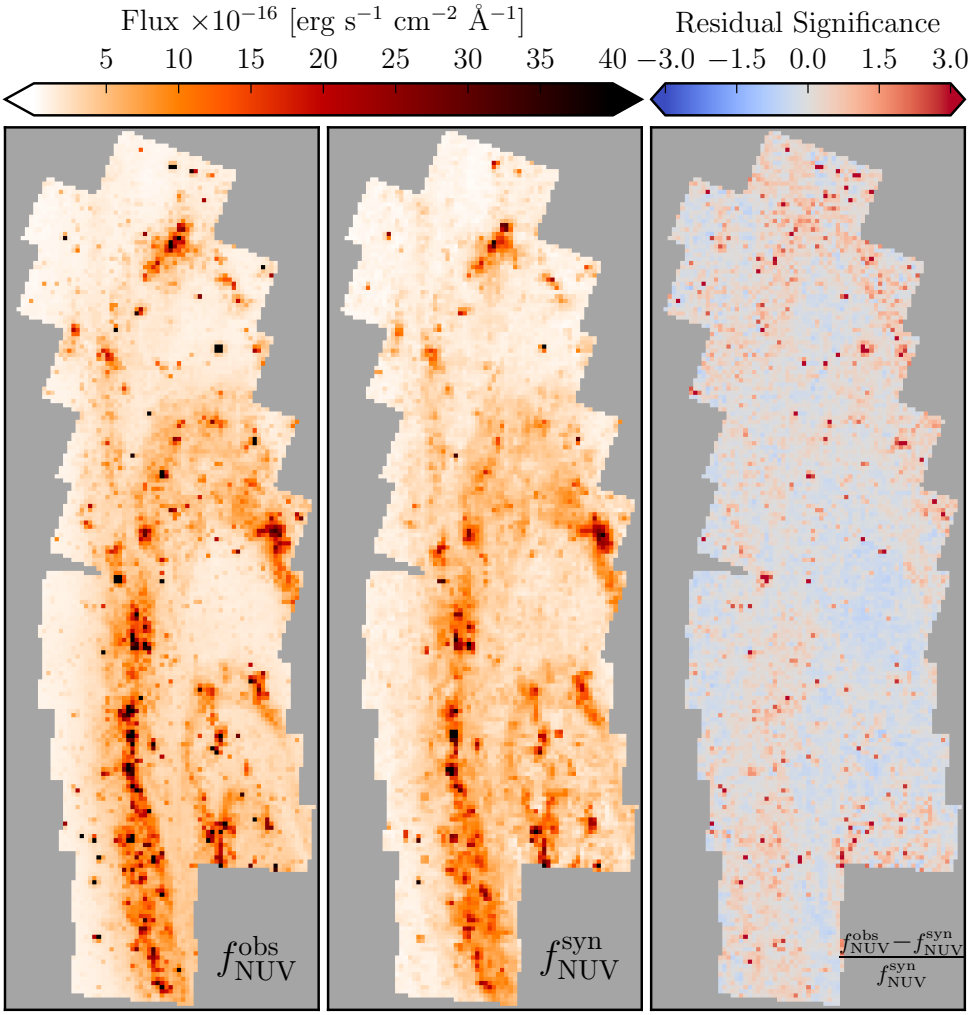

Figure 3.3 Same as Figure 3.2 except showing the NUV results. The left panel shows the observed flux, $f_{\rm NUV}^{\rm obs}$, the middle panel shows the modeled, attenuated flux, $f_{\rm NUV}^{\rm syn}$, and the right panel shows the significance of the residuals between the two, $f_{\rm NUV}^{\rm syn,0}$.

the fact that some features are not as defined in the synthetic map. We emphasize that we have used *optical* colors and magnitudes to derive the *ultraviolet* fluxes.

There are, however, distinct differences between the $f^{\rm syn}$ and $f^{\rm obs}$ maps. For example, the $f^{\rm obs}$ maps show some point-like sources that do not appear in the $f^{\rm syn}$ maps. Inspection of the original images shows that these sources are largely Milky Way foreground stars. Foreground stars are typically at a very different absolute magnitude than M31 stars, and it is unlikely that any foreground stars were inadvertently included in the CMD modeling. Additionally, foreground stars don't produce features in the synthetic maps because the fluxes in those maps are derived from the SFR of a *distribution* of stars, rather than single stars, so while a single bright star may dominate the pixel in the observed map, it has less of an effect in the modeled map because it is averaged out in the total SFH from which the modeled flux is derived.

There are also a number of bright pixels in the modeled maps that are not in the observed maps. These mostly correspond to photometric artifacts (primarily diffraction spikes) that remained in the PHAT photometry[3] after application of the quality cuts (Dalcanton et al. 2012). These artifacts increase the apparent stellar mass measurement in the SFH, which increases the synthetic flux. This contamination affects <5% of the pixels.

In Figure 3.4, we present a quantitative comparison of the synthetic and observed fluxes shown in Figures 3.2 and 3.3. We plot the ratio of the modeled reddened flux to the *GALEX* flux ($f^{\rm syn}/f^{\rm obs}$) as a function of *GALEX* flux, including the running median and standard deviation. The overall median and standard deviation are $\log_{10}(f^{\rm syn}_{\rm FUV}/f^{\rm obs}_{\rm FUV}) = 0.005 \pm 0.24$ and $\log_{10}(f^{\rm syn}_{\rm NUV}/f^{\rm obs}_{\rm NUV}) = -0.027 \pm 0.16$. Together with the qualitative comparison in Figures 3.2 and 3.3, these numbers indicate that in both filters, $f^{\rm syn}$ is consistent with $f^{\rm obs}$. The largest discrepancies occur at high observed flux, where the number of regions is very small, and are likely due to foreground stars or other photometric artifacts.

[3] We note that the SFHs derived in Lewis et al. (2015) used the first version of the PHAT photometry. The photometry has since changed, using different quality cuts and resulting in overall improvement. Given the large computing expense to run the SFHs on the entire grid and the minimal difference it would make for the SFHs, it was not deemed worthwhile to re-run the SFHs on the most recent photometry.

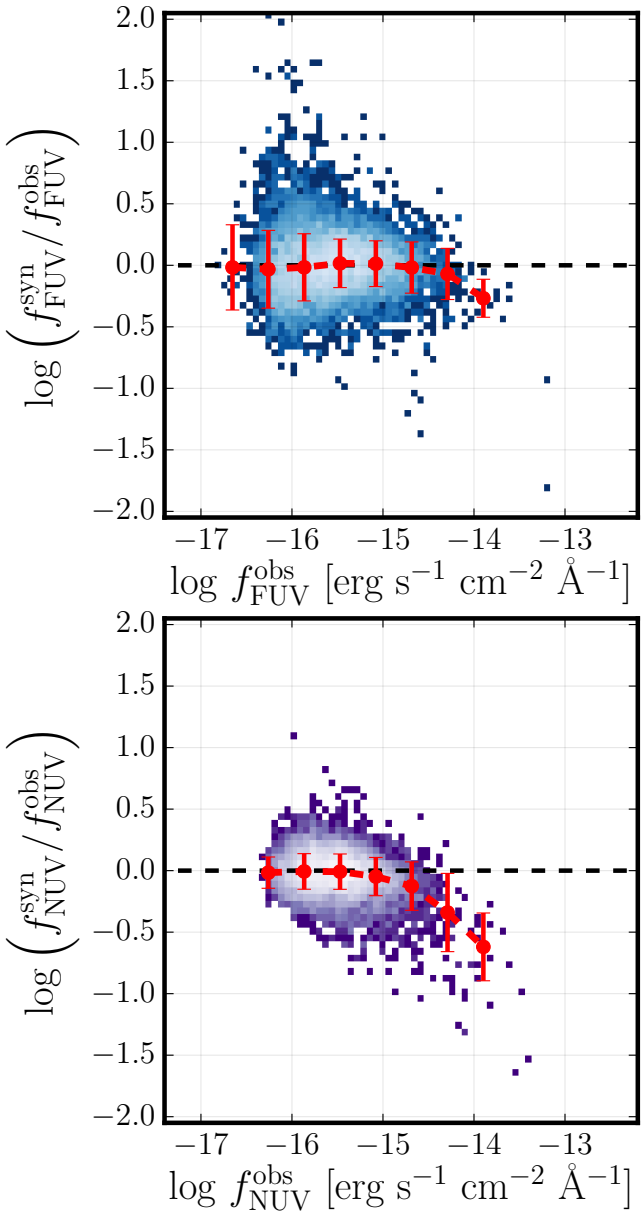

Figure 3.4 The log ratio of the modeled flux to the observed flux as a function of observed flux for all pixels that fall inside the PHAT footprint. The red circles in each panel show the running median with the standard deviation given by the error bars on each point. The median log ratios are 0.005 and -0.027 in the FUV and NUV, respectively. The standard deviation is 0.24 in the FUV and 0.16 in the NUV.

The FUV relation is flat across the range of observed fluxes. The scatter on the best-fit values decreases as the observed flux increases, ranging from 0.3 dex at the low end to 0.1 dex at the high end. The two regions at the highest FUV flux actually correspond to a single bright star located at the intersection of B12 and B14, clearly visible in Figure 1 and in the left panel of Figure 2.

In contrast, the NUV data are much tighter, showing a scatter of $\sim$0.1 dex at low observed fluxes and increasing to $\sim$0.2 dex at the brighter end. There is also a slight trend in the NUV data. The synthetic flux is over-estimated in regions of low observed flux and under-estimated in regions of high observed flux. This behavior can be seen in the right panel of Figure 3.3 where the regions between and outside of the ring features (low observed flux) are blue, indicating more synthetic flux than observed flux, and the ring regions (high observed flux) are red, indicating more observed flux than synthetic flux. At the low flux end, this offset is likely due to background subtraction. Reducing the amount of flux subtracted from all pixels will increase the amount of flux enough at the low flux end to come into agreement with the modeled data. It will not significantly affect the high flux end where the correction is only of order 1%.

At the high flux end of the NUV distribution, the inconsistency must lie with the modeled data. One possibility could be our treatment of dust, because the regions of high flux coincide with the dustiest regions. However, both the FUV and NUV are treated the same way and this problem does not affect the FUV, which should be even more sensitive to errors in the dust model; we cannot assume that the dust is too high in the NUV and just right in the FUV. We note, however, that the NUV band includes the 2175Å bump. If we were to reduce the strength of the bump at the same R_V (e.g., Conroy et al. 2010), this change would increase the flux in the NUV, bringing the ratio of synthetic to observed flux closer to one but leaving the FUV flux unchanged. A variation in bump strength would also have little effect on the low-flux regions which are also generally low-dust regions and are therefore less affected by the robustness of the extinction curve.

A final factor that could contribute to the trend seen in the NUV data is timescale. When

Table 3.2. Fraction of pixels within 1, 2, or 3 Sigma of One-to-One

Bin Center	N		1σ		2σ		3σ	
$\log\left(\mathrm{erg\,s^{-1}\,cm^{-2}\,\AA^{-1}}\right)$	FUV	NUV	FUV	NUV	FUV	NUV	FUV	NUV
-16.65	27	0	0.63	NA	0.96	NA	1.0	NA
-16.25	1302	396	0.76	0.69	0.95	0.96	0.99	0.99
-15.87	2956	3224	0.75	0.70	0.95	0.95	0.99	1.0
-15.47	3218	4311	0.73	0.73	0.95	0.95	0.99	0.99
-15.08	1838	1735	0.73	0.73	0.95	0.93	0.99	0.98
-14.68	640	374	0.78	0.65	0.95	0.89	0.98	0.97
-14.29	126	66	0.71	0.48	0.92	0.82	0.99	0.92
-13.99	12	14	0.33	0.00	0.67	0.50	0.92	0.79

Note. — The first column shows the center of the bin of width 0.4 dex. Columns 2 and 3 indicate the number of pixels that fall within that bin. Columns 4 and 5 show the fraction of pixels in that bin that lie within 1σ of the one-to-one line (the dashed line in Figure 3.4). Columns 6 and 7 show the fraction of pixels that lie within 2σ of the one-to-one line. Columns 8 and 9 show the fraction of pixels that lie within 3σ of the one-to-one line.

we constructed the set of SSPs, we set the metallicity of each SSP to the mean metallicity of the SFH over the last 100 Myr. The 100 Myr timescale is based on the average lifetime of the O and B stars that emit in the FUV, whereas the timescale for NUV emission is longer at 300 Myr. We tested using 300 Myr as the baseline over which to determine the mean metallicity for each SSP and found no difference in the results. M31's metallicity has not changed significantly over the last few hundred Myr.

Despite the systematic trend in the NUV and the larger scatter in the FUV, we find that 70–75% of pixels in both the FUV and the NUV fall within 1σ of the one-to-one line and >97% fall within 3σ. These percentages do not include the brightest single bin in the FUV

and the brightest two bins in the NUV where those numbers are significantly lower. The number of points in each bin as well as the percentage that fall within 1, 2, or 3σ are given in Table 3.2. While we do not match all points perfectly, the degree of agreement is still impressive.

The overall agreement between $f^{\rm syn}$ and $f^{\rm obs}$ confirms that our modeling procedure is generally robust and justifies the assumptions we used to model the flux, including the assumed IMF, stellar models and spectral library, and the extinction model. While the modeling can certainly be made more complex, it is reassuring to know that we can use all of this knowledge to derive SFHs, synthesize SEDs, and successfully recreate detailed maps in the UV, all from photometry in only two optical bands.

3.4.2 Issues Affecting the Synthetic Ultraviolet Maps

The above comparisons strongly support the overall reliability of the SFHs presented in Lewis et al. (2015), particularly the dust parameters derived in the SFH fitting process. Therefore, before we proceed to a discussion of the un-reddened maps, we highlight some additional considerations that could affect the modeled flux.

The *GALEX* data primarily suffers from Poisson uncertainties due to the exposure time. For each of the five DIS images in this study, we assume an average exposure time of 7×10^3 s in the FUV channel and 6×10^4 s in the NUV channel. The uncertainties are only a few percent at $f^{\rm obs}$ $\sim$$10^{-16}$ erg s^{-1} cm^{-2} Å^{-1}. The NUV uncertainties are an order of magnitude smaller.

The scatter in Figure 3.4 is much larger than the above Poisson uncertainties allow. As a result, the scatter seen in Figure 3.4 is most likely dominated by the modeling process. We now discuss possible sources of uncertainty in our synthetic data.

There are four major factors that could contribute to the scatter observed in the synthetic fluxes: (1) SFH uncertainties, (2) IMF sampling incompleteness, (3) differences between the dust model and the physical properties of the dust, and (4) stellar evolution model uncertainties. Because each of these effects is coupled to the others (e.g., the SFH of each

region is dependent on the stellar models used and is also degenerate with the dust in that region), it is difficult to constrain the uncertainties from each source separately to high precision. Instead, we provide a qualitative discussion of each source and its effect on the resulting flux.

SFH Uncertainties

We first consider the role of uncertainties in the SFH. At the native time resolution of 0.1 dex, the uncertainties on the SFR in a single time bin can range from $\gtrsim$10–100%. The exact number depends on the number of luminous main sequence stars in each region (Lewis et al. 2015), which will affect the certainty of star formation happening in one time bin as opposed to the adjacent time bin. These uncertainties naturally decrease when averaged over larger region sizes or longer timescales. The uncertainties on the SFR in Lewis et al. (2015) were determined using a hybrid Markov Chain Monte Carlo routine (Duane et al. 1987) to produce a sample of 10,000 SFHs. To determine the magnitude of the uncertainties propagated through from the SFHs, we ran 1000 of these SFHs in each region through our SED modeling routine. We take the uncertainty on the flux to be the distribution of fluxes derived from this sample. In Figures 3.5 and 3.6, we show the uncertainties in the modeled flux as a function of observed flux and log SFR for both the reddened and dust-free synthetic flux. The uncertainties are highly asymmetric, especially at the low-flux end because of asymmetries in the SFH uncertainties. When the best-fit SFR in a time bin is zero, the uncertainty on that SFR is only positive. The regions that populate the low-flux end of this figure tend to have little or no star formation in the most recent 100 Myr. Over the 100 Myr timescales of interest in this paper, the random uncertainties on the synthetic flux due to the SFH derivation are up to an order of magnitude at the very faint end, though only a factor of a few or less at the bright end.

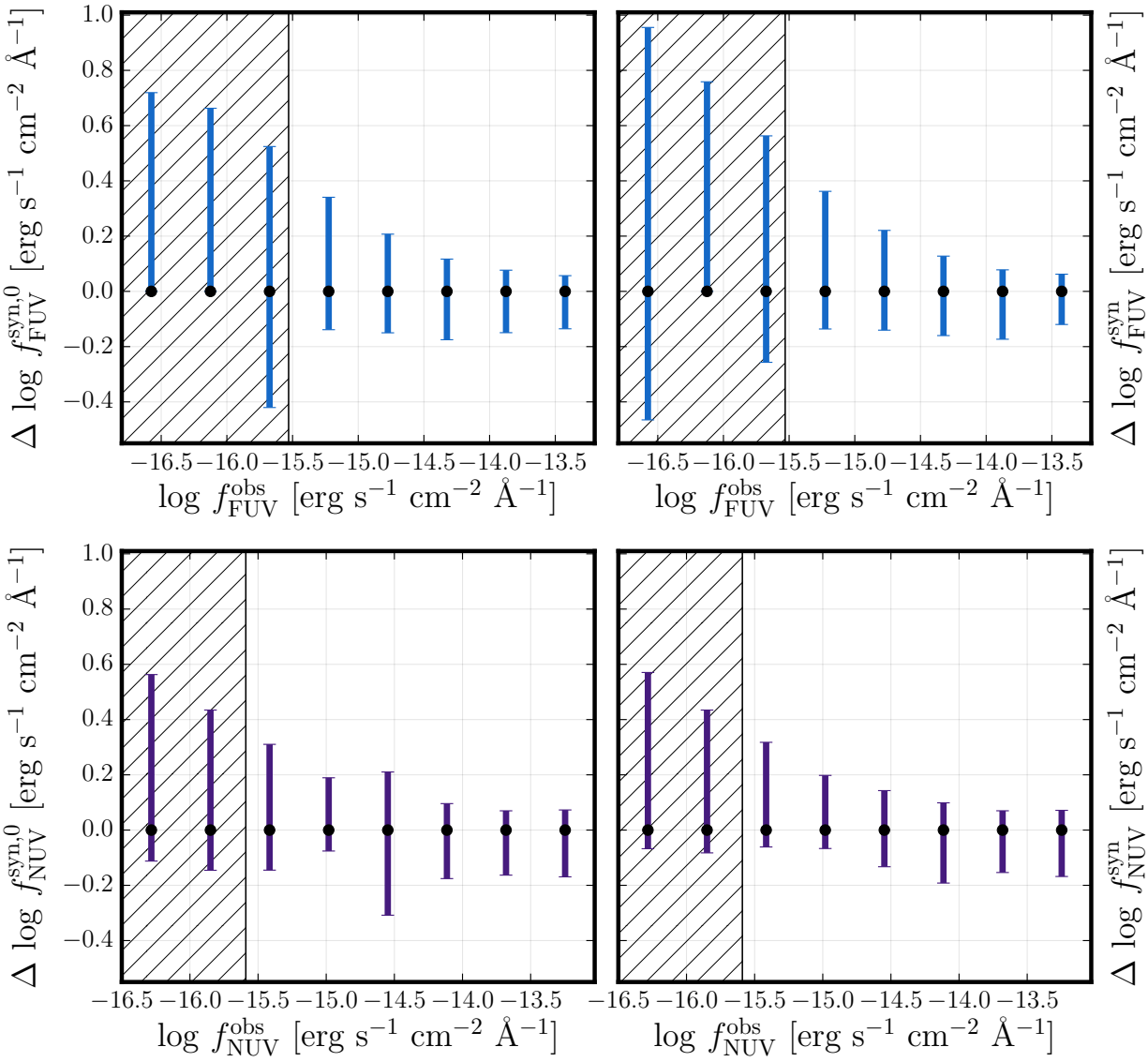

Figure 3.5 Uncertainties on the dust-free and reddened synthetic flux as a function of observed flux. The top panels show the FUV uncertainties and the bottom panels show the NUV uncertainties. Dust-free flux is on the left and reddened flux is on the right. The black vertical line indicates the total background level (Section 3.2.1) and therefore the hatched region indicates the flux levels at which *GALEX* noise takes over.

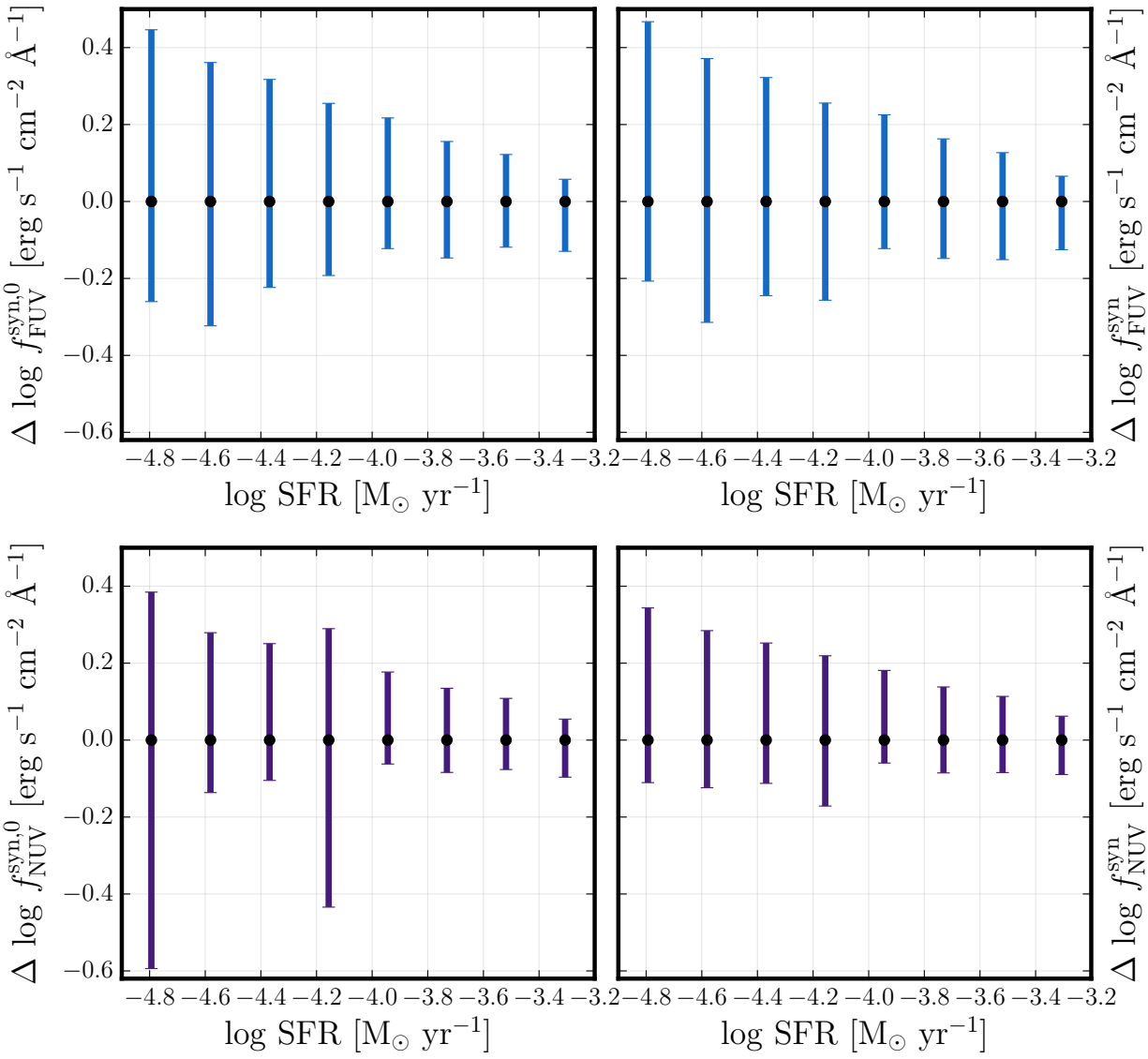

Figure 3.6 Uncertainties on the dust-free and reddened synthetic flux as a function SFR averaged over the last 100 Myr. The top panels show the FUV uncertainties and the bottom panels show the NUV uncertainties. Dust-free flux is on the left and reddened flux is on the right. We have only included SFRs above 10^{-5} $M_\odot\,yr^{-1}$. Uncertainties at lower SFRs are 0.8 – 1.0 dex in the FUV and 0.4 – 0.5 dex in the NUV.

Dust Models

We next consider uncertainties in the dust model used to model the SFHs and the flux. As described in Lewis et al. (2015), we modeled dust in the optical CMD-derived SFHs with a two-component top-hat model designed to account for constant extinction along the line of sight, and differential extinction internal to the galaxy. The CMD residuals suggest that this model is reasonable for the young stars, but extrapolation of this model to the UV requires assumptions about the attenuation curve and the 2175 Å bump. In the modeling process, we assume that the attenuation curve, R_V, and the strength of the 2175 Å bump are constant across the disk. However, it is possible that these have spatial variation, and this could lead to scatter in the flux ratios. Robust SED fitters, such as the BEAST (K. Gordon et al. 2016, submitted) may be able to measure such region-to-region variation.

Incomplete Sampling of the IMF

A third source of uncertainty is incomplete sampling of the stellar IMF. The UV light in a region is highly dependent on the number of massive stars. In modeling the SFHs, we assumed a fully-sampled IMF. When the SFR $\lesssim 10^{-4}$ $\mathrm{M_\odot\,yr^{-1}}$, however, the IMF may not be fully populated in that there are too few massive stars. This is most likely to occur in regions that are physically small or regions where the SFR is low or non-existent. That said, low flux regions tend to contain mostly older stellar populations. As such, stochastic effects do not make as much of a difference because the UV is coming from stars further down the luminosity function. In high-flux and high-SFR regions, a scale of 30 – 40 pc (approximately the size of a $4000\,\mathrm{M_\odot}$, 5 Myr old cluster) appears to be large enough to avoid IMF sampling issues (Boquien et al. 2015). Additionally, several studies have shown that stochastic sampling of the IMF – even at very low SFR – has less impact on the FUV and NUV fluxes because they result from integration over a wide mass range and are less dependent on the most massive stars than an ionizing luminosity such as Hα (e.g., Lee et al. 2009, 2011; da Silva et al. 2012; Johnson et al. 2013; da Silva et al. 2014).

In general, the 100 pc × 400 pc regions in this study are more than large enough to avoid effects of stochastic sampling in high SFR regions. In lower SFR regions, stochastic sampling could potentially affect our results. However, incomplete sampling of the IMF does not overwhelmingly contribute to the observed scatter in the flux ratios. The FUV and NUV fluxes are integrated over a stellar mass that reaches down to ∼3-5 $M_\odot$ on the main sequence. Additionally, stochastic effects of the IMF are incorporated into the uncertainties on the SFHs as described in Lewis et al. (2015). Consequently, it is unlikely that incomplete sampling of the IMF contributes significantly to the scatter in the flux ratios beyond the uncertainties already accounted for in the SFH measurements.

Stellar Models

The last source of uncertainty is from deficiencies in the stellar models used to derive the SFHs and to model the flux. Just as the number of massive stars affects the observed UV light, discrepancies between the synthetic and true UV properties of these massive, metal rich stars could introduce scatter into the flux ratios. This uncertainty is the most challenging to quantify. The fidelity of the stellar models will be the same in all locations, but the impact of the models will vary from region to region due to variation with stellar type and mass and therefore with SFH and IMF sampling. Perhaps most importantly, stellar models in the UV are poorly calibrated due to the paucity of massive, metal-rich stars in the local universe.

Therefore, based on the above effects, the scatter in the flux ratios shown in Figure 3.4 is dominated by the uncertainties in the SFH, which include scatter due to incomplete sampling of the IMF.

3.4.3 Emission Timescales

Fluxes in the FUV and NUV are often attributed to timescales of <100 Myr and <300 Myr, respectively, because most of the UV emission comes from the hottest, most massive stars that dominate younger stellar populations (Kennicutt & Evans 2012). It has also been shown

that older populations emit in the UV as well (e.g., O'Connell 1999), with often as much as 20-30% of the total emission in the FUV or NUV coming from these stars (e.g. Johnson et al. 2013). The contribution from older populations is generally negligible in regions of high recent star formation. However, in regions of low SFR, this contribution can be non-negligible, particularly in the NUV. Unfortunately, the CMD modeling in Lewis et al. (2015) excluded regions of the CMD in the fit that are most sensitive to old stellar populations, and thus our ability to model the UV contribution from older star formation is limited. Including this contribution would be most likely to increase the low SFR intensity region fluxes while leaving the high SFR intensity regions unaffected.

3.4.4 Scattered Light

A portion of a galaxy's UV light can be diffuse and not associated with an obvious star-forming region. This diffuse UV emission is found between visible spiral arms or rings. In some cases, this fraction can be quite significant (up to 65% in M33; Thilker et al. 2005). There are a number of suggestions for the origination of this diffuse light, including the dispersal of B–type stars after the dissolution of their natal clusters, a low level of diffuse star formation, or the scattering by dust of UV photons produced in bright star–forming regions (Marcum et al. 2001; Crocker et al. 2015).

Some of these forms of scattered light can provide extra UV flux to the observed UV maps that is not otherwise captured by our synthetic maps. We can, however, use our modeled data to examine the extent of scattered light in M31. The right panel in Figure 3.2 shows the difference between the observed and the modeled reddened FUV flux. Blue pixels have more synthetic flux than observed with *GALEX* and red pixels have more observed flux than synthetic flux. We have predicted slightly more synthetic flux than is observed (blue pixels) in just over half of the regions. However, the regions in which we have under-predicted the flux have a larger offset than the regions in which we have over-predicted the flux, which leads to the slightly negative median ratio discussed at the beginning of Section 3.4. This excess *GALEX* flux occurs primarily along the eastern side of the 10 kpc ring as well as near two

large OB associations in Bricks 15 & 21. This discrepancy is particularly interesting because it is found near regions of very high, recent star formation. The many star-forming regions along the northeastern section of the ring are responsible for the bump in the star formation rate seen ∼50 Myr ago (Lewis et al. 2015). The excess observed flux seen near these highly star-forming regions could be an indication that some of this UV light has been scattered by dust into regions where no star formation is occurring. Further analysis of scattered light is beyond the scope of this paper.

3.5 Results

There are many different uses for the maps we have presented in this paper, including testing standard procedures for understanding the fraction of obscured star formation as well as the the applicability of common SFR prescriptions. In this section, we compare standard corrections for dust with results from the synthetic flux to better understand SFR limitations.

3.5.1 Obscured Flux and Star Formation

In Section 3.4, we presented synthetic *GALEX* maps and verified that they were in superb agreement with observations, especially in the FUV where the impact of the "2175 Å bump" is negligible. We now consider the un-reddened synthetic images ($f^{\mathrm{syn},0}$) and compare them to standard estimates of the fraction of obscured star formation.

As already discussed, the FUV is an ideal tracer of star formation because it is tied directly to emission from the youngest and brightest O and B-stars. It is also highly affected by dust. Use of the FUV as a monochromatic SFR tracer underestimates the true SFR of a galaxy. It has long been noted, though, that a correction could be made by including the flux from the longer wavelengths where dust emits. Early studies suggested using the total infrared emission

Over the past several years, it has become standard to estimate the amount of obscured star formation by "correcting" the observed emission from young stars with the observed

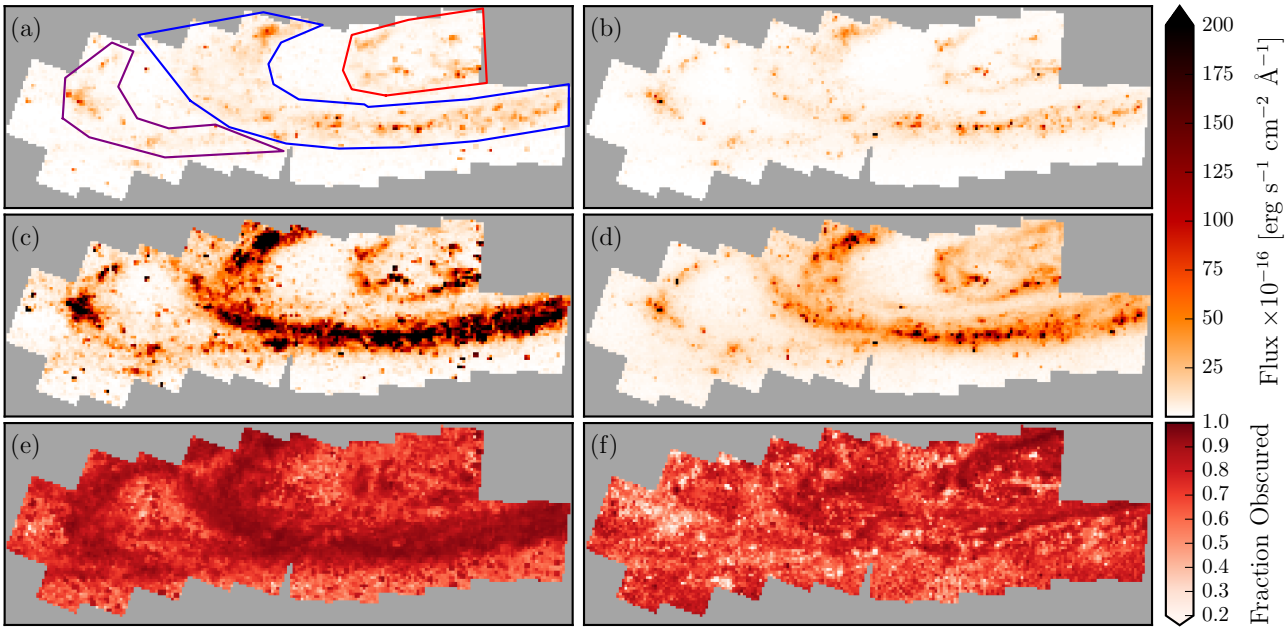

Figure 3.7 Obscured Flux and Star Formation. (a) Synthetic, reddened FUV flux: $f_{\rm FUV}^{\rm syn}$, (b) observed *GALEX* FUV flux: $f_{\rm FUV}^{\rm obs}$, (c) synthetic, un-reddened FUV flux: $f_{\rm FUV}^{\rm syn,0}$, (d) observed dust-correct flux:$f_{\rm FUV+24\mu m}$, (e) fraction of obscured flux from the synthetic maps: 1 - $f_{\rm FUV}^{\rm syn}$ / $f_{\rm FUV}^{\rm syn,0}$, (f) fraction of obscured flux from traditional observables: 1 - $f_{\rm FUV}^{\rm obs}$ / $f_{\rm FUV+24\mu m}$. Panels (a) – (d) are on the same flux scale and panels (e) and (f) are on the same scale for ease of comparison. In panel (a), we have outlined the ring features in blue (10 kpc ring), red (inner), and purple (outer). While panels (a) and (b) show remarkable agreement, the dust-corrected flux in panels (c) and (d) looks very different. In particular, the synthetic, dust-free maps indicate much more star formation in the ring and outer arm. The difference between the dust-free maps causes the fraction of obscured flux (maps (e) and (f)) to be structurally distinct. Panel (e), which uses the synthetic data, indicates that the 10-kpc ring and the 15 kpc ring feature are heavily dust obscured, while panel (f) suggests that only parts of the 10-kpc ring are obscured but that much more of the inner ring feature is enshrouded.

24μm flux from *Spitzer*. The idea is essentially one of energy balance. In a dust-free region, the total SFR could be inferred from the observed emission from young stars. In dusty regions, some of that emission is absorbed by the dust. The total flux of light that reaches the telescope is reduced and the derived SFR will be under-estimated. The dust obscures the star formation. However, the emission absorbed by the dust is not lost but rather re-emitted at different, longer wavelengths. Therefore, if we include that longer wavelength emission in our roundup of the total flux, the true SFR can be accurately derived.

Calzetti et al. (2007) first used 24 μm emission as a correction to Hα flux. They observed a correlation between the luminosity surface densities of Paα emission and 24 μm emission. Paα emission traces the ionizing photons from the photospheres of hot, young stars and is largely unaffected by dust, making it an ideal tracer of star formation in a galaxy (e.g., Kennicutt 1998). 24 μm emission traces the thermal dust emission of a galaxy originating from small dust grains (e.g., Draine & Li 2007). Calzetti et al. (2007) combined Hα emission with 24 μm emission and compared the result with the Paα emission to derive a calibration for a Hα + 24 μm SFR. Following this result, Leroy et al. (2008) derived a similar relation using FUV emission rather than Hα emission. Rather than using Paα emission for the total SFR, they estimated the scaling factor on 24 μm using various estimates of the total SFR. Similarly, in a sample of nearby galaxies, Hao et al. (2011) compared variations of UV + monochromatic infrared luminosities with IRX (total infrared to FUV luminosity ratio)-corrected FUV luminosities to derive composite SFR tracers, including a FUV + 25 μm tracer.

Dust obscuration is an extremely variable quantity. Non-active Sb-Scd galaxies typically lose about half of their bolometric luminosity to dust absorption. In early-type galaxies, this quantity drops to less than 15% Calzetti (2001). In M33, Boquien et al. (2015) found 75% of star formation in Hα, with only 25% in the infrared.

In Figure 3.7, we combine our synthetic FUV flux maps to examine the fraction of obscured star formation within the PHAT footprint and compare them with corresponding observed data from *GALEX* and *Spitzer*. In the left column, we show the synthetic maps

derived in this paper. In the top row, we plot the synthetic, reddened flux, $f_{\rm FUV}^{\rm syn}$. The middle row shows the dust-corrected flux, i.e., the synthetic, dust-free flux $f_{\rm FUV}^{\rm syn,0}$. These two maps are the same as those presented in Figure 3.2 but with a different scaling to emphasize the dust-free map. In the bottom row, we plot the fraction of obscured FUV flux using the images in the first two rows: 1 - $f_{\rm FUV}^{\rm syn}$ / $f_{\rm FUV}^{\rm syn,0}$.

The increase in total flux in the ring features immediately jumps out. Most of the star formation takes place in the 10 kpc ring (outlined in blue Lewis et al. 2015), which is also the dustiest part of the galaxy. We would therefore expect to see the most change in the flux in the ring features. The width of the ring also increases, indicating that the regions on the edges of the rings are also dusty. Overall, we find that in the synthetic dust-free data there is a factor of 8 more total flux than in the synthetic reddened data. If we look at the ring features individually, the factor difference between the total flux is 7.3, 8.2, and 7.8, for the inner, 10 kpc, and outer ring features respectively. The median factor increase for all pixels in each region is 5.6, 5.1, and 4.6, respectively.

Because M31 is a very well-studied galaxy, a lot of ancillary data exists. In addition to the *GALEX* images, we also have 24 μm images from *Spitzer*. We can therefore compare our obscured fraction analysis with estimates from other observables. We have already compared the synthetic reddened data to the *GALEX* FUV image. We can also compare the synthetic dust-free data to a derived *GALEX* FUV + *Spitzer* 24 μm image. We use the prescriptions from Hao et al. (2011) to correct the FUV image for dust:

$$L({\rm FUV})_{\rm corr} = L({\rm FUV})_{\rm obs} + 3.89 \times L(25\mu{\rm m}). \tag{3.4}$$

All luminosities have units of erg s^{-1}.

In the right column of Figure 3.7, we present corresponding maps of traditional observables of FUV + 24 μm (e.g., Hao et al. 2011; Kennicutt & Evans 2012). In the top row, we plot the observed *GALEX* flux, $f_{\rm FUV}^{\rm obs}$. The middle row shows the dust-corrected flux, i.e., the *GALEX* FUV flux corrected with 24 μm flux, $f_{\rm FUV+24\mu m}$. In the bottom row, we plot the fraction of obscured flux using the images in the first two rows. In panel (f) we use the

usual observables: 1 - $f_{\rm FUV}^{\rm obs}$ / $f_{\rm FUV+24\mu m}$. The 24 μm data comes from Gordon et al. (2006).

While the synthetic reddened and the *GALEX* maps look very good (total flux is conserved within 5%), the dust-free maps are quite different. There is a factor of 2.5 more flux in the synthetic map than in the *GALEX* + 24 μm map. Overall, we find that 88% of the flux is obscured in our synthetic maps, while 71% is obscured in the observed maps. The 24 μm correction therefore under-estimates the total FUV flux. This has a direct effect on the quantities derived from that flux, including the SFR.

We now look at the individual features of the maps. The first thing to notice is the difference in the 10 kpc ring between the two maps. If we sum up the total flux in that region, the synthetic map has a factor of 2.5 more flux than the observed map, although the median factor of the individual pixels is only 1.4. While both maps show structure within the ring, the primary difference is that the synthetic map implies that there is more flux at almost all locations. In the inner region of the galaxy, the overall structure is very similar in both maps, but the synthetic map contains a factor of 2.6 more flux, with a median of 1.86. Finally, the outer ring feature follows the same pattern. The overall structure is very similar, but the total flux is 2.4 times higher in the synthetic map with a median factor of 1.2. These differences show that in star-forming, dusty regions, the synthetic dust-free map reveals more flux than the 24 μm-corrected FUV map.

While the inter-arm regions lack the coherent structure of the ring features, the flux comparison in the synthetic and observed maps shows a similar trend. The total flux in the inter-arm regions of the synthetic map is a factor of 2.5 times higher than that in the observed map with a median value of 1.3.

The differences discussed above lead directly to the distinction in the maps of the fraction of obscured flux in the bottom row of Figure 3.7. As already discussed, the synthetic maps require a high degree of obscuration. Most of this dust occurs in the ring features, which are strong features in the obscured fraction map. However, all pixels have dust and are therefore obscured. The minimum and maximum obscuration in the synthetic maps is 19% and 97%, respectively.

There is much less structure in the observed obscured fraction map. In this map, the most obscured regions are towards the center of the galaxy. The 10 kpc ring and outer ring feature are less apparent while the inner ring feature is stronger. Additionally, the inner edge of each ring feature is more obscured than the feature itself; i.e., it is still possible to pick out the 10 kpc ring in the observed obscured fraction map, though only at one edge. Finally, we note that the bright star-forming region in B21 (the bright feature at left edge of panel c) has very little obscuration in the observed data suggesting that the stars in this region are old enough to have dispersed their natal cloud but have not yet reached more evolved, dusty stages. Our results show that the 24 μm correction for dust does not work well in regions of low star formation intensity which are likely dominated by older stellar populations.

3.5.2 SFR Measurements

The discrepancy between the synthetic dust-free flux map and the FUV + 24 μm flux map indicates that the overall SFR will also be affected. The usual method of converting a FUV flux into a SFR is to apply an extinction correction to the observed flux, convert the flux to luminosity, and then calculate a SFR according to a standard calibration. A common calibration is that from Kennicutt (1998) with updates by Hao et al. (2011) and Murphy et al. (2011):

$$\mathrm{SFR} = 10^{-43.35} \times L_{\mathrm{FUV}}. \tag{3.5}$$

where L_{FUV} is the dust-corrected FUV luminosity with units of erg s^{-1} and the resulting SFR has units of $\mathrm{M}_{\odot}\,\mathrm{yr}^{-1}$.

There are a variety of methods for correcting the data for dust. As mentioned in Section 3.5.1, using some constant times the 24 μm flux is a popular method, especially in relatively nearby galaxies where high quality *Spitzer* 24 μm data exists. Another method is to use UV color ($m_{\mathrm{FUV}} - m_{\mathrm{NUV}}$) to correct the FUV magnitude which is then converted to flux for further conversion to SFR. This method is often used at high redshift.

We use the calibrations from Hao et al. (2011). The correction using 24 μm data is shown

in Equation 3.4. The UV color correction is:

$$A_{\rm FUV} = \\ (3.83\pm0.48)[({\rm FUV}-{\rm NUV})_{\rm obs} - (0.022 \pm 0.024)]. \tag{3.6}$$

In Figure 3.8, we examine the relationship between the SFR averaged over the last 100 Myr as calculated from the CMD-derived SFH (Lewis et al. 2015) and that derived from FUV flux corrected for extinction with the 24 μm or UV color calibrations described above. In each panel, we plot the CMD-derived SFR ($\rm SFR_{CMD}$) on the x-axis. The top panels show the flux-to-flux relationship. In the bottom panels, we plot the ratio of the flux-based SFR to the cmd-based SFR ($\rm SFR_{flux}/SFR_{CMD}$) on the y-axis. In each panel, the black dashed line represents one-to-one agreement. In the top panels, the black star marks the flux-weighted mean along each axis. In the bottom panels, we have plotted the running median and standard deviation in blue.

In the left panels, we show the flux-based SFR ($\rm SFR_{flux}$) derived after using the 24 μm prescription to correct for extinction. In the right panels, we show the flux-based SFR calculated from FUV flux corrected for dust with the UV color calibration.

We first look at the left panels. On the top we plot the SFR derived from the 24 μm-corrected FUV flux against the CMD-derived SFR averaged over the most recent 100 Myr. The overall morphology of the data is ok using the 24 μm correction. There is a clear trend in the data that $\rm SFR_{flux,24\mu m}$ increases as $\rm SFR_{CMD}$ increases, as is expected. The flattening in $\rm SFR_{flux,24\mu m}$ occurs at $\rm SFR_{CMD} < \sim 10^{-6}$ which corresponds approximately to the limit at which the flux calibrations are no longer reliable, especially on these spatial scales (e.g., Murphy et al. 2011; Leroy et al. 2012; Kennicutt & Evans 2012). This results in an over-estimate of the SFR at low $\rm SFR_{CMD}$ and an under-estimate at high $\rm SFR_{CMD}$. This trend is seen more clearly in the bottom left panel, where we plot the log of the ratio between $\rm SFR_{flux,24\mu m}$ and $\rm SFR_{CMD}$. The over-estimate of $\rm SFR_{flux,24\mu m}$ increases as $\rm SFR_{CMD}$ decreases. At higher $\rm SFR_{CMD}$, the ratio starts to flatten though offset from the one-to-one line.

While the overall morphology of the relationship between $\rm SFR_{flux}$ and $\rm SFR_{CMD}$ is good,

the flux-weighted mean, marked by the black star in the top left panel, is offset. We find that the mean flux-based SFR is 0.39 dex lower than the mean CMD-based SFR. The 24 μm-corrected FUV flux will therefore under-estimate the SFR by a factor of $\sim$2.4.

The right panels in Figure 3.8 show the comparison between $\mathrm{SFR_{CMD}}$ and $\mathrm{SFR_{flux,FUV\text{-}NUV}}$. The results are very different from the 24 μm correction. When using UV color, the morphology of the relationship is completely wrong. On a region-to-region basis, there is zero correlation between $\mathrm{SFR_{CMD}}$ and $\mathrm{SFR_{flux,FUV\text{-}NUV}}$. Any $\mathrm{SFR_{CMD}}$ can map to a two order of magnitude range in $\mathrm{SFR_{flux,FUV\text{-}NUV}}$. The only trend that exists is that the UV color correction results in an over-estimate of $\mathrm{SFR_{flux,FUV\text{-}NUV}}$ at low $\mathrm{SFR_{CMD}}$ and an under-estimate at high $\mathrm{SFR_{CMD}}$.

Despite the absence of region-to-region correlation, the flux-weighted mean SFR falls directly on the one-to-one line. In unresolved regimes where spatial information is very coarse or unavailable and measurements are limited to single points for an entire galaxy, such as in the high-redshift regime, the UV color correction will provide a good overall estimate of the SFR.

We note that we could have used the synthetic, dust-free FUV flux-derived SFR on the x-axis instead of the 100 Myr averaged SFR from the CMD-derived SFHs. The results would be the same with an offset of the mean flux-weighted SFRs from the one-to-one line when using the 24 μm correction and a lack of correlation when using the UV color correction.

3.6 Discussion

We have shown that the conversion of FUV flux into a SFR after correcting for dust with two different prescriptions results in vastly different relations when compared with the SFR determined from the CMD-derived SFH (or alternatively from using Equation 3.5 on the dust-free synthetic FUV flux, $f_{\mathrm{FUV}}^{\mathrm{syn},0}$). These differences are perhaps not surprising, but they do beg the question of what drives the discrepancies. At the most basic level, the discrepancy arises either from the modeled data (synthetic flux or CMD-based SFR) or from the SFR calibrations in the literature.

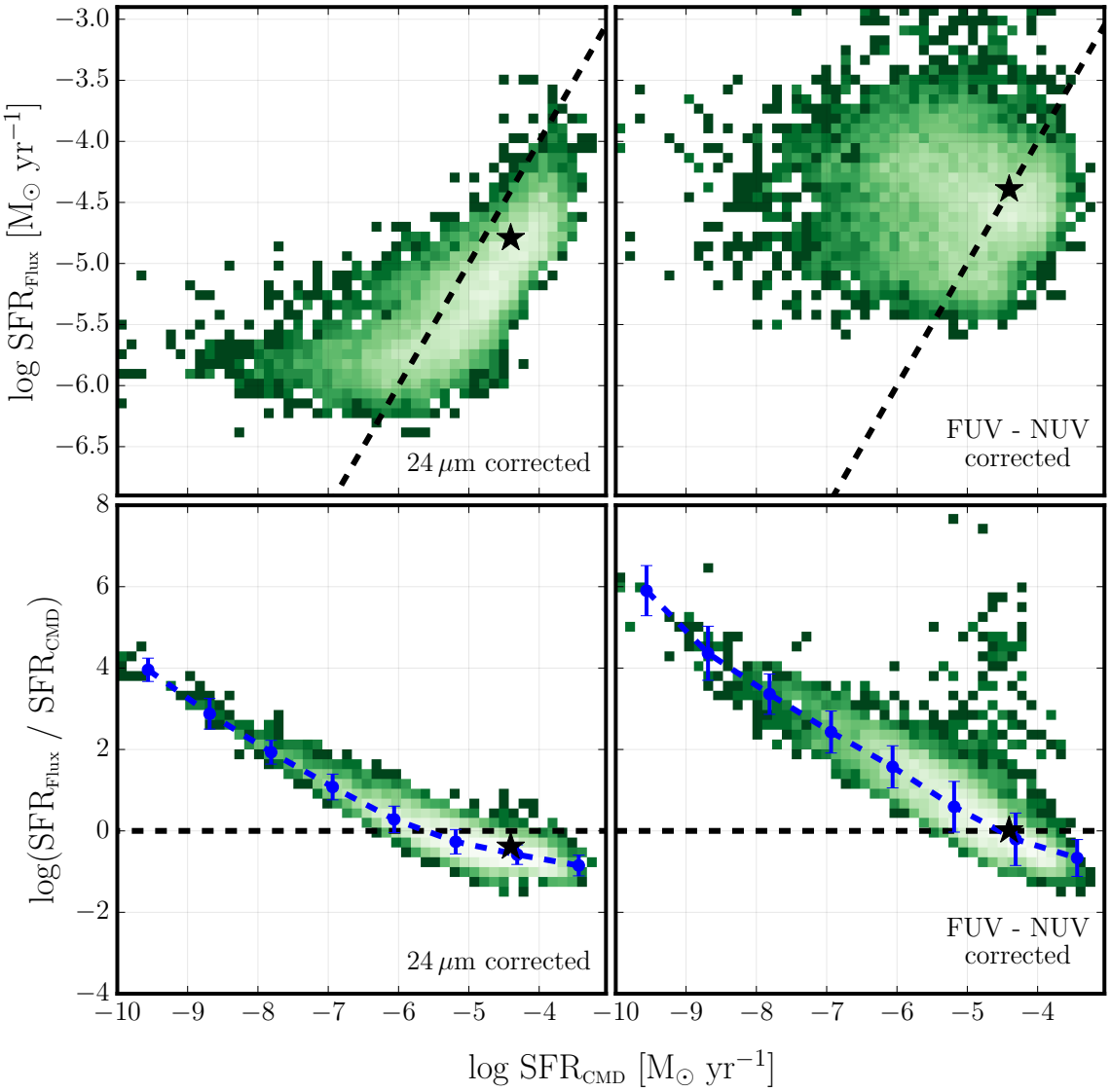

Figure 3.8 Comparison between CMD-based and flux-based SFRs. In all panels, the x-axis is the SFR from the CMD-derived SFHs, averaged over the last 100 Myr ($\langle \mathrm{SFR} \rangle_{100}$). In the top left panel, the y-axis shows the flux-based SFR derived from the FUV + 24 μm combination. The top right panel is corrected for dust using FUV–NUV color. The bottom panels show the ratio of the flux-based SFR to the CMD-based SFR. In each panel, the black star marks the flux-weighted mean along each axis, and the black dashed line denotes one-to-one agreement.

As discussed in Lewis et al. (2015) and Section 3.4.2, there are a variety of factors that affect the CMD-derived SFHs and the synthetic flux. The primary uncertainties come from the chosen dust parameters and uncertainties in the SFHs, which were only of order 10% over a 100 Myr timescale. We also showed in Section 3.4 and Figure 3.4 that the synthetic, reddened flux is in very good agreement with the observed *GALEX* FUV flux. This suggests that the dust parameters derived from the SFHs are reasonable and therefore the SFR derived from the CMD-derived SFHs is not driving the discrepancy.

The inconsistencies must therefore lie with the flux calibrations. This should not be a surprising conclusion. The vast majority of SFR prescriptions are designed for regions containing at least tens of thousands of stars, such as entire galaxies or bright, star-forming regions. They make assumptions about the shape of the SFH, usually assuming a constant SFR over some timescale. They assume that the IMF in the given region is completely sampled. They assume that the region is homogenous, i.e., stellar populations are completely mixed and they are insensitive to structure in the dust, gas, and stars. Additionally, they often use only a single metallicity (usually) solar, and they are insensitive to metallicity evolution.

Most objects in the universe fall into the unresolved regime where the above assumptions are generally safe. This is especially true in the high redshift universe. In this regime, the UV color correction is commonly used to correct the SFR for dust. While Figure 3.8 suggests that this correction is terrible in the spatially-resolved regime, the fact that the flux-averaged mean SFRs are in agreement suggests that it may be a reasonable choice in the unresolved regime, especially when the availability of data at IR wavelengths is limited.

In the local Universe,the existing calibrations seem to work on large (>1 kpc) scales, which is the scale at which they were calibrated. However, we showed in this paper that even the flux-weighted means over the entire galaxy are off when using the 24 μm correction. However, even on these scales, many of the above assumptions are not applicable. Nearby galaxies show highly-defined structure in spiral arms and rings, in dust lanes, and in populations of molecular clouds and other gaseous objects. This structure varies in population; spiral

arms are populated by young and blue, main sequence stars. The centers of galaxies tend to contain older, more redder populations. Additionally, as structure within a galaxy is resolved, variations in stellar environment become apparent. Regions of high and low star formation, of varying metallicity, and of changing stellar density are revealed. Finally, the shape of the SFH is important, especially when correcting for dust (e.g., Boquien et al. 2016). The assumptions made when averaging over entire galaxies can no longer be made on smaller, variable scales. In fact, making such assumptions will bias the results. Nonetheless, we still want to determine SFRs for these galaxies and on these scales to take advantage of the increased spatial resolution.

We note that we have chosen to use a single prescription for each method of correcting FUV flux for dust. However, many studies have examined hybrid SFR tracers in an effort to determine the best combination of the data. Specifically looking at the FUV + 24 μm combination, the uncertainty primarily lies on the weight applied to the 24 μm data, w_{24}. In this paper, we use the Hao et al. (2011) factor of 3.89. In an earlier study, Zhu et al. (2008) found w_{24}=6.31. More recently, Boquien et al. (2016) calculated w_{24} (they call it k_i and examine other infrared tracers long-ward of 24 μm as well) in 8 different galaxies and found a wide distribution ranging from 1.55 to 13.45 with a mean of 8.11. They stress that this factor has important galaxy-to-galaxy variations, as well as local vs. global variations that should not be overlooked. Uncertainty in this factor is is clearly an issue in this study as well. Had we used the Boquien et al. (2016) value of 8.11 in this paper, we would have found much better agreement between the flux-based SFR and the CMD-based SFR.

Boquien et al. (2016) actually present two different parameterizations of their factor k_i based on FUV-NIR color and on NIR luminosity density. These parameterizations allow k_i to vary from galaxy-to-galaxy. Testing and analysis of these parameterizations is beyond the scope of this paper. However, as higher spatial resolution becomes available beyond the most nearby galaxies, such methods for reliably determining the SFR while accounting for galaxy-to-galaxy variation are needed.

3.7 Conclusions

We have used spatially-resolved SFHs derived from optical resolved star data to model the SEDs of over 9000 sub-kpc regions in M31 and produce detailed maps of synthetic reddened and dust-free UV flux across the entire area covered by the PHAT survey. The SFHs were derived by Lewis et al. (2015) using F475W and F814W photometry from the PHAT survey. Both intrinsic and attenuated SEDs were derived from the SFHs using FSPS. These SEDs were convolved with the *GALEX* FUV and NUV response curves to generate synthetic fluxes, $f^{\rm syn}$. All of the flux values were then assembled into an overall map using Montage. The pixels correspond to physical areas of $4.4 \times 10^4\,{\rm pc}^2$.

We also used Montage to construct maps of the observed UV flux, $f^{\rm obs}$, using *GALEX* DIS images and 24 μm (Gordon et al. 2006), as well as $\langle {\rm SFR} \rangle_{100}$ from the spatially-resolved SFHs, all on the same spatial scale.

The agreement between the observed flux maps and the reddened modeled flux maps is encouraging, especially given that they were derived from only photometry in two optical bands. They indicate that models of UV emission and dust extinction are fairly accurate. The median log ratio of the synthetic reddened flux to the observed flux is 0.005 and -0.027 in the FUV and NUV, respectively, with standard deviations of 0.24 in the FUV and 0.16 in the NUV. This agreement confirms the robustness of our modeling procedure and justifies the assumptions made in the modeling routine.

The scatter in the relation between observed *GALEX* flux and synthetic, reddened flux is primarily due to uncertainties on the SFHs used in the modeling process. These uncertainties include a factor due to incomplete sampling of the IMF.

We compared our synthetic reddened and dust-free FUV flux maps with corresponding maps from observations. The synthetic reddened map was compared to the observed *GALEX* FUV map. The dust-free map was compared to map derived from a combination of FUV + 24 μm data. In the synthetic FUV flux maps, 88% of the flux is obscured by dust. In the observed maps, 71% is obscured. This suggests that the 24 μm correction results in an

under-estimate of the total FUV flux.

We converted the observed flux map into a map of SFR using two common prescriptions, one using 24 μm to correct for dust and the other using UV color. We compared the resulting SFRs with those determined from the Lewis et al. (2015) SFHs averaged over the past 100 Myr. While the morphology of the relation between the CMD-derived SFR and that calculated using the 24 μm correction was good, the *GALEX* + 24 μm-derived SFR was under-estimated by a factor of 2.5. Conversely, the UV-color correction resulted in a flux-weighted mean SFR in good agreement with that derived from the CMDs, but the relation shows no correlation between the two SFRs as would be expected.

The results we present in this paper provide an end-to-end verification of the SFH results presented in Lewis et al. (2015) and show that we have the ability to model flux in a variety of bandpasses given optical data and appropriate assumptions for the stellar IMF, a set of models describing stellar spectra and evolution, and an extinction model. While modeling flux in other bands provides different challenges, the technique is extremely promising.

3.8 Supplementary Analysis: The Effects of Old Stellar Populations on Synthetic and Observed Flux

Throughout the main body of this paper, we analyzed synthetic and observed FUV, NUV, and 24 μm flux without regard to the stellar populations emitting at each wavelength. We used the entire SFH – from the present day to 14 Gyr ago – in the modeling routine (Section 3.3.1, despite the warning that the Lewis et al. (2015) SFHs are robust only to 500 Myr ago. We did this in order to accurately compared the modeled UV flux with the total observed *GALEX* flux. Approximately 20-30% of the emission at FUV and NUV wavelengths comes from stars that are older than 100 to 300 Myr and are thought to produce most of the UV light flux.

We must include these older populations to accurately model the UV flux. We could have made an assumption about the form of the SFH beyond 500 Myr (constant, declining tau, etc.); however, we decided to use the full SFHs derived from the CMD analysis. We

note that while the SFH solution was optimized for the most recent 500 Myr, it still has information at older ages. Using this total SFH will be more robust than using an assumed form.

3.8.1 Modeled-to-Observed Flux Comparison

We account for these older populations in both the synthetic and the observed data. In Figure 3.9, we examine the effect of older stellar populations on the synthetic flux. We plot the ratio of the synthetic flux to the observed flux as a function of the observed flux (as in Figure 3.4). In each panel, we have modeled the FUV flux with a different age limit applied to the SFH. The top left panel uses the full SFH and is identical to the top panel in Figure 3.4. In the next panel we model the flux using the SFH back to 5 Gyr ago. The bottom left panel applies a cut to the SFH at 500 Myr ago, which is the limit specified in Lewis et al. (2015). The bottom right panel uses SFR data from just the most recent 100 Myr. In each panel, we have indicated the age limit in the top right corner. Below that is the ratio of the sum of the synthetic flux to the sum of the observed flux. The red circles and error bars show the running median and standard deviation.

The effect of reducing the age information in the flux modeling routine is clear. As the information from older populations is removed, the total synthetic flux drops, as expected. This decrease is generally seen in the low flux regions. The total synthetic flux decreases by $\sim$20% as the age information is cut from 14 Gyr to 100 yr. This is in line with literature values of the amount of UV flux expected from older populations (e.g., Johnson et al. 2013). We note, however, that in all panels and all flux bins, the log of the ratios ratios are consistent with zero to within 1σ.

We perform the same exercise in the NUV and plot the results in Figure 3.10. The general results are similar to those in the FUV except the decrease in flux is much more substantial in the NUV, especially at the low-flux end. As mentioned in our discussion of Figure 3.4, the NUV is much more sensitive to the shape of the extinction curve, primarily at the high-flux end. This sensitivity likely contributes to the under-production of synthetic flux seen in the

top left panel when the full SFH is used and propagated through as the synthetic flux relies more strongly on younger populations that may be more affected by the 2175Å bump.

The observed data is also affected by emission from older stellar populations (e.g., Kennicutt et al. 2009). A few corrections exist in the literature. One such method is to use 3.6 μm flux to correct for older populations. Some fraction of the 3.6 micron data, $\alpha_{3.6,\mathrm{FUV}}$, is subtracted from the FUV data:

$$I_{\mathrm{FUV,young}} = I_{\mathrm{FUV,all}} - \alpha_{3.6,\mathrm{FUV}} \times I_{3.6\mu\mathrm{m}} \tag{3.7}$$

leaving the FUV intensity from young stars. The general idea is that older stars tend to be faint at bluer wavelengths but will emit more strongly in the infrared. Leroy et al. (2008) looked at the ratio of FUV to 3.6 μm SFR intensities in their sample of nearby galaxies and found $\alpha_{3.6,\mathrm{FUV}} \sim 2 - 4 \times 10^{-3}$. However, Ford et al. (2013) performed the same exercise in M31 and found $\alpha_{3.6,\mathrm{FUV}} \sim 8 \times 10^{-4}$. Here we use the Ford et al. (2013) value derived for M31.

We apply this correction to the observed FUV flux and we plot the resulting flux ratios in Figure 3.11. We have also included the same age limit cuts to the synthetic flux as we showed in Figure 3.9. The correction to the observed flux increases the flux ratios, especially at the low-flux end, as would be expected. As the age limit on the synthetic flux decreases, the correction to the observed flux has less of an impact. In all panels and all flux bins (except for the brightest bin), the synthetic and observed fluxes are in agreement within 1σ. There is no corresponding correction in the literature for the contribution of older populations to the NUV flux.

3.8.2 SFR Comparison

In this section, we examine how the effects of older stellar populations on the observed flux translate to changes in the derived SFR. In the previous section, we corrected the observed FUV flux for older stellar populations by using data at 3.6 μm. We can do the same thing with our 24 μm data:

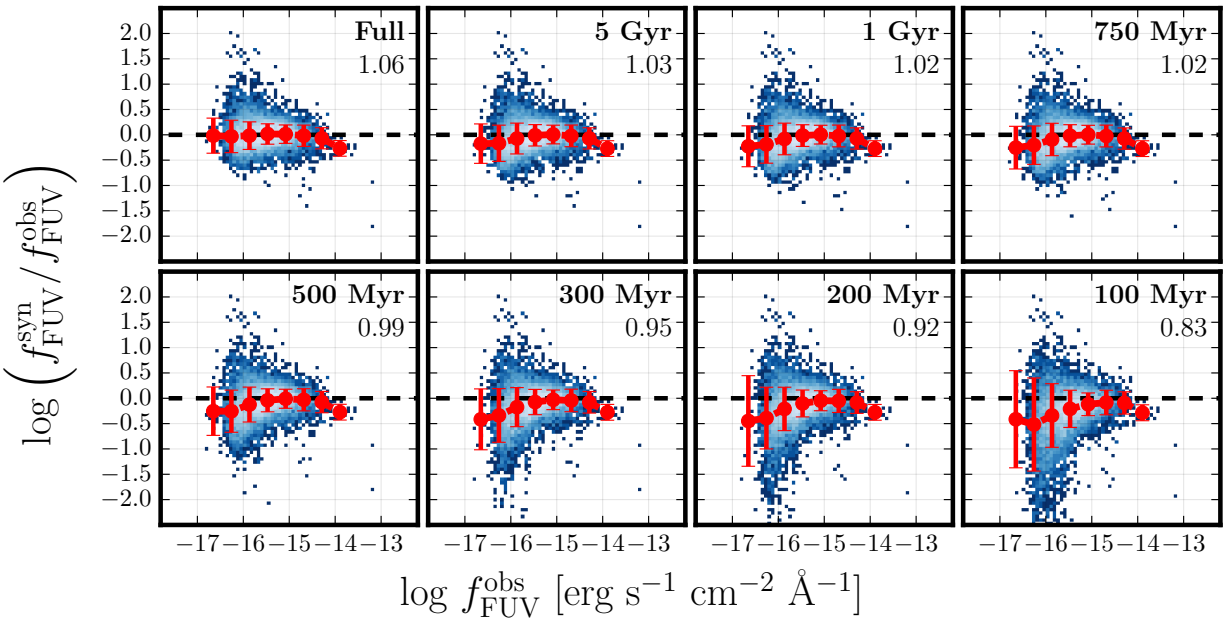

Figure 3.9 The log ratio of the synthetic, reddened FUV flux to the observed *GALEX* FUV flux as a function of observed flux with a variety of age cuts on the SFH. The red circles in each panel show the running median with the standard deviation given by the error bars on each point. The age cut used is listed in the top right corner of each panel. The fraction of total synthetic flux to total observed flux is listed just below the age cut.

$$I_{24,\mathrm{young}} = I_{24,\mathrm{all}} - \alpha_{3.6,24} \times I_{3.6\mu\mathrm{m}} \tag{3.8}$$

Leroy et al. (2008) found $\alpha_{3.6,24} \sim 0.1$ in their sample of galaxies. In their study of M31, Ford et al. (2013) also found $\alpha_{3.6,24} = 0.1$, so we use that value here.

We corrected both the *GALEX* FUV and the *Spitzer* 24 μm data for contributions from older stellar populations and recalculated the SFRs. We plot the resulting SFRs compared with those derived from the CMD-derived SFH in Figure 3.12. This figure can be directly compared to Figure 3.8 which does not include the old star correction.

Including the correction for older stars worsens the agreement between the observed and

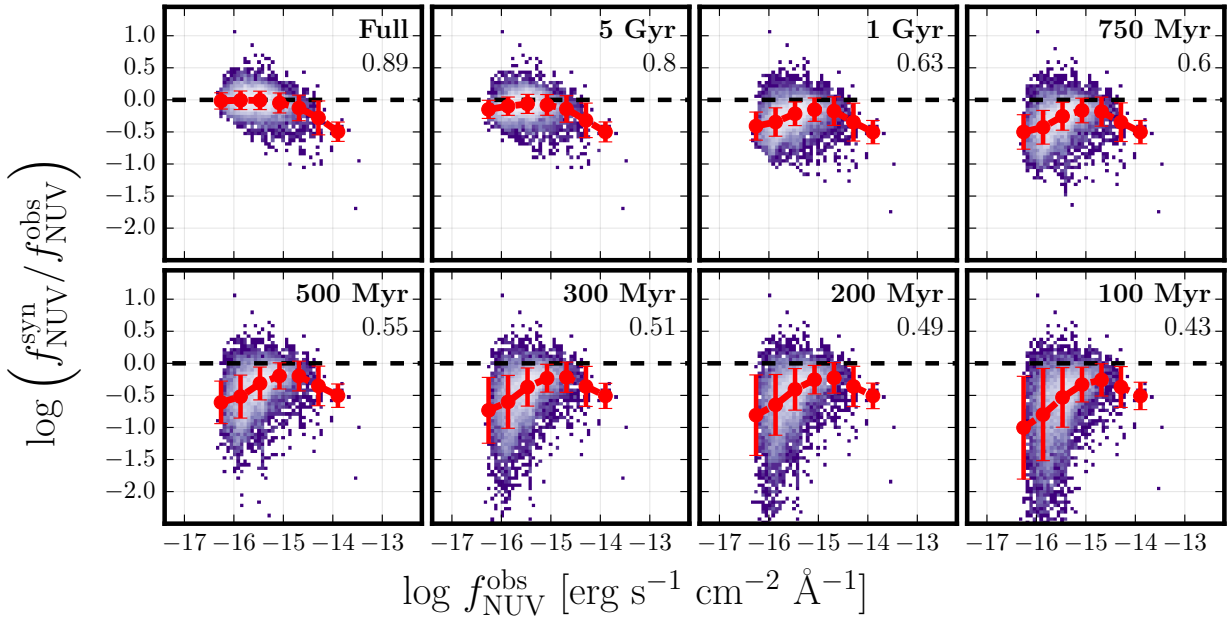

Figure 3.10 The same as Figure 3.9 except for the NUV.

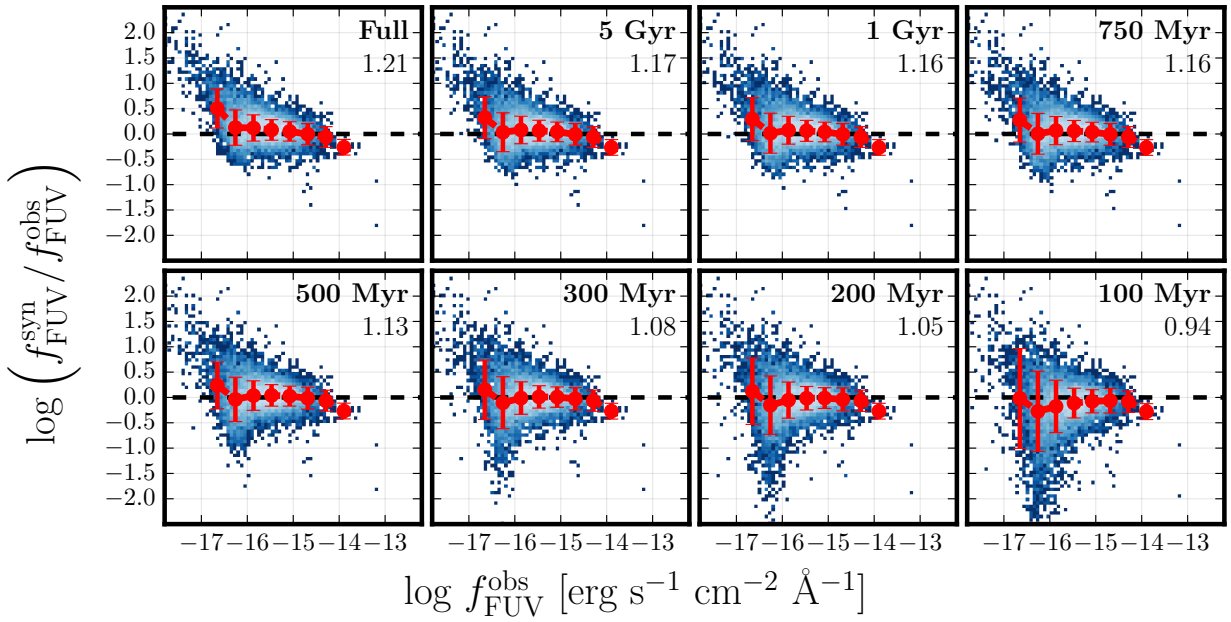

Figure 3.11 The same as Figure 3.9 except that we also include a correction for older populations in the observed flux.

CMD-based SFRs. In Figure 3.12, the x-axis remains unchanged from that in Figure 3.8 because it is taken directly from the most recent 100 Myr of the CMD-derived SFHs. No correction for old stars is necessary. In the left panels, the values on the y-axis decrease because there is generally less FUV flux. The overall morphology remains the same between Figures 3.12 and 3.8; however, the mean values of the flux and CMD-based SFRs now differ by 0.46 dex (a factor of 2.9), up from 0.39 dex (a factor of 2.4).

In the right panels of Figure 3.12, we show the UV color-derived SFR. While the flux-weighted means along the two axes are still in agreement, there is no overall correlation between the two SFRs on small spatial scales, as seen in in Figure 3.8. We cannot, however, draw any conclusions from the right panels because the NUV data have not been corrected for the contribution from older stellar populations.

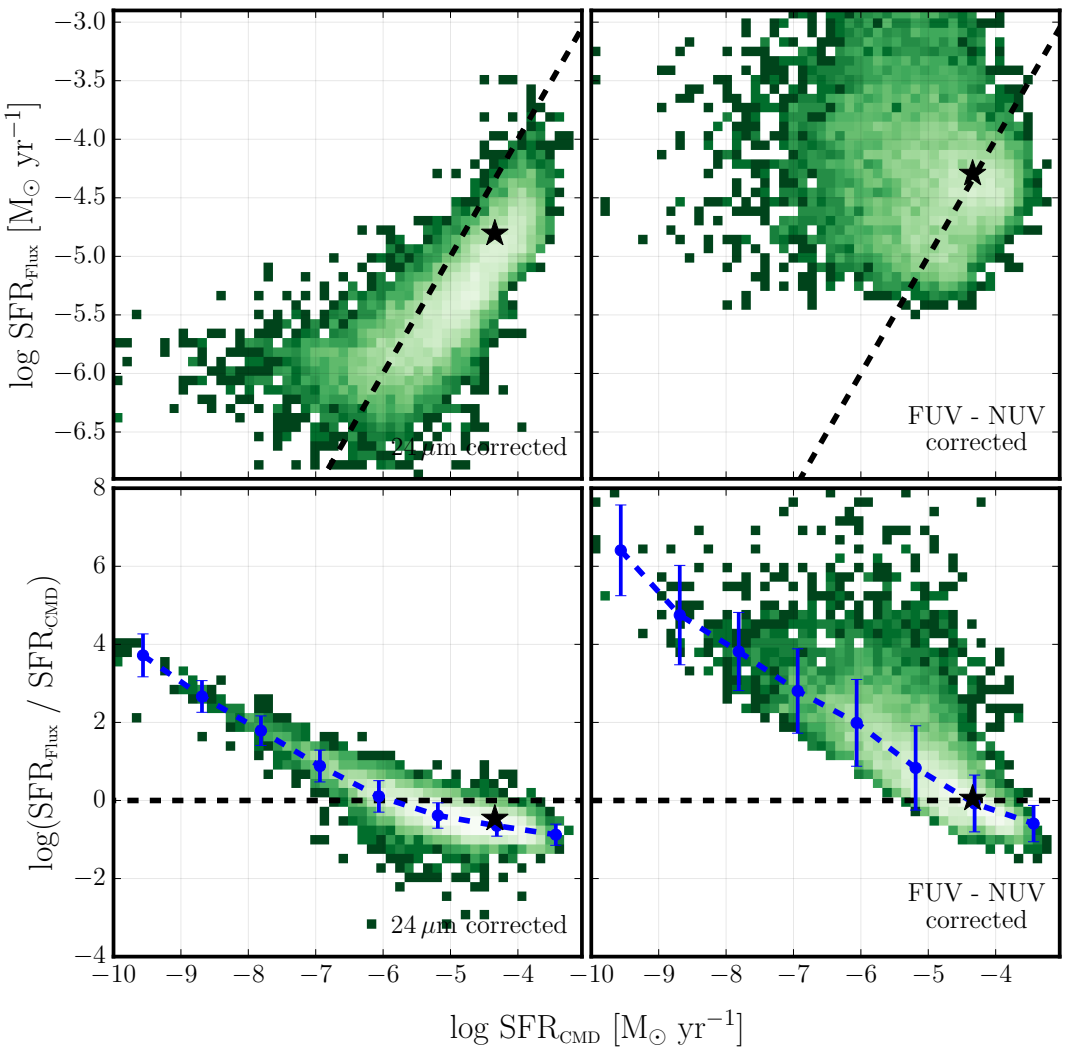

Figure 3.12 Comparison between CMD-based and flux-based SFRs. This is the same as Figure 3.8 except that we have corrected the observed FUV and 24 μm fluxes for the contribution from older stellar populations. In all panels, the x-axis is the SFR from the CMD-derived SFHs, averaged over the last 100 Myr ($\langle {\rm SFR} \rangle_{100}$). In the top left panel, the y-axis shows the flux-based SFR derived from the FUV + 24 μm combination. The top right panel is corrected for dust using FUV–NUV color. The bottom panels show the ratio of the flux-based SFR to the CMD-based SFR. In each panel, the black star marks the flux-weighted mean along each axis, and the black dashed line denotes one-to-one agreement.

Chapter 4

VARIATIONS IN THE DUST LAW ACROSS THE DISK OF M31

We infer the ultraviolet (UV) shape of M31's dust attenuation curve using 100 pc size regions across 1/3 of M31's star-forming disk. We derive the extinction curve that reproduces the observed *GALEX* images when applied to to synthetic, dust-free UV images derived from optical CMD-based, spatially-resolved SFHs. We fit for an attenuation curve model that includes both variable slope, R_V, and variable strength of the 2175 Å bump relative to that of the Milky Way (MW), parameterized as $f_{\rm bump}$. We find that the individual 100 pc regions provide good constraints in R_V, while the constraints on $f_{\rm bump}$ are mostly unconstrained on small scales. We derive global values of R_V and $f_{\rm bump}$ by modeling the ensemble of region results. We find that values of R_V are distributed with a mean of $\mu_{R_V} = 2.94 \pm 0.01$ and a width of $\sigma_{R_V} = 0.71 \pm 0.01$. The bump strength, $f_{\rm bump}$, distribution has a mean of $\mu_{f_{\rm bump}} = 0.68 \pm 0.01$ and a width of $\sigma_{f_{\rm bump}} = 0.19 \pm 0.01$. The mean R_V is somewhat smaller than the canonical MW value ($R_V = 3.1$), which corresponds to a more than 15σ deviation. The MW value can, however, be drawn from the M31 distribution with high probability. The 2175 Å bump feature is weaker than that of the MW, with agreement seen within 2σ. We create maps of the median R_V and $f_{\rm bump}$ values in each region across the survey area. The R_V map shows considerable variation from the inner regions to the 10-kpc ring, and from star-forming to quiescent regions.

4.1 Introduction

The presence of dust in galaxies has wide-ranging effects on most areas of astronomy. It causes stars to appear redder and fainter than they actually are, obscures the process of star

formation, and reprocesses light from the ultraviolet (UV) and optical into the mid- and far-infrared (IR). The net result is that dust substantially alters a galaxy's spectral energy distribution (SED), with the largest impacts seen in the UV.

Given these effects, interpreting extragalactic phenomena requires characterizing the properties of dust. These include efforts to understand the physical properties of dust, including its composition, grain size, formation and destruction, as well as its emissivity (see Draine 2003, and references therein).

Among the most useful ways to characterize dust is through its "attenuation curve", the amount of light removed by dust at each wavelength A_λ (often normalized to the attenuation in the optical V band, A_V). The resulting curve is shaped by the effects of both extinction and scattering, and thus is sensitive to the exact composition and geometry of the dust. As a result, the attenuation curve can vary with environment, depending on the properties of the population of dust grains (e.g., Kim et al. 1994; Weingartner & Draine 2001; Zubko et al. 2004; Seon & Draine 2016). Such variations have been seen both within the Milky Way (MW; e.g., Cardelli et al. 1989; Larson & Whittet 2005) and in other galaxies (e.g., Roussel et al. 2005; Clayton et al. 2015).

The typical way to determine the properties of an attenuation curve is through the "pair method" (e.g., Massa et al. 1983; Fitzpatrick & Massa 1986). The pair method compares the spectra of two stars of similar spectral type, one reddened and the other un-reddened (or only slightly reddened). Historically, studies that used this method only analyzed small samples along a limited number of lines-of-sight, due to the inability to find the necessary un-reddened stars.

When the attenuation curve is determined using stellar spectra, the interpretation is that the dust removes photons from the line-of-sight, either by absorbing the photons or by scattering them away. When this method is applied to extended objects, however, the interpretation is more complicated because dust can scatter light into the line-of-sight. The geometry and the properties of the dust both become important when measuring its effect on galaxies (e.g., Calzetti et al. 1994; Johnson et al. 2007; Wild et al. 2011; Battisti et al.

2016).

Attenuation curves are typically parameterized by just one or two variables. One of the most common parameterizations is by Cardelli et al. (1989). This attenuation law is a series of curves that are differentiated according to the slope of the curve, R_V. This widely used parameter is a measure of the total to selective extinction, or the slope of the extinction curve. Larger values of R_V indicate a flatter extinction curve, which is thought to be due to the presence of larger dust grains, which absorb and scatter light at longer wavelengths. Smaller values of R_V indicate a steeper extinction curve and smaller dust grains, which affect the shorter, UV wavelengths.

The second feature that is known to vary among attenuation curves is the 2175 Å bump, a region of additional attenuation in the extinction curve. It is very prominent feature in the MW's extinction curve but weak or non-existent in starburst galaxies (e.g., Cardelli et al. 1989; Calzetti et al. 1994, 2000; Battisti et al. 2016). There is also evidence of correlation between the strength of the bump feature and R_V, with larger R_V regions showing weaker bumps, and smaller R_V regions showing stronger bumps (e.g., Fitzpatrick & Massa 2007). Additional studies have found a correlation between specific SFR and bump strength, with higher specific SFRs having weaker bumps (e.g., Wild et al. 2011; Buat et al. 2012). This variation in bump strength is often characterized with a second parameter, $f_{\rm bump}$ (e.g., Fitzpatrick & Massa 1986; Conroy et al. 2010).

Given the variability of dust within the MW, it is also important to look at the attenuation properties of other galaxies both to place the MW's dust in context and to better understand the physics of dust populations. Additionally, observations in external galaxies must be corrected for dust for proper interpretation. Galaxies in the local universe are the easiest to study due to their proximity, which enables the application of techniques developed to study the MW. As a result, the Magellanic Clouds are the most extensively studied(e.g., Prevot et al. 1984; Fitzpatrick 1986; Pei 1992), with a handful of studies in M31 (e.g., Bianchi et al. 1996; Dong et al. 2014).

Beyond the most nearby galaxies, methods that do not require the resolution of individual

stars are required. Calzetti et al. (1994) studied the dust extinction properties in a sample of star-forming galaxies and found that they did not agree with either MW or LMC dust laws. Their derived dust law lacked a 2175 Å bump feature. The Calzetti et al. (1994) curve is often applied to high redshift galaxies. Battisti et al. (2016) carried out a follow-up study on a much larger sample of nearby ($z < 0.1$), star-forming galaxies with the same conclusion. In a similar sample of low-z ($z < 0.05$) star-forming galaxies, Conroy et al. (2010) also found that the traditional Cardelli curve did not fit the data well. However, they concluded that the trends seen in the galaxy colors must be due to a 2175 Å bump feature with a strength 80% that of the MW.

Given the abundant variety of stellar and gaseous environments found within an $L_\star$ galaxy like M31, there is no obvious reason why the attenuation curve should be constant across the galaxy. Indeed, two recent studies suggest that the optical-infrared extinction curve varies throughout the MW (Nataf et al. 2016; Schlafly et al. 2016). Our spatially-resolved SFHs provide an excellent dataset with which to examine variations in the attenuation curve in M31.

In this paper we probe the properties of the attenuation curve in a different way. We compare the UV flux predicted from the Lewis et al. (2015) SFHs to the observed *GALEX* flux across the face of M31 in $24'' \times 27''$regions. We fit for the global best-fit values of R_V and $f_{\rm bump}$ and map the spatial variation of R_V across the disk. The flux modeling process gives us the ability to predict the intrinsic flux without making any assumptions about the shape of the reddening curve.

This paper is organized as follows. In Section 4.2, we describe the data we use to perform this analysis. We then proceed to a description of the process used to fit for the attenuation curve parameters in Section 4.3, both region-by-region and as an ensemble. We present our results in Section 4.4 and discuss them in Section 4.5. A summary of our results is given in Section 4.6.

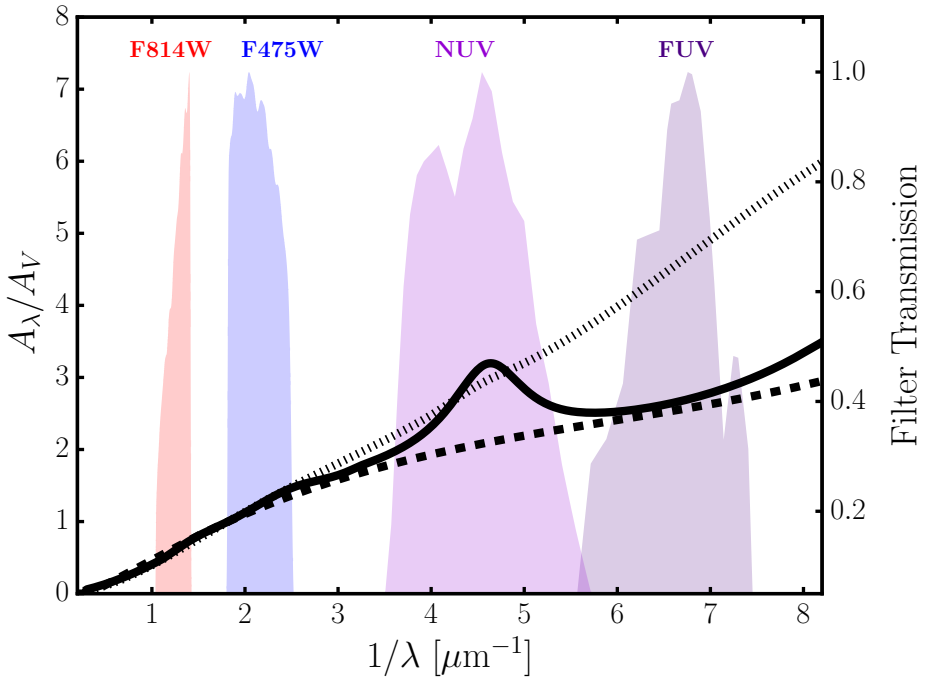

Figure 4.1 Dust laws and transmission curves for the filters used in this study. The solid black line is a Cardelli et al. (1989) extinction curve. The dashed black line is a Calzetti et al. (2000) curve. The black dotted line is a Pei (1992) SMC attenuation curve. We have over-plotted the transmission curves for the filters used in this study. At optical wavelengths, the dust curves are indistinguishable; as such, the specific dust parameters assumed in Lewis et al. (2015) have no significant effect on the SFH modeling.

4.2 Data

The data products used in this paper were created and described in Lewis et al. (2016). We briefly describe them here but we refer the reader to the original paper for further details.

4.2.1 Observed UV Flux

We take UV imaging data from the *GALEX* Deep Imaging Survey (DIS; Martin et al. 2005), using the five tiles that cover the PHAT survey in the FUV and NUV. We converted the

count rate units, *cps*, into flux according to

$$f = U \left(\frac{\mathrm{cps}}{\mathrm{counts\,s^{-1}\,pixel^{-1}}} \right) , \tag{4.1}$$

We subtracted off a background flux of 2.96×10^{-16} erg s^{-1} cm^{-2} Å^{-1} in the FUV and 2.60×10^{-16} erg s^{-1} cm^{-2} Å^{-1} in the NUV, calculated from the median flux in four, off-galaxy regions and then making a 10 – 40% adjustment to guarantee positive flux across M31. This adjustment primarily affects the regions with the smallest UV flux and therefore does not significantly affect our results. We refer to the observed, *GALEX* flux as $f_{\mathrm{FUV}}^{\mathrm{obs}}$ and $f_{\mathrm{NUV}}^{\mathrm{obs}}$ in the FUV and NUV, respectively.

4.2.2 Modeled Dust-free UV Flux

To compare to the *GALEX* observations, we construct synthetic maps of the *GALEX* flux from the inferred SFH of Lewis et al. (2015). These maps were presented in Lewis et al. (2016). Here we briefly describe the modeling process but refer the reader to the original paper for full details.

We used the Lewis et al. (2015) SFHs to create a set of simple stellar population (SSP) models using the Flexible Stellar Population Synthesis (FSPS) code (Conroy et al. 2009; Conroy & Gunn 2010) with an age resolution of 0.025 dex from log(age) = 5.500 to log(age) = 10.175. We set the metallicity of each SSP to the mean metallicity of the SFH over the last 100 Myr. If there was no star formation in the last 100 Myr, we set the metallicity to that in the most recent time bin when the SFR was not zero. The result was a spectral energy distribution (SED) for each SSP.

Next, we resampled the SFH from an age resolution of 0.1 dex to $\sim 6.5 \times 10^4$ yr. We interpolated the SSP SEDs to the SFH time points, weighted each SED by the SFR at the specified time point, and summed the SSP SEDs to create the integrated dust-free model SED. This process was completed in each of our 100 × 400 pc size regions to create a spatially-resolved map of optically-derived, intrinsic (i.e., un-reddened) UV flux across the PHAT survey. We use the word 'region' throughout this paper to refer to these 100×400 pc

size pieces of the PHAT survey. We refer to the synthetic, dust-free flux derived in Lewis et al. (2016) as $f_{\rm FUV}^{\rm syn,0}$ and $f_{\rm NUV}^{\rm syn,0}$ in the FUV and NUV, respectively.

4.2.3 Modeled Reddened UV Flux

In Lewis et al. (2015), we measured the SFHs of each region by fitting the optical CMD with a linear combination of SSPs. Two of the free parameters in this process were the optical dust parameters, given by $A_{V,\rm SFH}$ and $dA_{V,\rm SFH}$. These two parameters can be broadly seen as a foreground dust component ($A_{V,\rm SFH}$) applied uniformly to all stars, and a differential dust component ($dA_{V,\rm SFH}$), which accounts for extinction internal to M31 and describes the spread in extinction values. In a given region, all stars are therefore reddened by some value between $A_{V,\rm SFH}$ and $A_{V,\rm SFH} + dA_{V,\rm SFH}$. These parameters were derived according to a Cardelli et al. (1989) attenuation curve with $R_V = 3.1$ and $f_{\rm bump} = 1.0$. We note, however, that if we had used a different attenuation curve to derive the SFHs, the resulting values of $A_{V,\rm SFH}$ and $dA_{V,\rm SFH}$ would not have changed substantially because the most common dust laws are in broad agreement in the optical.

In Lewis et al. (2016), we modeled the reddened UV flux using these same dust parameters: a Cardelli et al. (1989) attenuation curve with $R_V = 3.1$ and $f_{\rm bump}$=1.0 for consistency with the SFH measurement. We modeled the flux as described in Section 4.2.2. Before summing the individual SSP SEDs, we first reddened each component. The attenuation was added according to a Cardelli et al. (1989) curve with R_V=3.1 and an A_V drawn from a uniform, random distribution between $A_{V,\rm SFH}$ and $A_{V,\rm SFH} + dA_{V,\rm SFH}$. The attenuated SSP components were then weighted by the SFR and summed together to create the integrated, reddened model SED. These reddened fluxes are directly comparable to the observed *GALEX* UV flux in each region. We refer to the synthetic, reddened flux derived in Lewis et al. (2016) as $f_{\rm FUV}^{\rm syn}$ and $f_{\rm NUV}^{\rm syn}$ in the FUV and NUV, respectively.

While we had to assume an attenuation curve to compare the synthetic flux with the observed flux in Lewis et al. (2016), such an assumption is not necessary. The intrinsic, dust-free flux (Section 4.2.2) was calculated without assumptions about the dust law. By

applying various attenuation laws to the synthetic dust-free flux gives us the ability to probe attenuation instead of assuming it. We chose the Cardelli et al. (1989) attenuation law for consistency with the SFH measurement; however, the same reddening process works for any R_V-based attenuation law, including the Calzetti et al. (1994) curve and the Conroy et al. (2010) curve.

4.3 Fitting Parameters of the Attenuation Curve

4.3.1 Comparison of predicted to observed UV colors and magnitudes

Before under taking a full quantitative analysis, in Figure 4.2, we make a qualitative comparison of the predicted to observed UV properties.

In the left panel, we plot the ratio of the observed FUV flux to the synthetic, dust-free flux ($f^{\rm obs}_{\rm FUV}/f^{\rm syn}_{\rm FUV}$) as a function of the optical dust parameters, $\widetilde{A_V} = A_{V,\rm SFH} + 1/2\ dA_{V,\rm SFH}$. (Recall that the stars in each region are reddened by some value between $A_{V,\rm SFH}$ and $A_{V,\rm SFH} + dA_{V,\rm SFH}$. Therefore, $\widetilde{A_V}$ represents the median value of the dust parameter in each region). The middle panel is the same as the left panel except with the observed and synthetic, dust-free NUV flux. In the right panel, we plot the difference between the observed UV color and the synthetic, dust-free UV color, also as a function of the optical dust parameters. The grayscale represents the density of regions in each pixel of parameter space. White pixels indicate a higher density of regions. In all panels, we plot the running median and 1σ dispersion in red.

We first look at the data, shown in grayscale. In the left and middle panels, the ratio of the observed to intrinsic flux decreases as $\widetilde{A_V}$ increases. This corresponds to an increase in attenuation with increasing $\widetilde{A_V}$. We would expect that regions with a large amount of dust in the optical might also have increased attenuation in the UV. However, while the flux in the FUV and the NUV shows a strong decrease with $\widetilde{A_V}$, the delta UV color ([$m^{\rm obs}_{\rm FUV}$ - $m^{\rm obs}_{\rm NUV}$] - [$m^{\rm syn}_{\rm FUV}$ - $m^{\rm syn}_{\rm NUV}$]) shows little change with increasing $\widetilde{A_V}$.

We next compare the running medians in Figure 4.2 to predictions for three different

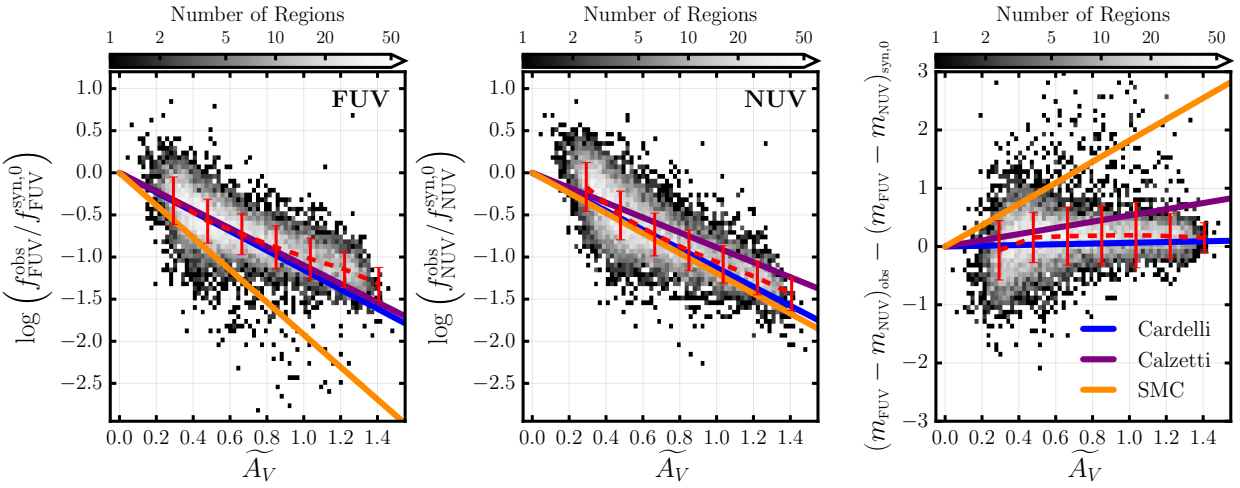

Figure 4.2 Comparison of the synthetic, dust-free and observed UV fluxes with optically-derived dust parameters. The left panel shows the ratio of the observed to synthetic, dust-free FUV flux. The middle panel shows the ratio of the observed to synthetic, dust-free NUV flux. In the right panel, we show the color difference between the observed and the synthetic, dust-free data. In each panel, the pixels (grayscale) are colored according to the number of regions that fall into each bin. The red points and dashed line show the running median and one sigma dispersion. The blue line is a Cardelli et al. (1989) extinction curve. The purple line is a Calzetti et al. (1994) attenuation curve. The orange line is an SMC (Pei 1992) attenuation curve.

attenuation curves. The blue line is a Cardelli et al. (1989) attenuation curve with R_V = 3.1, appropriate to the Solar neighborhood. The purple line is a Calzetti et al. (1994) attenuation curve with R_V = 4.05, derived in 'UV-bright', starburst galaxies. The orange line shows the attenuation curve derived in the Small Magellanic Cloud (SMC; Pei 1992).

Focusing on the left and middle panels that show the flux ratios in the FUV and NUV, respectively, the Cardelli et al. (1989) curve fits the data well, following the decrease in flux with increasing dust. However, while it agrees with the data within the 1σ dispersion shown in red, the slope is a bit steeper than the data require. This may suggest that the MW

default R_V may not be the optimal choice for M31. In the same two panels, the Calzetti et al. (1994) curve shows good agreement in the FUV (comparable to Cardelli). However, it is too shallow in the NUV, indicating that the observed NUV flux will be too bright if attenuated by a Calzetti curve. Finally, the SMC curve shows the opposite trend. The slope is much too steep in the FUV, indicating over-attenuation of the intrinsic flux, while it shows reasonable agreement in the NUV (comparable to Cardelli).

We now turn to the right panel, which shows the trend in δUV color with dust. As mentioned above, the data have essentially constant color. In general, shorter wavelengths suffer greater attenuation than longer wavelengths. This would suggest that $m_{\rm FUV}^{\rm obs}$ - $m_{\rm NUV}^{\rm obs}$ should be reddened because there should be more attenuation in the FUV than in the NUV. The magnitude in the FUV band increases (becomes fainter) more than that in the NUV band, so $m_{\rm FUV}^{\rm obs}$ - $m_{\rm NUV}^{\rm obs}$ would increase with increasing dust. Because the data do not show this trend, it suggests that something is reducing attenuation in the FUV or raising attenuation in the NUV.

The feature that is likely affecting the attenuation in the NUV is the 2175 Å bump. The bump is a very prominent feature in the MW attenuation curve (Figure 4.1) that increases the attenuation in the NUV but has little effect in the FUV. This feature could increase the attenuation in the NUV enough to offset the extra attenuation expected in the FUV, resulting in no change in color due to attenuation.

We see again that the Cardelli curve shows reasonable agreement with the data in the right panel. On the other hand, the Calzetti and SMC curves have *much* steeper slopes than the data require and result in *much* redder data than is observed. Neither the Calzetti nor the SMC curve has a 2175 Å bump and therefore has no method for increasing the NUV attenuation relative to the FUV attenuation. This suggests that M31 must have a 2175 Å bump feature in its attenuation curve.

We have shown that the overall fit of a Cardelli-like curve to the data is good, falling within 1σ of the median points across the entire $\widetilde{A_V}$ range. However, there is scatter about the median. The is approximately a 0.25 dex dispersion in the flux ratio at any value of $\widetilde{A_V}$,

as shown by the red error bars in each panel of Figure 4.2. Additionally, there are a number of points that do not appear to follow a Cardelli curve at all, but instead show better agreement with an SMC-type curve. This suggests that the parameters of the attenuation curve may not be uniform across the disk of M31, but may in fact show spatial variation. This variation is our impetus for performing a more advanced fitting to the reddened and dust-free data to see if the observed scatter is due to measurement uncertainty or if it represents intrinsic variation in the dust law.

4.3.2 Fitting of the Attenuation Curve

We now proceed to develop a more detailed model for the attenuation curve in M31.

The general agreement between the data and the Cardelli et al. (1989) curve in Figure 4.2 suggests that we should fit a curve with a rise to the UV and a significant 2175 Å bump. The Cardelli curve has a single adjustable parameter in R_V. It does not allow the strength of the 2175 Å bump, $f_{\rm bump}$, to change. To include variation in $f_{\rm bump}$, we adopt Conroy et al. (2010)'s formulae for construction of a Cardelli-like extinction curve with both R_V and $f_{\rm bump}$ as free parameters to be changed.

Examples from this set of parameterized attenuation laws are shown in Figure 4.3. In the left panel, we plot the Conroy attenuation curve with different values of R_V while holding $f_{\rm bump}$ equal to unity. These curves are the same ones that would come out of the Cardelli formulation. A smaller R_V results in a steeper curve in the UV and therefore greater attenuation. As R_V increases, the curves flatten. All curves have a bump feature in the NUV such that the attenuation at those wavelengths is elevated with a dip on either side.

In the right panel, we plot the Conroy attenuation curve with $R_V = 3.1$ and varying the strength of the bump feature, $f_{\rm bump}$, from 0.0 to 2.0, going from no bump to a bump that is twice as strong as that in the MW. As expected, this change affects only the 2175 Å bump feature; the curves overlap at other wavelengths. As $f_{\rm bump}$ increases, the bump features increases in size such that more attenuation is lost in the NUV.

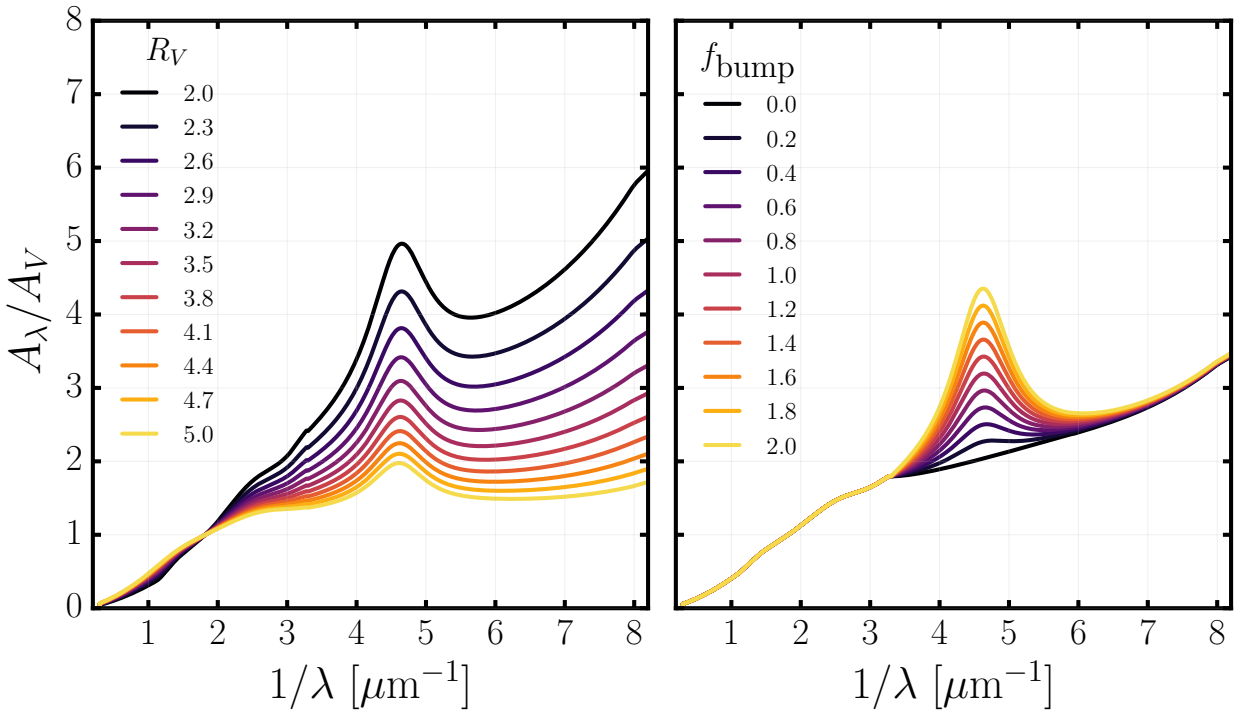

Figure 4.3 Effects of varying R_V or $f_{\rm bump}$. The left panel shows attenuation curves with fixed $f_{\rm bump} = 1.0$ and varying R_V from 2.0 (black) to 5.0 (yellow) As R_V increases, the attenuation curve flattens. The right panel shows attenuation curves with fixed $R_V = 3.1$ and varying $f_{\rm bump}$ from 0.0 (black) to 2.0 (yellow). $f_{\rm bump}$ represents the strength of the 2175 Å bump, so as $f_{\rm bump}$ increases, the bump is more pronounced.

4.3.3 Methodology

We take a two step process to analyze R_V and $f_{\rm bump}$. First, for each region, we derive the values of R_V and $f_{\rm bump}$ that produce the observed color and flux measurement for that region given the intrinsic synthetic flux derived in Section 4.2.2. We also derive the associated uncertainties in R_V and $f_{\rm bump}$ for each region. In the second step, we use the ensemble of inferred probability distributions of R_V and $f_{\rm bump}$ for each region to infer the global best fit for R_V and $f_{\rm bump}$ along with associated uncertainties. We now describe each step in detail.

Modeling the R_V and $f_{\rm bump}$ distributions for a single region

We first inferred probability distributions for R_V and $f_{\rm bump}$ for each region using the affine-invariant ensemble sampler in the Markov Chain Monte Carlo package `emcee` (Foreman-Mackey et al. 2013). To do so, we fit the ratios of observed to synthetic, dust-free UV flux ($x_F = f_{\rm FUV}^{\rm obs}/\ f_{\rm FUV}^{\rm syn,0}$ and $x_N = f_{\rm NUV}^{\rm obs}/\ f_{\rm NUV}^{\rm syn,0}$) as shown in the left two panels of Figure 4.2 and described below.

For simplicity, we set the value of A_V equal to $\widetilde{A_V}$ and then converted A_V to τ_V with:

$$A_\lambda = -2.5 \log_{10}\left(\frac{F_\lambda}{F_0}\right) = -\frac{2.5}{\ln(10)} \ln\left(\frac{F_\lambda}{F_0}\right) = 1.086 \ln\left(\frac{F_0}{F_\lambda}\right) = 1.086\,\tau_\lambda. \tag{4.2}$$

Therefore,

$$\tau_V = A_V/1.086. \tag{4.3}$$

At each step in (R_V, $f_{\rm bump}$) space, we generated a synthetic spectrum using the Flexible Stellar Population Synthesis (FSPS) code (Conroy et al. 2009; Conroy & Gunn 2010). We calculated τ_λ from the Conroy et al. (2010) attenuation curve given R_V, $f_{\rm bump}$, and τ_V and used it to redden the synthetic spectrum. We then converted the reddened and un-reddened spectra to magnitudes by weighting each spectrum by the *GALEX* response curves. Finally, we converted magnitudes to flux. We refer to these modeled fluxes as $f_{\rm FUV}^{\rm mod,red}$ and $f_{\rm NUV}^{\rm mod,red}$ for the reddened fluxes and $f_{\rm FUV}^{\rm mod,0}$ and $f_{\rm NUV}^{\rm mod,0}$ for the dust-free fluxes in the FUV and NUV, respectively. Note that these are different than the synthetic fluxes derived in Lewis et al. (2016).

We computed the likelihood of these modeled, reddened and dust-free fluxes given the observed *GALEX* and synthetic, dust-free fluxes, R_V, and $f_{\rm bump}$. We assumed flat priors on R_V and $f_{\rm bump}$ over the ranges R_V=[0, 10] and $f_{\rm bump}$=[0, 1.5]. The distributions for the UV ratios are:

$$p(x_F, x_N \mid A_V, R_V, f_{\rm bump}) = \frac{1}{\sqrt{2\pi(\sigma_F^2 + \sigma_N^2)}}\, e^{-\frac{1}{2}\left[\frac{(w_F - x_F)^2}{\sigma_F^2} + \frac{(w_N - x_N)^2}{\sigma_N^2}\right]} \tag{4.4}$$

where σ_F and σ_N are the uncertainties on the FUV and NUV observations, respectively.The parameters w_F and w_N are the modeled data calculated as a function of A_V, R_V and $f_{\rm bump}$ and given by $w_F(A_V, R_V, f_{\rm bump}) = f_{\rm FUV}^{\rm mod,red}(A_V, R_V, f_{\rm bump})/f_{\rm FUV}^{\rm mod,0}$ and $w_N(A_V, R_V, f_{\rm bump}) = f_{\rm NUV}^{\rm mod,red}(A_V, R_V, f_{\rm bump})/f_{\rm NUV}^{\rm mod,red}$.

We calculated the posterior probabilities in R_V and $f_{\rm bump}$ and saved the resulting distributions in R_V and $f_{\rm bump}$ for each region.

Inferring the intrinsic distribution of R_V and $f_{\rm bump}$ in M31

Given the set of measurements calculated above, we can infer ensemble characteristics about the distributions of R_V and $f_{\rm bump}$ under the assumption that they are all drawn from a single distribution. Specifically, we assume that the distribution of attenuation curves is normal with a mean of μ and a width of σ. That is, we find typical values for R_V and $f_{\rm bump}$ with some intrinsic scatter around those typical values.

We model the ensemble distribution following Foreman-Mackey et al. (2014). The marginalized likelihood of each parameter is given by

$$p(g \mid \theta) = \int \prod_k p(g_k \mid y_k) p\left(y_k \mid \theta\right) dy_k \tag{4.5}$$

where g_k is the data in each region k, y_k is the parameter for which we are finding the likelihood specified in each region, i.e., either R_V or $f_{\rm bump}$, and θ are the parameters of the assumed distribution. We will assume a normal distribution, so $\theta = [\mu, \sigma]$.

The posterior probability for each region is described by Bayes Theorem:

$$p(y_k \mid g_k, \alpha) = \frac{p(y_k \mid \alpha)\, p(g_k \mid y_k)}{p(g_k \mid \alpha)} \tag{4.6}$$

$p(y_k \mid g_k, \alpha)$ is the posterior probability of the parameters y_k conditioned on the data g_k and we use the notation α to represent the priors on the data g_k; $p(y_k \mid \alpha)$ is the prior probability on the desired parameters; $p(g_k \mid y_k)$ is the likelihood of the data, g_k given the parameters, y_k; and $p(g_k \mid \alpha)$ is the prior probability on the data itself.

We simplify the marginalized likelihood (Equation 4.5) by multiplying by unity

$$\frac{p(y_k \mid g_k, \alpha)}{p(y_k \mid g_k, \alpha)} \tag{4.7}$$

and re-arranging using Equation 4.6 to get

$$\frac{p(g \mid \theta)}{p(g \mid \alpha)} = \int \prod_k \frac{p(y_k \mid \theta)}{p(y_k \mid \alpha)} \, p(y_k \mid g_k, \alpha) \, dy_k. \tag{4.8}$$

The posterior probability, $p(y_k \mid g_k, \alpha)$ can be adequately constrained with a set of N samples drawn randomly from that distribution. We then use the Monte Carlo approximation of the integral

$$p(g) = \int y(x) g(x) dx = \frac{1}{n} \sum_{i=1}^{n} g(x_i) \tag{4.9}$$

to further simplify Equation 4.5 up to some extraneous constant

$$p(g \mid \theta) \approx \prod_k \frac{1}{N} \sum_{n=1}^{N} \frac{p(y_k^{(n)} \mid \theta)}{p(y_k^{(n)} \mid \alpha)}. \tag{4.10}$$

We selected a set number of samples, $N = 50$, randomly in each region. At each sample point, we calculated the likelihood of a given μ and σ and computed the log of the sum of the exponentials of all 50 samples per region. We then summed all region likelihoods to determine the full likelihood for a given μ and σ. For simplicity, we have modeled the R_V and $f_{\rm bump}$ distributions independently, though the two parameters are likely dependent in some way.

4.4 Results

Throughout the rest of this paper, we refer to the median value x in each region as $\widetilde{x}$. That is, the median R_V is given by $\widetilde{R_V}$ and the median $f_{\rm bump}$ is given by $\widetilde{f_{\rm bump}}$. The means of the ensemble values (i.e., of the distribution of single values for R_V and $f_{\rm bump}$ across the entire survey) are denoted by μ_{R_V} and $\mu_{f_{\rm bump}}$. On a region-by-region basis, the dispersions in R_V

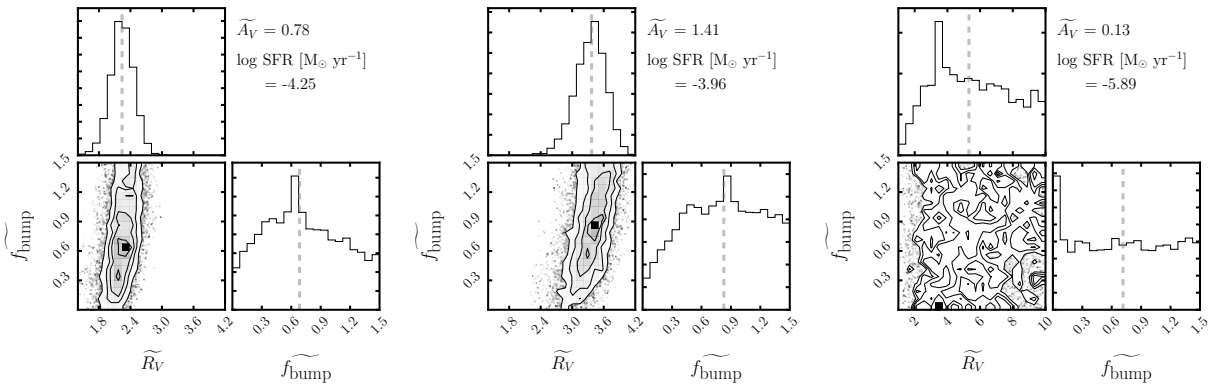

Figure 4.4 Joint and marginalized distributions of $\widetilde{R_V}$ and $\widetilde{f_{\rm bump}}$ for three different regions. In each panel, we have noted the $\widetilde{A_V}$ and SFR of that region. The dashed lines denote the median values of each parameter. In the left panel, we show the PDFs of a region with $\widetilde{A_V}$ and SFR that is typical of the average region. The $\widetilde{R_V}$ PDF is very well-behaved with a strong central value and a defined width. The $\widetilde{f_{\rm bump}}$ PDF is very different. While it does have a peak value, the distribution is certainly not normal. The region in the middle panel has a high SFR and $\widetilde{A_V}$ relative to the majority of regions. The $\widetilde{R_V}$ and $\widetilde{f_{\rm bump}}$ PDFs are similar to those in the left panel. In the right panel, we show a region with low $\widetilde{A_V}$ and low SFR. In this case, neither $\widetilde{R_V}$ nor $\widetilde{f_{\rm bump}}$ are well-constrained.

and $f_{\rm bump}$ are denoted by $\widetilde{\sigma_{R_V}}$ and $\widetilde{\sigma_{f_{\rm bump}}}$. The widths of the ensemble distributions in R_V and $f_{\rm bump}$ are denoted as σ_{R_V} and $\sigma_{f_{\rm bump}}$.

4.4.1 Region-by-Region Results

In Figure 4.4, we show the results of our fitting in three representative 100 pc pixels, each of which samples a different A_V and SFR. The region shown in the left panel is typical of the average region in our sample in terms of A_V and SFR. The $\widetilde{R_V}$ PDF is well-behaved with a median of $\sim$2.3 and a width of $\sim$0.45. The $\widetilde{f_{\rm bump}}$ PDF, on the other hand, is not as well localized. While it certainly has a point of highest likelihood at $\sim$0.6 (the median value is $\sim$0.7), it has non-negligible likelihood at all values of $\widetilde{f_{\rm bump}}$.

We show a high SFR, high A_V region in the middle panel. As with the left panel, the R_V PDF is well-constrained, but with a higher mean R_V of $\sim$3.4. Again, $f_{\rm bump}$ has a mild preference for a certain value though its likelihood space covers the limits of $f_{\rm bump}$ given in the fitting prior.

The region shown in the right panel behaves quite differently. This region has low A_V and low SFR and the distributions in $\widetilde{R_V}$ and $\widetilde{f_{\rm bump}}$ hold little information, as one might expect when the effects of dust are guaranteed to be small. The $\widetilde{R_V}$ PDF is much broader than in the high A_V regions ($\sigma \sim 2.7$ versus $\sigma \sim 0.2 - 0.3$). The peak of the $\widetilde{R_V}$ distribution is at $\sim$3.5, while the median value is $\sim$5. In this region, $\widetilde{f_{\rm bump}}$ is completely uninformative. As expected, it is difficult to fit the parameters of an extinction curve when there is little extinction.

We note that regions with low SFR and low $\widetilde{A_V}$ have poorly constrained values of $\widetilde{R_V}$ and $\widetilde{f_{\rm bump}}$. This is not surprising given the correlation between SFR and $\widetilde{A_V}$. Star formation occurs in regions of molecular gas and dust. At birth, stars are hidden inside their dusty natal clouds, which obscures their light. Therefore, regions of high star formation also tend to be dusty.

The above three examples cover a range of values in SFR and $\widetilde{A_V}$, and demonstrate the degree to which $\widetilde{R_V}$ and $\widetilde{f_{\rm bump}}$ are constrained in individual pixels. The median $\widetilde{R_V}$ varies significantly from region-to-region. The PDFs for $\widetilde{R_V}$ tend to be well-behaved, but with varying means and widths from region-to-region. We plot the full distribution in $\widetilde{R_V}$ in the top left panel of Figure 4.5 and quantify the distribution with boxplots in the top left panel of Figure 4.6. The $\widetilde{R_V}$ distribution for all regions is in black. The distribution has a median of $\widetilde{R_V} = 3.07$, with a long tail to larger values.

We examine the environmental dependence of the R_V distribution by plotting the distribution for all regions with SFR $> 10^{-5}$ $\rm M_\odot\,yr^{-1}$ in blue and all regions with $\widetilde{A_V} > 1.0$ in green. With either cut, the distribution narrows and loses its tail. This can also be seen in a reduction in the size of each box in Figure 4.6. Additionally, the R_V distribution shifts to slightly higher values when choosing only high $\widetilde{A_V}$ regions (with a median R_V of 3.33 at $\widetilde{A_V}$

> 1.0 and 2.96 at $\widetilde{A_V} < 1.0$), suggesting a dependence of $\widetilde{R_V}$ on $\widetilde{A_V}$.

The top right panel shows the distribution in $\widetilde{\sigma_{R_V}}$. As with the $\widetilde{R_V}$ distribution, it is highly peaked (the median value is 0.41) with a long tail to larger values. Additional cuts on SFR (blue) and $\widetilde{A_V}$ (green) result in tighter distributions with smaller medians (0.35 and 0.32, respectively). This substantial narrowing of the distribution is clearly seen in Figure 4.6.

We show the distributions of $\widetilde{f_{\rm bump}}$ and $\widetilde{\sigma_{f_{\rm bump}}}$ in the bottom two panels of Figure 4.5. The distribution in $\widetilde{f_{\rm bump}}$ stretches over the range from 0.2 to 1.2 with just a slight peak at 0.7. The distribution's width is comparable to the mean value of $\widetilde{\sigma_{f_{\rm bump}}}$, suggesting that most of the observed width could be consistent with just measurement errors. Applying cuts on SFR, $\widetilde{A_V}$, and $\widetilde{\sigma_{R_V}}$ does not significantly change the distribution of $\widetilde{f_{\rm bump}}$ in either peak or width, only slightly reducing the tail to high values of $\widetilde{f_{\rm bump}}$ and $\widetilde{\sigma_{f_{\rm bump}}}$(see Figure 4.6).

The $\widetilde{\sigma_{f_{\rm bump}}}$ distribution is plotted in the bottom right panel. This distribution is fairly narrow, with a median of 0.42. Additional cuts in SFR and $\widetilde{A_V}$ result in a slightly narrower distributions with medians to slightly smaller values of 0.41 and 0.40, respectively.

In all panels, the gray shaded region represents all regions with well-measured values of $\widetilde{R_V}$, given by $\widetilde{\sigma_{R_V}}$ / $\widetilde{R_V} < 0.2$. Application of this cut removes most of the tail to high $\widetilde{R_V}$ and high $\widetilde{\sigma_{R_V}}$ and tightens the distribution of all parameters.

We move now to an examination of the relationship between $\widetilde{R_V}$ and $\widetilde{f_{\rm bump}}$. We plot $\widetilde{R_V}$ versus $\widetilde{f_{\rm bump}}$ for all regions in Figure 4.7. Each circle represents a single region. Darker areas on the plot indicate a higher density of regions in that part of parameter space. There does not appear to be any correlation between $\widetilde{R_V}$ and $\widetilde{f_{\rm bump}}$. $\widetilde{R_V}$ values between 2 and 5 span almost the entire range in $f_{\rm bump}$. At larger values of $\widetilde{R_V}$, the distribution of $\widetilde{f_{\rm bump}}$ values narrow; however, these regions also all have large $\widetilde{\sigma_{R_V}}$ values, making their R_V measurements less reliable.

In Figure 4.8, we examine the individual regions in the context of the entire survey by plotting the distributions and spatial maps of $\widetilde{A_V}$, $\widetilde{\sigma_{R_V}}$ / $\widetilde{R_V}$ and $\widetilde{\sigma_{f_{\rm bump}}}$ / $\widetilde{f_{\rm bump}}$. These maps show the fractional width of the PDFs as a function of position, and thus show how well

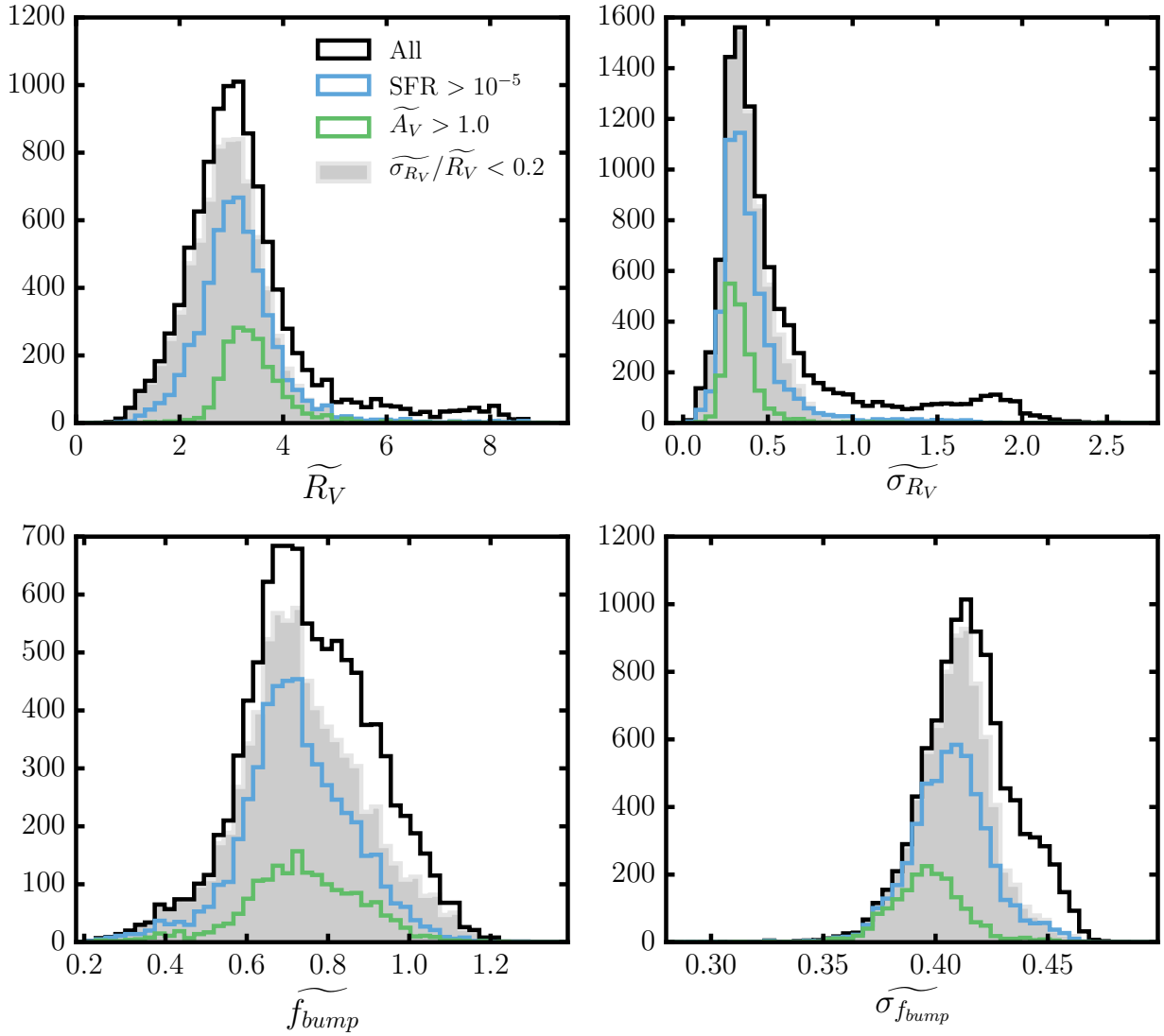

Figure 4.5 Distributions of $\widetilde{R_V}$, $\widetilde{f_{\rm bump}}$, and their dispersions. The black line shows the distribution of all regions. The blue line includes all regions with SFR $> 10^{-5}$ $M_\odot\,yr^{-1}$. The green line includes regions with $\widetilde{A_V} > 1.0$. The gray shaded area is the distribution of all regions with $\widetilde{\sigma_{R_V}}$ / $\widetilde{R_V} < 0.2$, representing regions with better measurements in R_V.

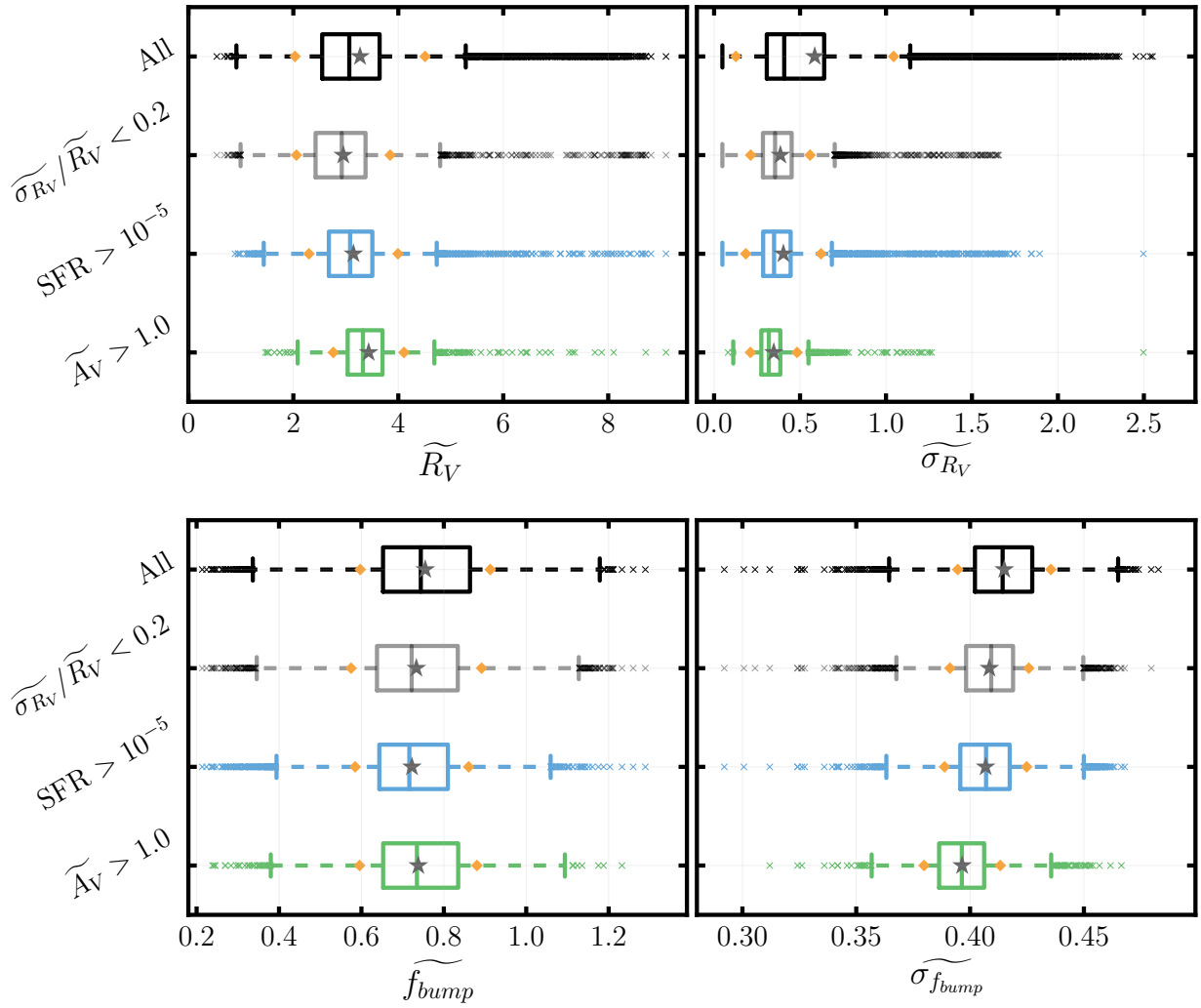

Figure 4.6 Boxplots of $\widetilde{R_V}$, $\widetilde{f_{\rm bump}}$, and their dispersions. The black line shows the distribution of all regions. The blue line includes all regions with SFR $> 10^{-5}$ $M_\odot$ yr^{-1}. The green line includes regions with $\widetilde{A_V} > 1.0$. The gray shaded area is the distribution of all regions with $\widetilde{\sigma_{R_V}}$ / $\widetilde{R_V} < 0.2$, representing regions with better measurements in R_V. Each box marks the quartiles and median of the distribution. The whiskers are at 1.5 times the interquartile range. All regions beyond this range are marked by an 'X'. The gray star denotes the mean of the distribution, and the small orange diamonds are at 1σ from the mean.

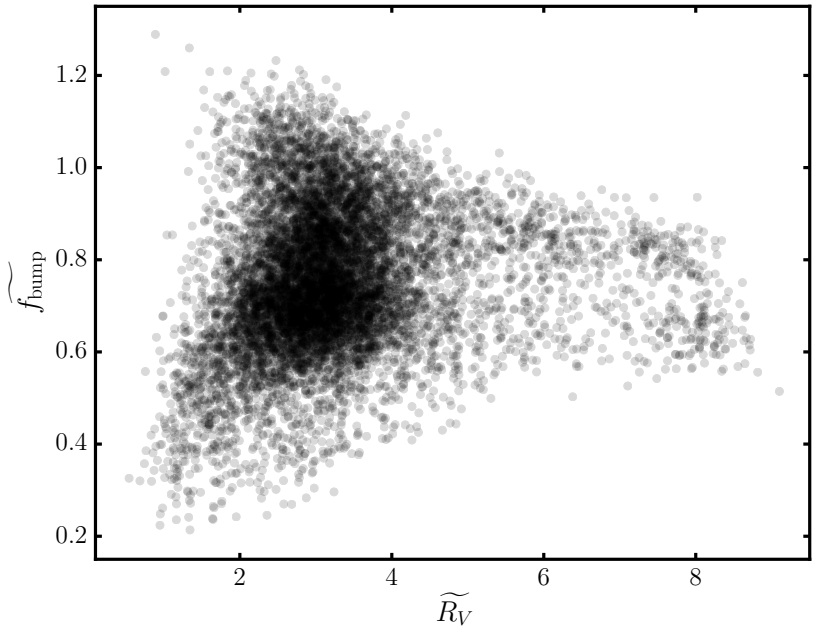

Figure 4.7 Scatter plot of $\widetilde{R_V}$ and $\widetilde{f_{\rm bump}}$. Each circle represents a single region. Darker areas indicate a higher density of regions. There is not a strong correlation between $\widetilde{R_V}$ and $\widetilde{f_{\rm bump}}$.

$\widetilde{R_V}$ and $\widetilde{f_{\rm bump}}$ are measured within individual regions. We plot $\widetilde{A_V}$ in the top panel. The distribution of values is plotted on the left and the map is shown on the right. As may be expected, M31's ring features have larger dust content than the inter-ring regions.

The middle panel shows the distribution of $\widetilde{\sigma_{R_V}}$ / $\widetilde{R_V}$ on the left and its spatial variation on the right. There is a clear peak in the distribution at 0.1 with a long tail to higher values, where low values represent tighter constraints on $\widetilde{R_V}$ in a given region. Comparison with the map on the right clearly shows that the most well-constrained regions are located in M31's ring features where the extinction is highest. As we showed in Figure 4.4, it is much easier to constrain the parameters of the extinction curve when there is more dust.

In the lower panel of Figure 4.8, we plot the distribution of $\widetilde{\sigma_{f_{\rm bump}}}$ / $\widetilde{f_{\rm bump}}$ on the left and its spatial variation on the right. Focusing on the distribution, we see that the fractional uncertainty on $\widetilde{f_{\rm bump}}$ is much larger than for $\widetilde{R_V}$, with a peak in the distribution at 0.5. Not

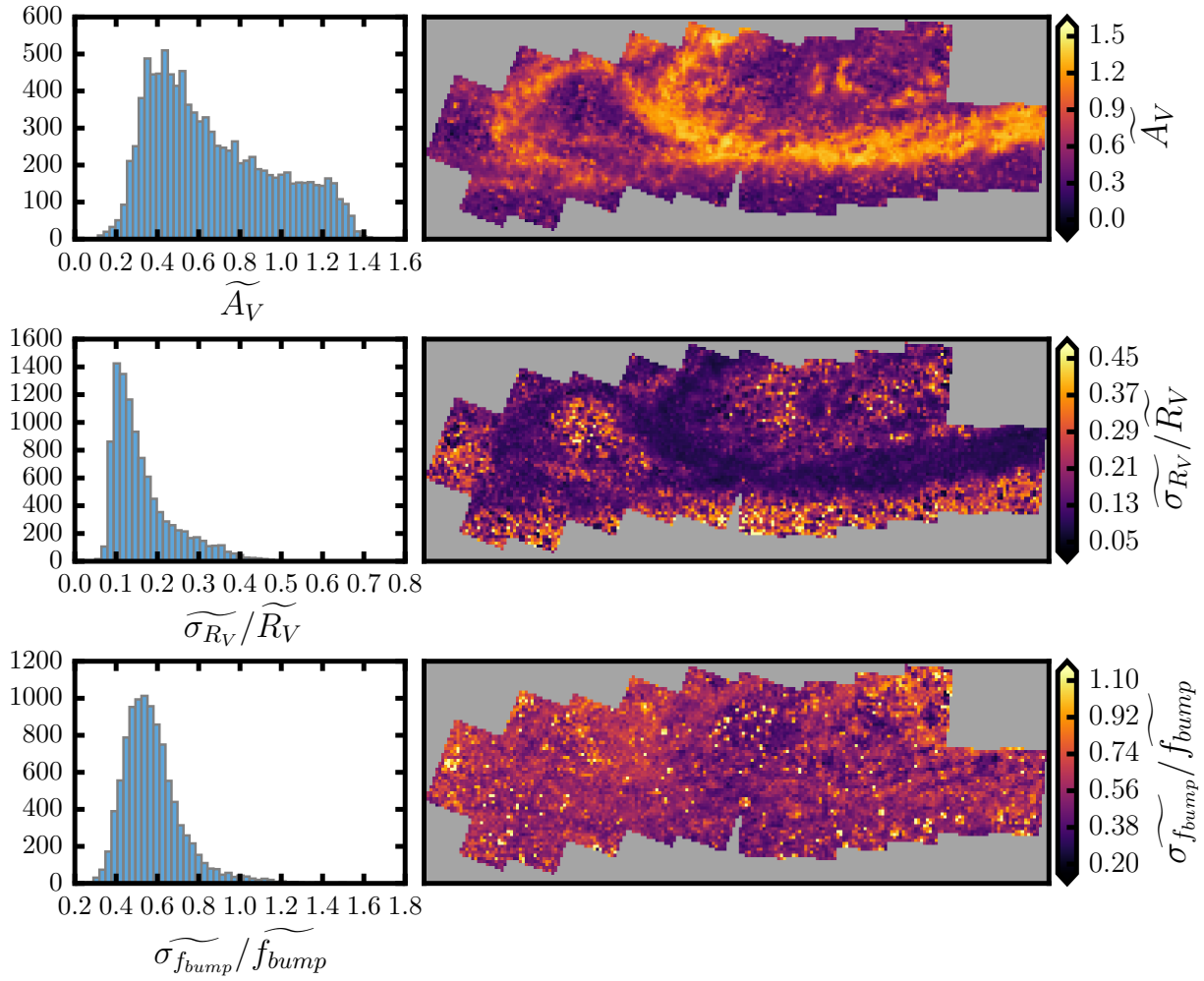

Figure 4.8 Distributions of $\widetilde{A_V}$, $\widetilde{\sigma_{R_V}}$ / $\widetilde{R_V}$ and $\widetilde{\sigma_{f_{\rm bump}}}$ / $\widetilde{f_{\rm bump}}$. In the top panel, we plot the 1D distribution of $\widetilde{A_V}$ on the left and its spatial variation on the right. The middle panel shows the distribution of $\widetilde{\sigma_{R_V}}$ / $\widetilde{R_V}$ on the left and a spatial map on the right. The bottom panel shows the 1D distribution and map for $\widetilde{\sigma_{f_{\rm bump}}}$ / $\widetilde{f_{\rm bump}}$. Regions with well-measured $\widetilde{R_V}$ values (low values of $\widetilde{\sigma_{R_V}}$ / $\widetilde{R_V}$) occur in regions of elevated dust content where $\widetilde{A_V}$ is highest. The $\widetilde{f_{\rm bump}}$ measurements show no correlation with $\widetilde{A_V}$.

surprisingly, the map on the right shows very little structure. The lack of spatial structure and the larger variation in the distribution of $\widetilde{f_{\rm bump}}$ corroborates the single region results in Figure 4.4 which show only weak constraints on $\widetilde{f_{\rm bump}}$ on 100 pc scales.

Figure 4.5 suggests that the distributions of $\widetilde{R_V}$ and $\widetilde{f_{\rm bump}}$ are roughly gaussian, particularly for the regions with good measurements in $\widetilde{R_V}$. Although the distributions are broad, it is unclear if their widths are due to intrinsic dispersion in the values of $\widetilde{R_V}$ and $\widetilde{f_{\rm bump}}$ across M31, or whether the observed width is due primarily to the intrinsic uncertainties in the measurement of these parameters.

4.4.2 Ensemble Results

We address this issue by computing the ensemble distributions of R_V and $f_{\rm bump}$, as described in Section 4.3.3, by assuming that the parameters for the individual region PDFs could each be drawn from a normal distribution of mean μ and width σ in R_V and $f_{\rm bump}$. If the observed dispersions in the left panels of Figure 4.5 are dominated by measurement errors, then the widths, σ, will be small. Larger values of σ will indicate that the true values of R_V and/or $f_{\rm bump}$ vary significantly across the disk. The results of the fitting process are shown in Figure 4.9 and summarized in Table 4.1.

For these fits, we first exclude the 24% of regions with poorly measured values of $\widetilde{R_V}$ ($\widetilde{\sigma_{R_V}}$ / $\widetilde{R_V} > 0.2$; the gray shaded region in Figure 4.5 and the gray box in Figure 4.6). This choice removes much of the tail to large R_V, making the Gaussian assumption more likely to be a reasonable model for the intrinsic distributions of R_V and $f_{\rm bump}$.

Figure 4.9 shows ensemble values of $\mu_{R_V} = 2.94$ and $\mu_{f_{\rm bump}} = 0.68$ in M31. Additionally, these mean values are very well-constrained (± 0.01). The mean R_V is $\sim$5% smaller than the canonical value in the Milky Way ($R_V = 3.1$). We must note, however, that the MW value is an average over $\sim$30 lines of sight which vary from 2 to greater than 5 (e.g., Cardelli et al. 1989). Uncertainties on measurements of R_V in the MW are half the size of the typical value in this study, generally no more than $\sim$0.2 (e.g., Harris 1973; Schultz & Wiemer 1975; Barlow & Cohen 1977; Sneden et al. 1978) compared to $\sim$0.7 here. Although our measured value of

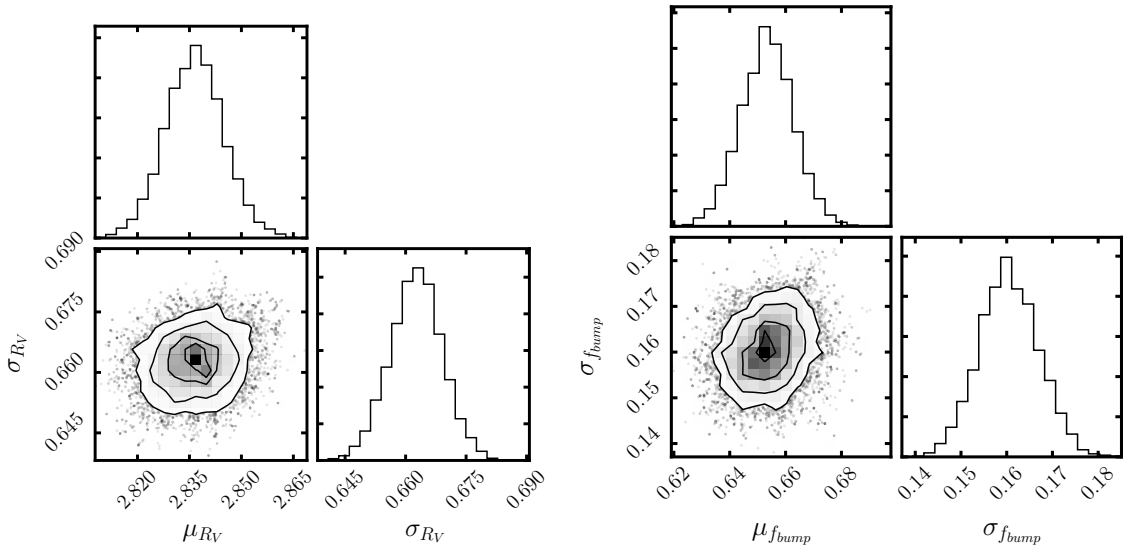

Figure 4.9 Joint and marginalized distributions for the ensemble distributions of R_V (left) and $f_{\rm bump}$(right) for all regions with $\widetilde{\sigma_{R_V}}$ / $\widetilde{R_V} < 0.2$. The distribution for the entire data set and those for other cuts on the data look very similar.

R_V is 16σ below the canonical MW value, if the uncertainties in the MW are included, our ensemble value of R_V in M31 is consistent with the MW canonical value.

Studies in the MW, however, generally use samples of young, short-lived, UV-bright O and B stars. For a closer comparison with the current study, we select only the regions with very high star formation over the past 100 Myr. These are the regions most likely to contain such short-lived stars. When we model only the regions with SFR $> 10^{-4}$ $M_\odot$ yr^{-1}, we find $\mu_{R_V} = 3.14 \pm 0.02$ and $\sigma_{R_V} = 0.34$. These numbers are in much closer agreement with the canonical MW values.

Figure 4.9 also shows that the inferred intrinsic widths of the distributions are significant. The intrinsic R_V distribution is relatively wide ($\sigma_{R_V} = 0.71$), suggesting that R_V indeed varies significantly on 100 pc scales across M31, and that the observed variations are not solely due to measurement errors. This conclusion is not unexpected, given the spatial coherence of the variations seen in Figure 4.5. Comparing the typical measurement uncertainty of $\widetilde{\sigma_{R_V}}$

$\sim$0.4 on the individual regions to the inferred intrinsic width of the distribution (σ_{R_V} $\sim$0.68), it's clear that the observed with of the $\widetilde{R_V}$ distribution in Figure 4.5 is dominated by the dispersion in the population.

The 2175 Å bump feature in M31 appears to be weaker than that in the MW. We find $\mu_{f_{\rm bump}} = 0.68 \pm 0.01$, relative to the MW's $f_{\rm bump}$=1.0. Figure 4.9 also shows that M31's 2175 Å bump is weaker than that of the Milky Way, which has $f_{\rm bump} = 1.0$. In contrast to the μ_{R_V} distribution, the $\mu_{f_{\rm bump}}$ distribution is fairly narrow ($\sigma_{f_{\rm bump}}$=0.19$\pm$0.01), indicating that the observed $f_{\rm bump}$ distribution in Figure 4.5 is dominated by the much larger measurement uncertainties ($\widetilde{\sigma_{f_{\rm bump}}}$ $\sim$0.42). The intrinsic narrowness also suggests that the 2175 Å bump in M31 is indeed likely to be globally weaker than that in the Milky Way.

4.4.3 Extinction Parameter Dependence on A_V, SFR, and environment

We have computed the region and ensemble distributions of R_V and $f_{\rm bump}$ across the PHAT survey area. In Figure 4.4, we showed that SFR and $\widetilde{A_V}$ can vary substantially from region-to-region. In this section, we examine the relationship (or lack thereof) between the two parameters of the UV dust distribution, R_V and $f_{\rm bump}$, and the SFR and $\widetilde{A_V}$ in each region.

Variation with A_V

It has been suggested that R_V varies with A_V, in that stars with high A_V tend to sample dense regions (i.e., the centers of molecular clouds), and in these dense regions, one would expect that the rate of dust grain growth would be higher (e.g., Whittet et al. 2001). Therefore, as A_V increases, R_V is also expected to increase.

We first visualize this possible dependence in the left column of Figure 4.10 where we plot $\widetilde{R_V}$ versus $\widetilde{A_V}$. Each pixel is colored according to the median SFR of all regions that fall in that part of parameter space. The top row includes all regions and the bottom row includes all regions with $\widetilde{\sigma_{R_V}} < 0.8$, i.e., where $\widetilde{R_V}$ is relatively well-measured. The blue contours in each plot indicate pixels with 5, 20, and 40 regions. Looking at the lower panel,

Table 4.1. Ensemble Parameters for R_V and $f_{\rm bump}$

Selection	% Regions	Parameters	μ	σ
All Regions	100	R_V	2.94 ± 0.01	0.71 ± 0.01
		$f_{\rm bump}$	0.68 ± 0.01	0.19 ± 0.01
$\widetilde{\sigma_{R_V}}$ / $\widetilde{R_V} < 0.2$	76	R_V	2.84 ± 0.01	0.66 ± 0.01
		$f_{\rm bump}$	0.65 ± 0.01	0.16 ± 0.01
A_V+ 1/2 $dA_V > 0.5$	63	R_V	3.06 ± 0.01	0.58 ± 0.01
		$f_{\rm bump}$	0.67 ± 0.01	0.16 ± 0.01
A_V+ 1/2 $dA_V > 1.0$	18	R_V	3.31 ± 0.02	0.44 ± 0.01
		$f_{\rm bump}$	$0.66^{+0.02}_{-0.01}$	0.12 ± 0.01
SFR $> 10^{-5}$ $M_\odot$ yr^{-1}	52	R_V	3.01 ± 0.01	0.59 ± 0.01
		$f_{\rm bump}$	0.63 ± 0.01	0.14 ± 0.01
SFR $> 10^{-4}$ $M_\odot$ yr^{-1}	7.6	R_V	3.14 ± 0.02	0.34 ± 0.01
		$f_{\rm bump}$	0.63 ± 0.02	0.12 ± 0.01
Inner Regions	15	R_V	2.59 ± 0.02	$0.62^{+0.02}_{-0.01}$
		$f_{\rm bump}$	0.68 ± 0.03	0.21 ± 0.02
Outer Regions	85	R_V	3.00 ± 0.01	0.68 ± 0.01
		$f_{\rm bump}$	0.71 ± 0.01	0.19 ± 0.01
Inner Regions & SFR $> 10^{-5}$ $M_\odot$ yr^{-1}	7.7	R_V	2.55 ± 0.02	0.60 ± 0.02
		$f_{\rm bump}$	0.53 ± 0.03	0.16 ± 0.02
Outer Regions & SFR $> 10^{-5}$ $M_\odot$ yr^{-1}	44	R_V	3.08 ± 0.01	0.54 ± 0.01
		$f_{\rm bump}$	0.64 ± 0.01	0.14 ± 0.01

Note. — Parameters of the ensemble distributions for R_V and $f_{\rm bump}$ with cuts on $\widetilde{A_V}$, SFR, $\widetilde{\sigma_{R_V}}$ / $\widetilde{R_V}$, and location. The first column indicates the region selection. The second column gives the percentage of all regions that are included in that selection. The fourth and fifth columns give the mean and sigma, respectively, of the normal distribution of R_V and $f_{\rm bump}$.

a correlation between $\widetilde{R_V}$ and $\widetilde{A_V}$ is clear. Regions with low $\widetilde{A_V}$ have low $\widetilde{R_V}$, while those with high $\widetilde{A_V}$ tend to have higher $\widetilde{R_V}$.

In the middle panel of Figure 4.10, we include the relationship with $\widetilde{f_{\rm bump}}$ by plotting $\widetilde{f_{\rm bump}}$ versus $\widetilde{R_V}$ with each pixel colored according to the median $\widetilde{A_V}$ of all regions that fall within that pixel. The relationship between $\widetilde{R_V}$ and $\widetilde{A_V}$ is visible, particularly in the bottom panel where we have removed high-noise regions. As $\widetilde{R_V}$ increases, so too does $\widetilde{A_V}$. The inclusion of $\widetilde{f_{\rm bump}}$ does not provide any additional information. The range in $\widetilde{A_V}$ is observed at all values of $\widetilde{f_{\rm bump}}$.

We further examine the dependence of R_V on A_V by modeling the ensemble distribution again, this time cutting out the regions with $\widetilde{A_V} < 0.5$. In this case, we find that the mean of the R_V distribution increases to $\mu_{R_V} = 3.06$ and the width of the distribution decreases slightly to $\sigma_{R_V} = 0.58$, while the $f_{\rm bump}$ distribution remains unchanged. This behavior continues if we compute the ensemble distributions with stricter cuts on $\widetilde{A_V}$. For $\widetilde{A_V} > 1.0$, we find $\mu_{R_V} = 3.3$, 6% larger than the MW value, and $\sigma_{R_V} = 0.44$. Again, the $\mu_{f_{\rm bump}}$ distributions are largely unchanged. These results are included in Table 4.1.

The effect of these cuts on $\widetilde{A_V}$ visibly affect the distribution of attenuation curves across M31. In Figure 4.11, we plot attenuation curves drawn from a sample of the ensemble distributions described in Table 4.1. The top left corner includes all regions. The mean curve with $\mu_{R_V} = 2.94$, σ_{R_V}=0.71, $\mu_{f_{\rm bump}}$=0.68, and $\sigma_{f_{\rm bump}} = 0.19$ is shown as the thick black line. We then created two normal distributions, one for R_V and one for $f_{\rm bump}$ with the given mean and width, and drew samples from each to generate extinction curves allowed by those distributions. Those curves are plotted as thin gray lines. For comparison, the MW curve is shown with the dashed black line.

In the bottom right corner, we repeat the same exercise using the ensemble results calculated for regions with $\widetilde{A_V} > 1.0$. The thick green line represents the total ensemble value, while the thin green lines are attenuation curves created from draws from the R_V and $f_{\rm bump}$ distributions given by the mean and width of the ensemble. In this panel, it is clear that a cut in $\widetilde{A_V}$ dramatically reduces the spread in attenuation curves that can be drawn from the

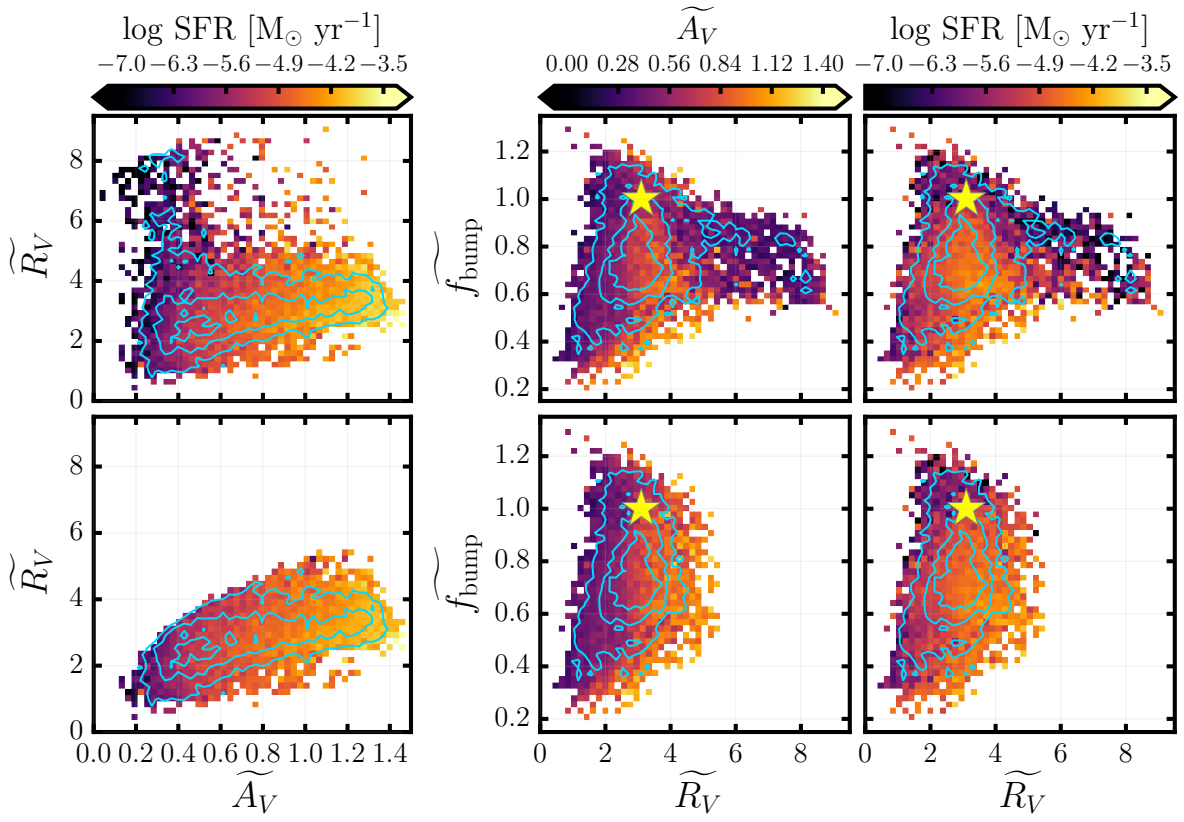

Figure 4.10 The relationship between SFR, $\widetilde{A_V}$, $\widetilde{R_V}$, and $\widetilde{f_{\rm bump}}$. In the left and right panels, each pixel is colored according to the median SFR of all regions that fall within that pixel. In the middle panel, each pixel is colored according to the median value of $\widetilde{A_V}$. The top panels include all regions. The bottom panels include only regions with $\widetilde{\sigma_{R_V}} < 0.8$. The blue lines contour pixels with 5, 20, and 40 regions. The yellow star marks the MW values.

distribution.

Variation with SFR

R_V may also vary with SFR. R_V is a strong indicator of the dust grain size distribution, with larger values of R_V indicating larger grains. Star formation can alter the grain size distribution, and as a result, it can change R_V. However, the effect of star formation on dust

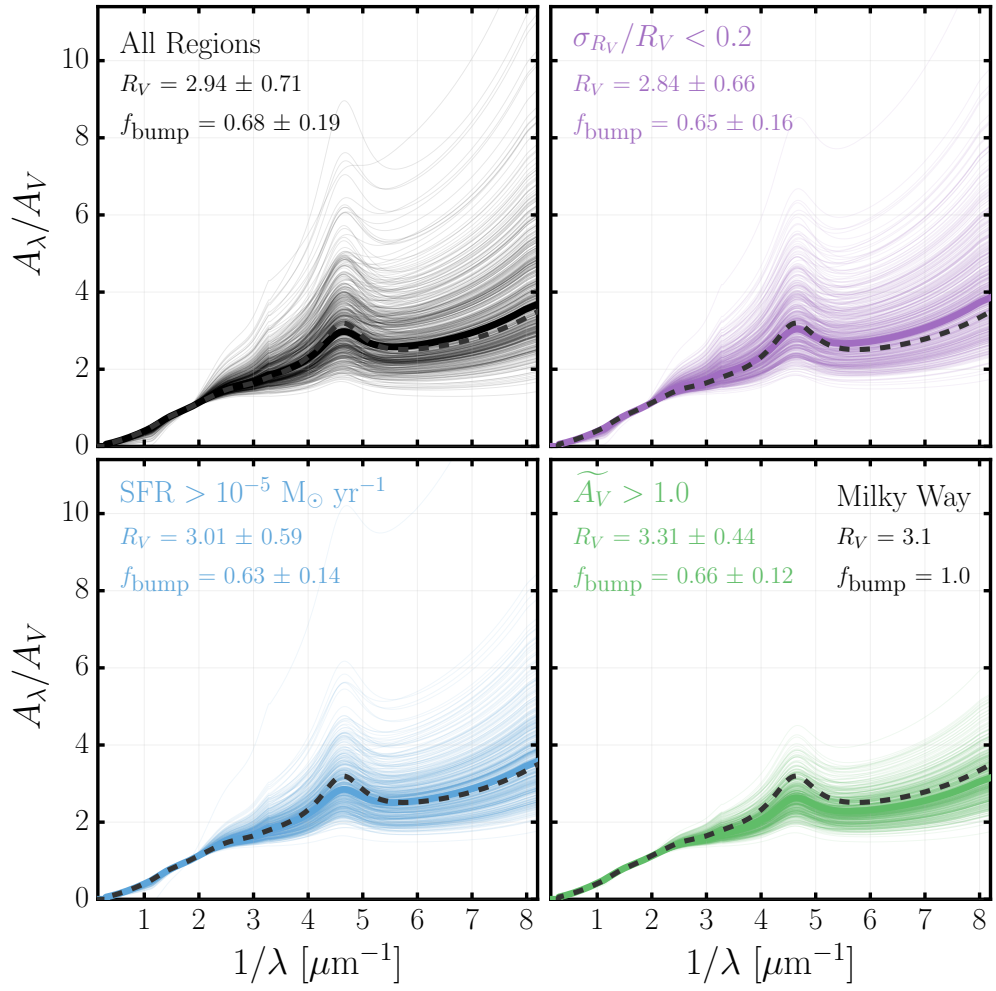

Figure 4.11 Sample attenuation curves drawn from ensemble distributions with various cuts on the data. The top left panel shows 500 samples drawn from the normal distribution with the parameters determined from solving for the ensemble distribution using all regions in M31. The top right panel shows samples drawn from the ensemble distribution of all regions with σ_{R_V} / $R_V < 0.2$. The bottom left attenuation curves are drawn from the ensemble of high SFR regions with SFR $> 10^{-5}$ M$_\odot$ yr^{-1}. The bottom right panel plots attenuation curves drawn from high dust regions with $\widetilde{A_V} > 1.0$. All panels include 500 samples shown by thin, transparent lines. The thick solid line represents the peak of the distribution. The black dashed line in each panel shows the attenuation curve for the MW.

is complex. Star formation change the dust distribution either through grain destruction or by grain production in supernovae and stellar winds. Additional complexities arise due to the correlation of SFR with A_V or with the total gas which also tracks A_V. Therefore, while we characterize the relationship between SFR and R_V, disentangling the various dependencies driving the observed relationship is likely not possible.

We examine the relationship between R_V, $f_{\rm bump}$, and SFR in each of our regions in the right column of Figure 4.10 where we have plotted $\widetilde{f_{\rm bump}}$ versus $\widetilde{R_V}$ with pixels colored according to the median of the 100 Myr SFRs for our regions, when binned by the region's $\widetilde{f_{\rm bump}}$ and $\widetilde{R_V}$. As before, the top panel includes all regions and the bottom panel includes regions with $\widetilde{\sigma_{R_V}} < 0.8$. The blue contours mark number density levels of 5, 20, and 40 regions per pixel.

Regions with the highest SFR ($> 10^{-5}$ $\rm M_\odot\,yr^{-1}$) tend to have higher values of $\widetilde{R_V}$. This correlation is especially visible in the bottom panel where we removed the regions with poorly constrained $\widetilde{R_V}$ ($\widetilde{\sigma_{R_V}} > 0.8$). This result is unsurprising given the correlation between SFR and $\widetilde{A_V}$ and the strong trend of $\widetilde{R_V}$ with $\widetilde{A_V}$ (the left panel of Figure 4.10). Additionally, regions with $f_{\rm bump} > 1.0$ are almost entirely confined to low SFRs, with SFR $< 10^{-5}$ $\rm M_\odot\,yr^{-1}$.

The lowest SFR regions occur at the highest values of $\widetilde{R_V}$. We note, however, that these regions are all eliminated in the cut on $\widetilde{\sigma_{R_V}}$. Nevertheless, this correlation explains our ensemble results, where when we select just high SFR regions, $\mu_{f_{\rm bump}}$ decreases and μ_{R_V} increases. The effect is not strong; the decrease in $f_{\rm bump}$ is minimal due to the paucity of regions with high $f_{\rm bump}$ values.

Spatial Variation of R_V and $f_{\rm bump}$

In Figure 4.12, we show maps of the average 100 Myr SFR, median $\widetilde{R_V}$, and $\widetilde{f_{\rm bump}}$ in each region. The $\widetilde{f_{\rm bump}}$ map is relatively flat, as is expected from its large individual uncertainties (Figure 4.5) and the low variation detected in the width of the ensemble of regions (Figure 4.9). When compared with the top panel, we see that the highest $\widetilde{f_{\rm bump}}$ values occur in the

low-SFR regions between the inner ring feature and the 10-kpc ring, as well as the regions outside of the ring.

The $\widetilde{R_V}$ map shows shows much more structure. Figure 4.12 shows that the 10-kpc ring spans a relatively narrow range in R_V, varying around the median value from 2.6 – 3.2. Regions outside of the ring features have the highest R_V and regions between the ring features have the lowest R_V. These are, once again, the lowest SFR regions as well as the regions with the least amount of dust, which limits the usefulness of their constraints on R_V.

We can pick out the variation in the high SFR regions more clearly in Figure 4.13. In this plot, we have colored each region by the difference between its median R_V or $f_{\rm bump}$ value and that of the ensemble for M31: $\widetilde{R_V}$ - μ_{R_V} and $\widetilde{f_{\rm bump}}$ - $\mu_{f_{\rm bump}}$. The R_V map in the top panel shows distinct variation amongst the ring features. The 10-kpc ring generally has higher R_V than the ensemble though it varies from +0.1 to +1.0 or more. Regions of higher R_V also coincide with star-forming regions and OB associations along the eastern side of the 10-kpc ring. However, OB 54 (van den Bergh 1964) in Brick 15 (white region at the top and center of the top panel of Figure 4.13) has an R_V that is approximately equal to that of the ensemble.

Figure 4.13 also shows a difference between the inner region of the galaxy and the outer regions. The central area is mostly colored red in this figure, indicating that the median $\widetilde{R_V}$ in each region is smaller than the ensemble value of $\mu_{R_V} = 3.01$ for the highest SFR regions. The 10-kpc ring and outer ring feature are primarily white or blue in color, indicating that the median $\widetilde{R_V}$ in each region is equal to or greater than the ensemble value.

We quantify this difference by modeling the ensemble distributions for the inner region and the outer regions, independently, with no cuts on SFR. When we do that, we find that the inner regions have $\mu_{R_V} = 2.59 \pm 0.02$ and $\sigma_{R_V} = 0.62^{+0.02}_{-0.01}$. All other regions have ensemble values of $\mu_{R_V} = 3.00 \pm 0.01$ and $\sigma_{R_V} = 0.68 \pm 0.01$. This suggests that the observed difference between the inner and outer regions of the galaxy is real. This is also in agreement with studies of the extinction curve toward the bulge (Section 4.5.1), which claim that R_V is smaller in the central regions than in the outer regions of the galaxy.

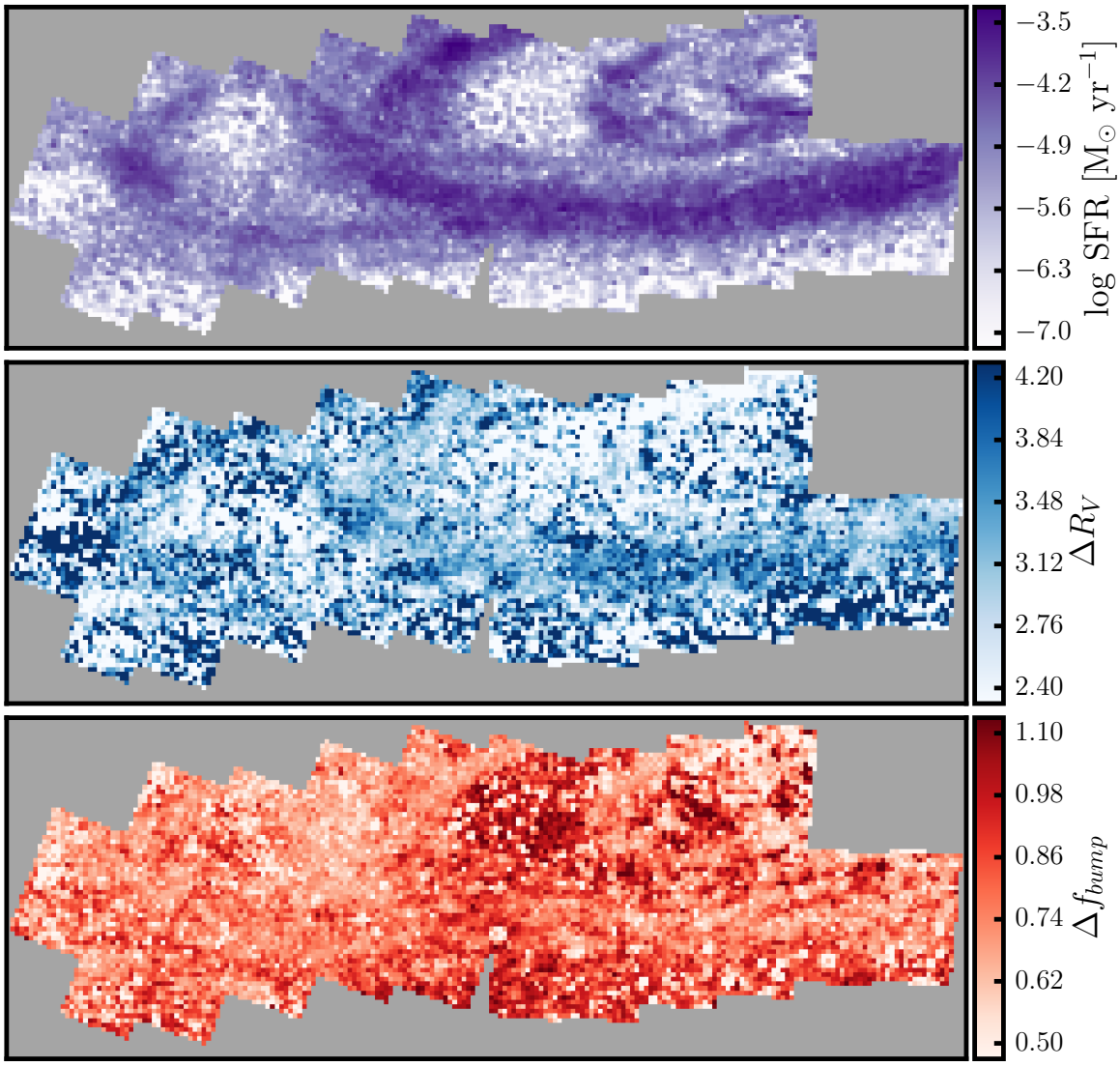

Figure 4.12 Maps of SFR (top, purple), R_V (middle, blue) and $f_{\rm bump}$(bottom, red) across the PHAT survey. Each region is colored according to its median 100 Myr SFR, R_V, and $f_{\rm bump}$ value, respectively. The maps are oriented such that north is to the top left and east is towards the bottom.

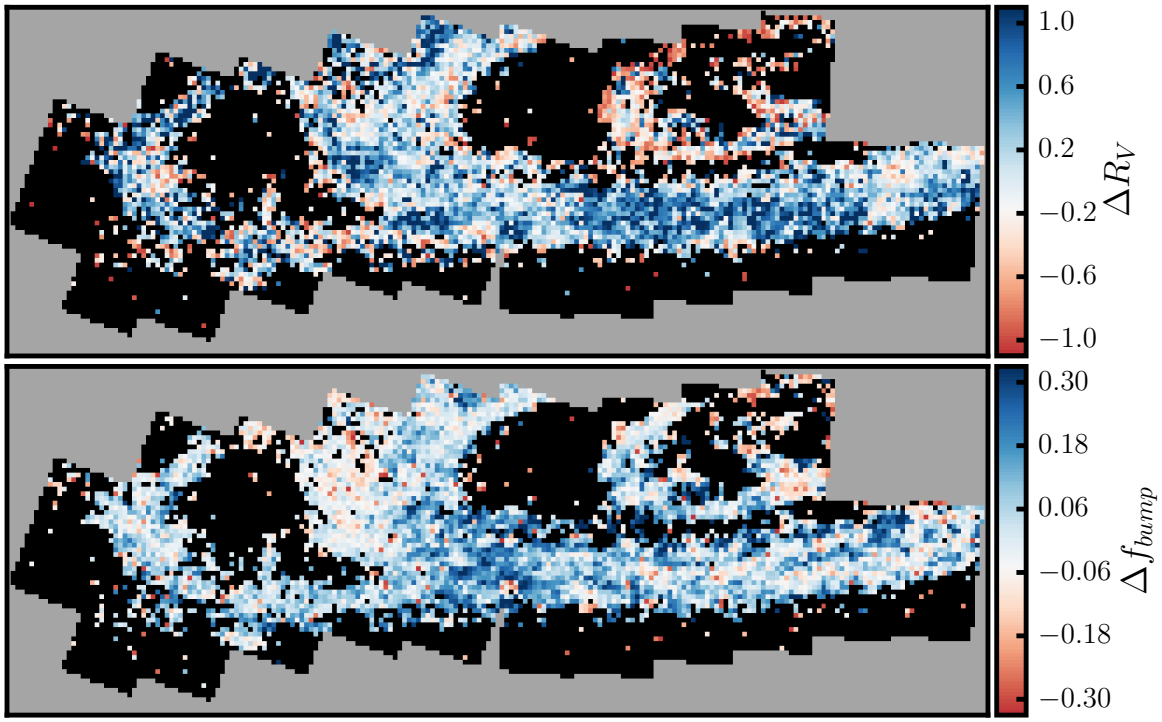

Figure 4.13 Maps of Δ R_V (top, blue) and Δ $f_{\rm bump}$(bottom, red) across the PHAT survey. Each region is colored according to the difference between its value and M31's ensemble: $\widetilde{R_V}$ - μ_{R_V} and $\widetilde{f_{\rm bump}}$ - $\mu_{f_{\rm bump}}$. Regions colored blue have R_V or $f_{\rm bump}$ higher than the mean and regions colored red are lower than the mean. All regions with SFR $< 10^{-5}$ $M_\odot$ yr^{-1} are colored black.

4.5 Discussion

4.5.1 Comparison with existing R_V results in M31

As one of only a few nearby galaxies with resolved stars, there have been a number of studies examining the extinction curve of M31. Bianchi et al. (1996) used *HST* UV spectra of OB stars in M31 to derive the ultraviolet extinction curve using multiple techniques. They found that the extinction curve had a similar shape to that in the MW (R_V ~3.1), but that the 2175 Å bump feature was weaker, if only at the 1σ level. This finding from traditional

spectral analysis is completely consistent with the results presented in this paper.

In a follow-up study to Bianchi et al. (1996), Clayton et al. (2015) also used *HST* spectra to examine the extinction curves towards reddened OB stars in M31. They do not explicitly list R_V or bump strength for each of their four curves, but they do note that they cover a range of R_V, from MW-like to SMC like, with differing 2175 Å bump strengths.

In a study toward the bulge of M31, Melchior et al. (2000) used ground-based optical images to derive a much steeper slope for the M31 extinction curve than for the MW, with $R_V = 2.1$. This finding is entirely inconsistent with our results and is likely due to the fact that the bulge has low attenuation due to a low dust column (e.g., Groves et al. 2012). Additionally, as previously noted, optical data alone provide only minimal discrimination of variation in the slope of the attenuation curve. Nevertheless, this result provides further support to the suggestion that R_V increases as A_V increases, or vice versa.

More recently, using a combination of *HST* and *Swift/UVOT* imaging, Dong et al. (2014) measured the extinction curve toward 5 regions in the bulge of M31 and found that the curves were steeper than that in the MW, with $R_V = 2.4 - 2.5$. While they did find 2175 Å bumps in their extinction curves, they do not comment on their strength relative to the MW.

Our ensemble result agrees very well with existing studies of M31's attenuation curve. There are large discrepancies with the values found for sightlines toward the bulge in the Melchior et al. (2000) and Dong et al. (2014) studies. We have not measured the properties of the attenuation curve on any sightlines toward the bulge. We do, however, find that regions toward the center of the galaxy have smaller ensemble R_V values than are seen toward the outer parts of the galaxy. Therefore, we are not concerned with the discrepancies between our overall results and those presented in Melchior et al. (2000) and Dong et al. (2014).

It is important to remember that line-of-sight variation in a galaxy like M31 is likely to be large. Such galaxies cover enormous ranges in stellar environments, from highly crowded to very sparse, from completely obscured to dust-free. These differences will naturally lead to variation in the properties of dust across the galaxy and the resulting R_V values derived from the dust distribution. In the 81% of regions with $\widetilde{\sigma_{R_V}} < 0.8$, 28% have $\widetilde{R_V} < 2.5$ and

17% have $\widetilde{R_V} > 3.5$. In high dust regions with $\widetilde{A_V} > 0.8$, ∼5% of the regions have $\widetilde{R_V} < 2.5$. Averaging over individual line-of-sight values to generate a single galaxy-wide value of R_V smooths over this variation. Solving for the properties of the ensemble distribution, as we have done here, preserves the inherent variation seen within the galaxy. It must, however, be properly used, since taking the peak values of the ensemble for all regions in a galaxy is no different than averaging over regions.

4.5.2 Implications for dust properties

The parameter R_V is generally assumed to represent the dust grain size distribution in a region. Small values of R_V indicate small dust grains and large values of R_V indicate large dust grains. It is important to remember, though, that this definition of R_V came after it was used to parameterize extinction curves. That is, the Cardelli et al. (1989) curves are not physically motivated.

The attribution of R_V to grain size is sensible. Smaller values of R_V result in steeper curves in the UV. A steeper curve requires that more UV light must be attenuated by dust. Dust grains are most likely to affect wavelengths that are similar in size. Therefore, for high attenuation at small wavelengths, there must be small dust grains. Correspondingly, as R_V increases, the dust curve flattens at the UV end resulting in less attenuation of UV light. This suggests that photons at UV wavelengths are not as affected by dust, requiring larger dust grains.

The source of the 2175 Å bump in attenuation curves has long been discussed. Stecher & Donn (1965) first suggested that the bump feature could be due to interstellar graphite grains, and many studies followed up (e.g. Savage & Mathis 1979). However, it was eventually recognized that this interpretation had a number of flaws, including that the position of the peak of the bump was dependent on dust grain properties (e.g., Massa et al. 1983), whereas observations suggest that the bump position is constant (e.g., Fitzpatrick & Massa 1986; Mathis 1994) and models cannot reproduce this constancy if they change dust particle properties such as the size distribution or shape of the grains (e.g., Draine & Malhotra 1993).

The strongest explanation today is that polycyclic aromatic hydrocarbons (PAHs) are responsible for the 2175 Å bump feature (e.g., Desert et al. 1990; Li & Greenberg 1997; Weingartner & Draine 2001). The importance of PAH emission in the infrared (IR) is well-studied, where originally un-identified IR features were determined to be the result of PAH emission (e.g., Leger & Puget 1984). Laboratory measurements of PAH emission in the visible and UV showed that PAHs are responsible for at least some of the bump emission (Joblin et al. 1992). Studies of nearby galaxies suggest that PAH emission can be very sensitive to the local radiation field, in that harder ration fields can efficiently destroy PAH molecules (e.g., Smith et al. 2007). This provides a logical explanation for the variation in 2175 Å bump strength from galaxy-to-galaxy. However, the PAH hypothesis is still a matter of debate. Current models predict the strength of the 2175 Å bump feature by assuming that it is largely due to PAH emission; i.e., PAH molecules fit the 2175 Å bump feature by construction. Nevertheless, they are still the most likely candidate for this feature.

With that in mind, the result presented in this paper, $R_V = 2.94$ over all regions, implies a steeper extinction curve and smaller dust grains than seen in the MW. Because smaller dust grains imply greater attenuation at UV wavelengths, existing measurements of UV attenuation in M31 using a MW curve are under-estimated. An under-estimation of the attenuation affects the interpretation of flux from the galaxy, including the conversion of that flux into a SFR.

Additionally, we find that the 2175 Å bump feature is only 68% the strength of that in the MW. A weaker bump suggests to first order that M31 contains fewer PAH molecules than the MW, due either to inherently different dust compositions or to variations in the UV radiation field. Montalto et al. (2009) find that the radiation field in M31 is up to twice that of the MW. Draine et al. (2014) find that PAH abundance is constant out to 20 kpc at a global value of 3.9% of the dust mass, slightly smaller than the 4.5% estimate in the solar neighborhood (Draine & Li 2007).

4.5.3 Is R_V dependent on A_V?

There is evidence that R_V varies with A_V. Whittet et al. (2001) suggest that in the coldest, densest regions of molecular clouds, the optical properties of dust change. In particular, the size distribution shifts from small to large grains. This could be due to the growth of icy coatings, which is independent of the dust particle size, or due to grain growth by collision. In altering the grain size distribution, this process of grain growth changes the properties of the attenuation curve by changing the value of R_V.

Other studies have seen similar correlations. A strong correlation between R_V and A_V in stars with $A_V > 2.0$ has been measured in the center of the Perseus molecular cloud (Foster et al. 2013), further supporting the suggestion of grain growth in highly dense environments. An earlier study covering a range of environments found a slight correlation between R_V and the average extinction per unit gas mass (given by A_V / N_H) such that as A_V / N_H increases, R_V also increased (Kim & Martin 1996). A possible correlation is also seen in the extinction law at high-latitude (Larson & Whittet 2005). The range in A_V is small, with most sightlines having $A_V < 1.5$, and the observed trend between R_V and A_V is slight.

The results presented in this paper also show a very slight dependence of R_V on A_V. The bottom left panel of Figure 4.10, in which we plot $\widetilde{R_V}$ versus $\widetilde{A_V}$ as a function of SFR for regions with well-measured values of $\widetilde{R_V}$, shows that the regions with the lowest values of $\widetilde{A_V}$ have lower $\widetilde{R_V}$ than those with the highest values of $\widetilde{A_V}$. M31, however, is not a particularly dusty galaxy and the range in A_V is small and at low-valued. There is a large amount of scatter in this relation such that any given $\widetilde{A_V}$ corresponds to $\Delta\widetilde{R_V} = 2 - 3$. Therefore, while the bulk trend suggests a dependence of R_V on A_V, the environment probed at the scales of this paper prevent a full exploration of this correlation.

On a region-by-region basis, we have determined the value of R_V with fairly high precision. On the other hand, $f_{\rm bump}$ is much less well-defined. It has non-zero probability across the distribution. Improvement to this work is necessary to further refine our measurements of $f_{\rm bump}$. The most straightforward way to do this is to increase the number of bands measured

in the UV. In this study, we use only the two *GALEX* bands. Inclusion of the bands from SWIFT/UVOT, would increase the number to 5 and provide three bands in the NUV range which would allow for further constraint on the measurement of 2175 Å bump feature, which primarily affects the NUV.

There are, of course, a variety of ways to determine the properties of the attenuation curve. One such tool that is being used in M31 is the Bayesian Extinction and Stellar Tool (BEAST; Gordon et al. 2016). The BEAST uses a probabilistic approach to model the photometric SEDs of resolved stars observed in large surveys, such as PHAT. The BEAST models the dust-attenuated stellar SED with robust uncertainties using the 6-band photometry available from the PHAT survey. One of the primary goals of the BEAST is to study the properties of dust in galaxies for which resolved star observations are available, the first of which will be M31. By modeling the SEDs of individually-resolved stars and averaging the results in rectangular regions, the BEAST can create maps of the dust properties (i.e., A_V, R_V, column density) across the PHAT survey (H. Arab et al., in prep.). This is a very complementary method to the one described in this paper and will enable confirmation of the results presented here.

4.6 Summary

We fit the observed-to-intrinsic flux ratios in the FUV and NUV in 100 pc size regions across the disk of M31 using a Conroy et al. (2010) extinction curve with two parameters: R_V and $f_{\rm bump}$, the strength of the 2175 Å bump relative to the Milky Way.

We find that the individual regions generally show good constraints on their R_V distribution, but poor constraints on the $f_{\rm bump}$ distribution. When we combine all of the regions and model the ensemble under the assumption of a normal distribution, we find that the best R_V is $\mu_{R_V} = 2.94$ with a width of $\sigma_{R_V} = 0.71$, and the best $f_{\rm bump}$ is $\mu_{f_{\rm bump}} = 0.68$ with a width of $\sigma_{f_{\rm bump}} = 0.19$, compared to $R_V = 3.1$ and $f_{\rm bump} = 1.0$ in the MW.

This mean R_V value implies a steeper attenuation curve than that seen in the MW, there is also a significant width to the distribution. This width encompasses the range in R_V

we see on these 100 pc spatial scales. Interestingly, the width of the $f_{\rm bump}$ distribution is fairly small, despite the poor constraints on individual regions, which likely indicates that the $f_{\rm bump}$ distribution is dominated by measurement errors.

We also compute the ensemble distributions with various cuts on our data. We find that the mean R_V increases and the width of the distribution decreases as we cut out regions with low A_V. We see the same trend if we make a cut in SFR, selecting only the regions with SFR $> 10^{-5} - 10^{-4}$ $\rm M_\odot\,yr^{-1}$.

We find that the central regions of M31 show a strong decrease in R_V relative to the rest of the galaxy, similar to studies of M31's bulge, which find $R_V < 2.5$.

Our mean ensemble R_V, μ_{R_V}, is highly constrained and 15σ below the MW value. The width of the distribution, however, represents the wide range of R_V values found across the disk of M31. Additionally, the range of R_V specified in the literature is also large and likely reflective of the difference between individual lines-of-sight probed in different studies. This region-to-region variation will become increasingly important as we move toward higher resolution and probe the physics of star formation and the interstellar medium on smaller and smaller scales.

Chapter 5

CONCLUSIONS

In this last chapter, I briefly summarize the results presented in this dissertation and discuss directions for future work.

5.1 Summary

In this dissertation, I presented a detailed view of star formation on small scales over a large contiguous area of the Milky Way-like galaxy M31. This work was made possible by observations taken by the *Hubble Space Telescope* as part of the Panchromatic Hubble Andromeda Treasury, a multi-year *HST* program that imaged more than 120 million stars in M31.

In Chapter 2, I began by splitting the PHAT survey area into ∼9000 regions that are ∼100 pc × 100 pc in projected size. I used the colors and magnitudes of the individually-resolved stars to model the CMD and measure the SFH going back 500 Myr in each region. I showed that on 100 pc scales, the SFHs display significant variation that is dependent on stellar environment as well as dust and gas reservoirs. Despite this variation, there is also galaxy-wide fluctuation in the SFH. I found that M31's well-known 10-kpc star-forming ring is a long-lived structure, with ongoing star formation over at least the past 500 Myr. This is remarkable given that the dynamical timescale at this radius is ∼250 Myr. Additionally, the ring is a stationary structure, with no indication of radial movement suggestive of an expanding density wave caused by the infall of a satellite galaxy suggested in recent studies.

I also showed that the SFR in M31 has been globally declining over the past 500 Myr. The SFH reveal a small bump in the SFR 50 Myr, corresponding to star-forming regions in the ring. We found that the SFR averaged over the past 100 Myr is 0.28 ± 0.03 $M_\odot\,yr^{-1}$

with an average deprojected intensity of 7.3×10^{-4} $M_\odot$ yr^{-1} kpc^{-2}. This yields a total SFR of $\sim$0.7 $M_\odot$ yr^{-1} when extrapolated to the entire area of M31's disk.

In Chapter 3, I then used the spatially-resolved recent SFHs from Chapter 2 in combination with population synthesis modeling to generate synthetic NUV and FUV maps of M31, with and without dust reddening. I showed that the reddened maps reproduce the main morphological features in the *GALEX* imaging, including the rings and large star-forming complexes. The predicted flux was in good agreement with the observed flux, with median ratios between the modeled and observed flux of $\log_{10}(f^{\rm syn}_{\rm FUV}/f^{\rm obs}_{\rm FUV}) = 0.005 \pm 0.24$ and $\log_{10}(f^{\rm syn}_{\rm NUV}/f^{\rm obs}_{\rm NUV}) = -0.027 \pm 0.16$ in the FUV and NUV, respectively. This agreement verifies the robustness of the technique used to model the UV.

I used the dust-free map in the FUV to examine obscured star formation in M31. I demonstrated that the predicted FUV flux indicated that 88% of the FUV flux in M31 is obscured by dust compared to the 71% suggested by use of *GALEX* FUV flux and FUV + 24 μm flux, which captures the flux emitted by young stars that was absorbed by dust and re-emitted at longer wavelengths. This difference propagates to discrepancies in the SFRs derived from the FUV + 24 μm flux and those determined from the 100 Myr average SFR from the CMD-based SFHs. The 24 μm-corrected FUV flux underestimates the SFR by a factor of $\sim$2.5. The results presented in this study indicate the necessity of properly accounting for UV flux re-emitted at all wavelengths.

Chapter 3 emphasized the importance of understanding the role of dust in characterizing SFRs, so in Chapter 4, I delved into the properties of the attenuation curve. I inferred the shape of the UV attenuation curve in each region by comparing the observed *GALEX* data with synthetic data that was created with different attenuation curve parameters. Specifically, I fit for an attenuation curve model that includes both variable slope, R_V, and variable strength of the 2175 Å bump relative to that of the MW, $f_{\rm bump}$, using an MCMC algorithm. I derived values for R_V and $f_{\rm bump}$ in each region, and then used the constraints in each region to determine the global parameters by modeling the ensemble.

I found that values of R_V are distributed with a mean of $\mu_{R_V} = 2.94 \pm 0.01$ and a width

of $\sigma_{R_V} = 0.71 \pm 0.01$. The bump strength, $f_{\rm bump}$, distribution has a mean of $\mu_{f_{\rm bump}} = 0.68 \pm 0.01$ and a width of $\sigma_{f_{\rm bump}} = 0.19 \pm 0.01$. The mean R_V is somewhat smaller than the canonical MW value ($R_V = 3.1$), which corresponds to a more than 15σ deviation. The MW value can, however, be drawn from the M31 distribution with high probability. The 2175 Å bump feature is weaker than that of the MW, with agreement seen within 2σ. I created maps of R_V and $f_{\rm bump}$ across the PHAT survey area, which showed that R_V varies considerably across the survey and correlates strongly with A_V, while$f_{\rm bump}$ does not suggest any structural variation.

5.2 Future Work

The data products that resulted from the studies presented here are highly useful as input into other studies to examine many different research topics. The SFHs presented in Chapter 2 have already been used by others.

This dissertation showcases the natural usefulness of the SFHs presented in Chapter 2 to enhance future studies. While they are interesting by themselves, the SFHs were used to predict UV fluxes in Chapter 3, and those fluxes were used to examine the attenuation curve in Chapter 4.

5.2.1 Calibrating SFR *Formulae*

A natural extension of the work presented here is to use the SFHs and the predicted UV flux to re-examine standard SFR formulae. One of the largest challenges to calibrating SFR measurements is determining the "true" SFR. CMD-fitting is generally considered to be the most accurate way to measure SFRs. It can only be done in the most nearby galaxies where stars are individually resolved. This makes the very local Universe the perfect laboratory for verifying the standard formulae used to measure SFRs in the more distant universe.

I briefly discussed in Chapter 3 that the commonly-used SFR tracer of *GALEX* FUV + *Spitzer* 24 μm flux under-estimated the SFR in M31 by a factor of 2.5. I pointed to the literature to demonstrate that the manner in which these two terms are combined is highly

uncertain and the coefficient used varies both within and between galaxies. The SFHs in M31 can be used as the ground truth to calibrate not only the combination of the FUV + 24 μm tracer, but also combinations with longer wavelengths. The range of environments that the SFHs span enables wider application of the M31 results.

5.2.2 Examining the relationship between Star Formation and the ISM

A second area of interest is to probe the relation between star formation and the clouds of dust and gas from which stars form. Star formation is an extremely important phenomenon that affects almost all areas of astrophysics. The manner in which gas condenses to form stars is the subject of much study. A great deal of work has been done on very small scales to understand the conditions inside the cores of molecular clouds that promote the formation of stars (e.g., Bate 2009). The relations for star formation on galactic scales (1 kpc or greater) are also well-studied (e.g., Bigiel et al. 2008). The scale in between – tens to hundreds of parsecs – is not as well understood.

Galactic scale relations work because they require that regions be large enough that on average they are smooth – no clumps of star formation or dust. The number and location of molecular clouds is unimportant. These relations are known to break down on smaller scales when this averaging is no longer applicable. Regions are small enough that some regions may have molecular clouds and others may not. At the other end of the spectrum, the results of the very small-scale studies are not scalable to the more sparse regions outside molecular clouds.

A study of this in-between scale is needed. Such a study would seek to understand the effects of star formation on the ISM by quantifying the energy injection from star formation into the ISM. It would examine the effects of time to better understand the timescale over which star formation occurs. It would analyze the importance of scale by examining how relations change with physical size.

5.2.3 Expansion to other galaxies

All of the work presented here has been performed in the Milky Way-like galaxy, M31, where the PHAT survey provides a 120 million star catalog from which to extract data. In our effort to learn more about how the MW formed and has evolved, M31 is the perfect external galaxy as its properties are most similar.

However, in a number of other ways, M31 is a very unusual galaxy. It forms most of its stars in a large ring, discussed in Chapter 2, rather than in spiral arms. It has a very low SFR and is likely turning off its star formation. While it is a dusty galaxy, its dust content is low relative to most other galaxies in the Universe. This makes M31 a very interesting galaxy to study, but may also limit the applicability of the results to different types of galaxies.

Ideally, we would like to do similar work on a variety of galaxies to cover a range in masses, SFRs, dust content, etc. Unfortunately, we are limited to the Local Group, which consists primarily of very low-mass dwarf galaxies, which have been highly studies though are not as useful for spatial work. The largest galaxies are the MW, M31, the Large and Small Magellanic Clouds, which have previously been studies in a manner similar to the work in Chapter 2 (Harris & Zaritsky 2004, 2009), and M33. The next obvious place to extend this work is to M33, which is the target of an upcoming *HST* program.

BIBLIOGRAPHY

Agertz, O., & Kravtsov, A. V. 2015a, ApJ, 804, 18

—. 2015b, ArXiv e-prints, arXiv:1509.00853

Aparicio, A., & Hidalgo, S. L. 2009, AJ, 138, 558

Athanassoula, E., & Beaton, R. L. 2006, MNRAS, 370, 1499

Athanassoula, E., Romero-Gómez, M., & Masdemont, J. J. 2009, MNRAS, 394, 67

Azimlu, M., Marciniak, R., & Barmby, P. 2011, AJ, 142, 139

Balick, B., Kwitter, K. B., Corradi, R. L. M., & Henry, R. B. C. 2013, ApJ, 774, 3

Barlow, M. J., & Cohen, M. 1977, ApJ, 213, 737

Barmby, P., Huchra, J. P., Brodie, J. P., et al. 2000, AJ, 119, 727

Barmby, P., Ashby, M. L. N., Bianchi, L., et al. 2006, ApJ, 650, L45

Bastian, N., Gieles, M., Ercolano, B., & Gutermuth, R. 2009, MNRAS, 392, 868

Bastian, N., Weisz, D. R., Skillman, E. D., et al. 2011, MNRAS, 412, 1539

Bate, M. R. 2009, MNRAS, 397, 232

Battisti, A. J., Calzetti, D., & Chary, R.-R. 2016, ApJ, 818, 13

Beaton, R. L., Majewski, S. R., Guhathakurta, P., et al. 2007, ApJ, 658, L91

Bernard, E. J., Ferguson, A. M. N., Chapman, S. C., et al. 2015a, MNRAS, 453, L113

Bernard, E. J., Ferguson, A. M. N., Barker, M. K., et al. 2012, MNRAS, 420, 2625

Bernard, E. J., Ferguson, A. M. N., Richardson, J. C., et al. 2015b, MNRAS, 446, 2789

Bertelli, G., & Nasi, E. 2001, AJ, 121, 1013

Bianchi, L., Clayton, G. C., Bohlin, R. C., Hutchings, J. B., & Massey, P. 1996, ApJ, 471, 203

Bigiel, F., Leroy, A., Walter, F., et al. 2008, AJ, 136, 2846

Bigiel, F., Leroy, A. K., Walter, F., et al. 2011, ApJ, 730, L13

Blair, W. P., Kirshner, R. P., & Chevalier, R. A. 1982, ApJ, 254, 50

Block, D. L., Bournaud, F., Combes, F., et al. 2006, Nature, 443, 832

Boquien, M., Buat, V., & Perret, V. 2014, A&A, 571, A72

Boquien, M., Calzetti, D., Aalto, S., et al. 2015, A&A, 578, A8

Boquien, M., Kennicutt, R., Calzetti, D., et al. 2016, A&A, 591, A6

Braun, R., Thilker, D. A., Walterbos, R. A. M., & Corbelli, E. 2009, ApJ, 695, 937

Brinks, E., & Burton, W. B. 1984, A&A, 141, 195

Brinks, E., & Shane, W. W. 1984, A&AS, 55, 179

Brown, T. M., Smith, E., Ferguson, H. C., et al. 2006, ApJ, 652, 323

—. 2007, ApJ, 658, L95

Brown, T. M., Beaton, R., Chiba, M., et al. 2008, ApJ, 685, L121

Buat, V., Noll, S., Burgarella, D., et al. 2012, A&A, 545, A141

Bundy, K., Bershady, M. A., Law, D. R., et al. 2015, ApJ, 798, 7

Buta, R. 1986, ApJS, 61, 609

—. 1995, ApJS, 96, 39

Buta, R., & Combes, F. 1996, Fund. Cosmic Phys., 17, 95

Calzetti, D. 2001, PASP, 113, 1449

Calzetti, D., Armus, L., Bohlin, R. C., et al. 2000, ApJ, 533, 682

Calzetti, D., Kinney, A. L., & Storchi-Bergmann, T. 1994, ApJ, 429, 582

Calzetti, D., Kennicutt, R. C., Engelbracht, C. W., et al. 2007, ApJ, 666, 870

Cardelli, J. A., Clayton, G. C., & Mathis, J. S. 1989, ApJ, 345, 245

Chemin, L., Carignan, C., & Foster, T. 2009, ApJ, 705, 1395

Chen, C.-H. R., Indebetouw, R., Chu, Y.-H., et al. 2010, ApJ, 721, 1206

Chomiuk, L., & Povich, M. S. 2011, AJ, 142, 197

Clayton, G. C., Gordon, K. D., Bianchi, L. C., et al. 2015, ApJ, 815, 14

Code, A. D. 1969, PASP, 81, 475

Cole, A. A., Skillman, E. D., Tolstoy, E., et al. 2007, ApJ, 659, L17

Conroy, C. 2013, ARA&A, 51, 393

Conroy, C., & Gunn, J. E. 2010, ApJ, 712, 833

Conroy, C., Gunn, J. E., & White, M. 2009, ApJ, 699, 486

Conroy, C., Schiminovich, D., & Blanton, M. R. 2010, ApJ, 718, 184

Corbelli, E., Lorenzoni, S., Walterbos, R., Braun, R., & Thilker, D. 2010, A&A, 511, A89

Crocker, A. F., Chandar, R., Calzetti, D., et al. 2015, ApJ, 808, 76

da Silva, R. L., Fumagalli, M., & Krumholz, M. 2012, ApJ, 745, 145

da Silva, R. L., Fumagalli, M., & Krumholz, M. R. 2014, MNRAS, 444, 3275

Dalcanton, J. J., Williams, B. F., Seth, A. C., et al. 2009, ApJS, 183, 67

Dalcanton, J. J., Williams, B. F., Lang, D., et al. 2012, ApJS, 200, 18

Dalcanton, J. J., Fouesneau, M., Hogg, D. W., et al. 2015, ApJ, 814, 3

Davidge, T. J., McConnachie, A. W., Fardal, M. A., et al. 2012, ApJ, 751, 74

de Vaucouleurs, G., de Vaucouleurs, A., Corwin, H. G., et al. 1995, VizieR Online Data Catalog, 7155, 0

Desert, F.-X., Boulanger, F., & Puget, J. L. 1990, A&A, 237, 215

Dierickx, M., Blecha, L., & Loeb, A. 2014, ApJ, 788, L38

Dohm-Palmer, R. C., Skillman, E. D., Mateo, M., et al. 2002, AJ, 123, 813

Dolphin, A. E. 2000, PASP, 112, 1383

—. 2002, MNRAS, 332, 91

—. 2012, ApJ, 751, 60

—. 2013, ApJ, 775, 76

Dong, H., Li, Z., Wang, Q. D., et al. 2014, ApJ, 785, 136

Dorman, B., Rood, R. T., & O'Connell, R. W. 1993, ApJ, 419, 596

Dorman, C. E., Guhathakurta, P., Fardal, M. A., et al. 2012, ApJ, 752, 147

Draine, B. T. 2003, ARA&A, 41, 241

Draine, B. T., & Li, A. 2007, ApJ, 657, 810

Draine, B. T., & Malhotra, S. 1993, ApJ, 414, 632

Draine, B. T., Aniano, G., Krause, O., et al. 2014, ApJ, 780, 172

Duane, S., Kennedy, A., Pendleton, B. J., & Roweth, D. 1987, Physics Letters B, 195, 216

Fitzpatrick, E. L. 1986, AJ, 92, 1068

Fitzpatrick, E. L., & Massa, D. 1986, ApJ, 307, 286

—. 2007, ApJ, 663, 320

Ford, G. P., Gear, W. K., Smith, M. W. L., et al. 2013, ApJ, 769, 55

Foreman-Mackey, D., Hogg, D. W., Lang, D., & Goodman, J. 2013, PASP, 125, 306

Foreman-Mackey, D., Hogg, D. W., & Morton, T. D. 2014, ApJ, 795, 64

Foster, J. B., Mandel, K. S., Pineda, J. E., et al. 2013, MNRAS, 428, 1606

Fritz, J., Gentile, G., Smith, M. W. L., et al. 2012, A&A, 546, A34

Galarza, V. C., Walterbos, R. A. M., & Braun, R. 1999, AJ, 118, 2775

Gallart, C., Freedman, W. L., Aparicio, A., Bertelli, G., & Chiosi, C. 1999, AJ, 118, 2245

Gallart, C., Zoccali, M., & Aparicio, A. 2005, ARA&A, 43, 387

Gehrels, N., Chincarini, G., Giommi, P., et al. 2004, ApJ, 611, 1005

Gil de Paz, A., Boissier, S., Madore, B. F., et al. 2007, ApJS, 173, 185

Gilbert, K. M., Guhathakurta, P., Kollipara, P., et al. 2009, ApJ, 705, 1275

Gilbert, K. M., Kalirai, J. S., Guhathakurta, P., et al. 2014, ApJ, 796, 76

Girardi, L., Williams, B. F., Gilbert, K. M., et al. 2010, ApJ, 724, 1030

Gogarten, S. M., Dalcanton, J. J., Williams, B. F., et al. 2010, ApJ, 712, 858

Gordon, K. D., Bailin, J., Engelbracht, C. W., et al. 2006, ApJ, 638, L87

Gordon, K. D., Fouesneau, M., Arab, H., et al. 2016, ApJ, 826, 104

Governato, F., Zolotov, A., Pontzen, A., et al. 2012, MNRAS, 422, 1231

Groves, B., Krause, O., Sandstrom, K., et al. 2012, MNRAS, 426, 892

Guhathakurta, P., Rich, R. M., Reitzel, D. B., et al. 2006, AJ, 131, 2497

Hao, C.-N., Kennicutt, R. C., Johnson, B. D., et al. 2011, ApJ, 741, 124

Harris, D. H. 1973, in IAU Symposium, Vol. 52, Interstellar Dust and Related Topics, ed. J. M. Greenberg & H. C. van de Hulst, 31

Harris, J., & Zaritsky, D. 1999, AJ, 117, 2831

—. 2004, AJ, 127, 1531

—. 2009, AJ, 138, 1243

Hernandez, X., Valls-Gabaud, D., & Gilmore, G. 2000, MNRAS, 316, 605

Hopkins, P. F., Kereš, D., Oñorbe, J., et al. 2014, MNRAS, 445, 581

Ibata, R., Chapman, S., Ferguson, A. M. N., et al. 2004, MNRAS, 351, 117

Joblin, C., Leger, A., & Martin, P. 1992, ApJ, 393, L79

Johnson, B. D., Schiminovich, D., Seibert, M., et al. 2007, ApJS, 173, 392

Johnson, B. D., Weisz, D. R., Dalcanton, J. J., et al. 2013, ApJ, 772, 8

Johnson, L. C., Seth, A. C., Dalcanton, J. J., et al. 2012, ApJ, 752, 95

—. 2015, ApJ, 802, 127

Kalirai, J. S., Gilbert, K. M., Guhathakurta, P., et al. 2006, ApJ, 648, 389

Kang, Y., Bianchi, L., & Rey, S.-C. 2009, ApJ, 703, 614

Kennicutt, R. C., & Evans, N. J. 2012, ARA&A, 50, 531

Kennicutt, Jr., R. C. 1989, ApJ, 344, 685

—. 1998, ARA&A, 36, 189

Kennicutt, Jr., R. C., Calzetti, D., Walter, F., et al. 2007, ApJ, 671, 333

Kennicutt, Jr., R. C., Hao, C.-N., Calzetti, D., et al. 2009, ApJ, 703, 1672

Kim, S.-H., & Martin, P. G. 1996, ApJ, 462, 296

Kim, S.-H., Martin, P. G., & Hendry, P. D. 1994, ApJ, 422, 164

Koch, A., Rich, R. M., Reitzel, D. B., et al. 2008, ApJ, 689, 958

Kormendy, J. 1979, ApJ, 227, 714

Kroupa, P. 2001, MNRAS, 322, 231

Krumholz, M. R., Fumagalli, M., da Silva, R. L., Rendahl, T., & Parra, J. 2015, MNRAS, 452, 1447

Kwitter, K. B., Lehman, E. M. M., Balick, B., & Henry, R. B. C. 2012, ApJ, 753, 12

Larson, K. A., & Whittet, D. C. B. 2005, ApJ, 623, 897

Lee, C.-H., Kodric, M., Seitz, S., et al. 2013, ApJ, 777, 35

Lee, J. C., Gil de Paz, A., Tremonti, C., et al. 2009, ApJ, 706, 599

Lee, J. C., Gil de Paz, A., Kennicutt, Jr., R. C., et al. 2011, ApJS, 192, 6

Leger, A., & Puget, J. L. 1984, A&A, 137, L5

Leroy, A. K., Walter, F., Brinks, E., et al. 2008, AJ, 136, 2782

Leroy, A. K., Bigiel, F., de Blok, W. J. G., et al. 2012, AJ, 144, 3

Leroy, A. K., Walter, F., Sandstrom, K., et al. 2013, AJ, 146, 19

Lewis, A. R., Dolphin, A. E., Dalcanton, J. J., et al. 2015, ApJ, 805, 183

Lewis, A. R., Simones, J. E., Johnson, B. D., et al. 2016, submitted

Li, A., & Greenberg, J. M. 1997, A&A, 323, 566

Li, Y., Crocker, A. F., Calzetti, D., et al. 2013, ApJ, 768, 180

Lynds, R., & Toomre, A. 1976, ApJ, 209, 382

Marcum, P. M., O'Connell, R. W., Fanelli, M. N., et al. 2001, ApJS, 132, 129

Marigo, P., Girardi, L., Bressan, A., et al. 2008, A&A, 482, 883

Martin, D. C., Fanson, J., Schiminovich, D., et al. 2005, ApJ, 619, L1

Massa, D., Savage, B. D., & Fitzpatrick, E. L. 1983, ApJ, 266, 662

Massey, P., Olsen, K. A. G., Hodge, P. W., et al. 2006, AJ, 131, 2478

Mathis, J. S. 1994, ApJ, 422, 176

McConnachie, A. W., Irwin, M. J., Ferguson, A. M. N., et al. 2005, MNRAS, 356, 979

Meidt, S. E., Schinnerer, E., van de Ven, G., et al. 2014, ApJ, 788, 144

Melchior, A.-L., Viallefond, F., Guélin, M., & Neininger, N. 2000, MNRAS, 312, L29

Meurer, G. R., Wong, O. I., Kim, J. H., et al. 2009, ApJ, 695, 765

Meynet, G., Maeder, A., Schaller, G., Schaerer, D., & Charbonnel, C. 1994, A&AS, 103

Monachesi, A., Trager, S. C., Lauer, T. R., et al. 2012, ApJ, 745, 97

Monelli, M., Hidalgo, S. L., Stetson, P. B., et al. 2010, ApJ, 720, 1225

Montalto, M., Seitz, S., Riffeser, A., et al. 2009, A&A, 507, 283

Morrissey, P., Conrow, T., Barlow, T. A., et al. 2007, ApJS, 173, 682

Murphy, E. J., Condon, J. J., Schinnerer, E., et al. 2011, ApJ, 737, 67

Nataf, D. M., Gonzalez, O. A., Casagrande, L., et al. 2016, MNRAS, 456, 2692

Nieten, C., Neininger, N., Guélin, M., et al. 2006, A&A, 453, 459

O'Connell, R. W. 1999, ARA&A, 37, 603

O'Connell, R. W., Bohlin, R. C., Collins, N. R., et al. 1992, ApJ, 395, L45

Pei, Y. C. 1992, ApJ, 395, 130

Pilyugin, L. S., Grebel, E. K., & Kniazev, A. Y. 2014, AJ, 147, 131

Pradhan, A. C., Ojha, D. K., Robin, A. C., Ghosh, S. K., & Vickers, J. J. 2014, A&A, 565, A33

Prevot, M. L., Lequeux, J., Prevot, L., Maurice, E., & Rocca-Volmerange, B. 1984, A&A, 132, 389

Roberts, M. S. 1966, ApJ, 144, 639

Robitaille, T. P., & Whitney, B. A. 2010, ApJ, 710, L11

Rosenfield, P., Johnson, L. C., Girardi, L., et al. 2012, ApJ, 755, 131

Roussel, H., Gil de Paz, A., Seibert, M., et al. 2005, ApJ, 632, 227

Sanders, N. E., Caldwell, N., McDowell, J., & Harding, P. 2012, ApJ, 758, 133

Savage, B. D., & Mathis, J. S. 1979, ARA&A, 17, 73

Scannapieco, C., Wadepuhl, M., Parry, O. H., et al. 2012, MNRAS, 423, 1726

Schlafly, E. F., Meisner, A. M., Stutz, A. M., et al. 2016, ApJ, 821, 78

Schmidt, M. 1959, ApJ, 129, 243

Schmitt, H. R., Calzetti, D., Armus, L., et al. 2006, ApJ, 643, 173

Schruba, A., Leroy, A. K., Walter, F., Sandstrom, K., & Rosolowsky, E. 2010, ApJ, 722, 1699

Schultz, G. V., & Wiemer, W. 1975, A&A, 43, 133

Schwarz, M. P. 1981, ApJ, 247, 77

—. 1984, MNRAS, 209, 93

Seon, K.-I., & Draine, B. T. 2016, ArXiv e-prints, arXiv:1606.02030

Sick, J., Courteau, S., Cuillandre, J.-C., et al. 2014, AJ, 147, 109

Simones, J. E., Weisz, D. R., Skillman, E. D., et al. 2014, ApJ, 788, 12

Smith, J. D. T., Draine, B. T., Dale, D. A., et al. 2007, ApJ, 656, 770

Sneden, C., Gehrz, R. D., Hackwell, J. A., York, D. G., & Snow, T. P. 1978, ApJ, 223, 168

Stecher, T. P., & Donn, B. 1965, ApJ, 142, 1681

Struck, C. 2010, MNRAS, 403, 1516

Tabatabaei, F. S., & Berkhuijsen, E. M. 2010, A&A, 517, A77

Thilker, D. A., Hoopes, C. G., Bianchi, L., et al. 2005, ApJ, 619, L67

Towns, J., Cockerill, T., Dahan, M., et al. 2014, Computing in Science and Engineering, 16, 62

Trundle, C., Dufton, P. L., Lennon, D. J., Smartt, S. J., & Urbaneja, M. A. 2002, A&A, 395, 519

van den Bergh, S. 1964, ApJS, 9, 65

Walter, F., Brinks, E., de Blok, W. J. G., et al. 2008, AJ, 136, 2563

Walterbos, R. A. M., & Kennicutt, Jr., R. C. 1988, A&A, 198, 61

Walterbos, R. A. M., & Schwering, P. B. W. 1987, A&A, 180, 27

Weingartner, J. C., & Draine, B. T. 2001, ApJ, 548, 296

Weisz, D. R., Dolphin, A. E., Skillman, E. D., et al. 2014, ApJ, 789, 147

Weisz, D. R., Dalcanton, J. J., Williams, B. F., et al. 2011, ApJ, 739, 5

Weisz, D. R., Johnson, B. D., Johnson, L. C., et al. 2012, ApJ, 744, 44

Westera, P., Lejeune, T., Buser, R., Cuisinier, F., & Bruzual, G. 2002, A&A, 381, 524

Whittet, D. C. B., Gerakines, P. A., Hough, J. H., & Shenoy, S. S. 2001, ApJ, 547, 872

Wild, V., Charlot, S., Brinchmann, J., et al. 2011, MNRAS, 417, 1760

Wilkins, S. M., Gonzalez-Perez, V., Lacey, C. G., & Baugh, C. M. 2012, MNRAS, 427, 1490

Williams, B. F. 2002, MNRAS, 331, 293

—. 2003a, MNRAS, 340, 143

—. 2003b, AJ, 126, 1312

Williams, B. F., Dalcanton, J. J., Seth, A. C., et al. 2009, AJ, 137, 419

Williams, B. F., Dalcanton, J. J., Stilp, A., et al. 2010, ApJ, 709, 135

Williams, B. F., Lang, D., Dalcanton, J. J., et al. 2014, ApJS, 215, 9

Williams, B. F., Dalcanton, J. J., Dolphin, A. E., et al. 2015, ApJ, 806, 48

Wyder, T. K., Dolphin, A. E., & Hodge, P. W. 1998, MNRAS, 298, 259

Zaritsky, D. 1999, AJ, 118, 2824

Zaritsky, D., Kennicutt, Jr., R. C., & Huchra, J. P. 1994, ApJ, 420, 87

Zhu, Y.-N., Wu, H., Cao, C., & Li, H.-N. 2008, ApJ, 686, 155

Zubko, V., Dwek, E., & Arendt, R. G. 2004, ApJS, 152, 211

VITA

Alexia R. Lewis was born in Minneapolis, MN. After graduating from high school, she moved east to attend college at Bowdoin College in Brunswick, ME where she earned a Bachelor of Arts in Physics in 2008. She moved back to the Minneapolis area after college and completed a year in the City of Lakes AmeriCorps program, working at a high school in Minneapolis. She also volunteered extensively for the Minneapolis Planetarium Society, presenting planetarium shows in MN schools with a mobile Planetarium. She moved to Seattle, WA in 2010 to begin graduate studies at the University of Washington. Alexia completed her doctorate in 2016.